

A Thesis Submitted for the Degree of PhD at the University of Warwick

Permanent WRAP URL:

<http://wrap.warwick.ac.uk/109387>

Copyright and reuse:

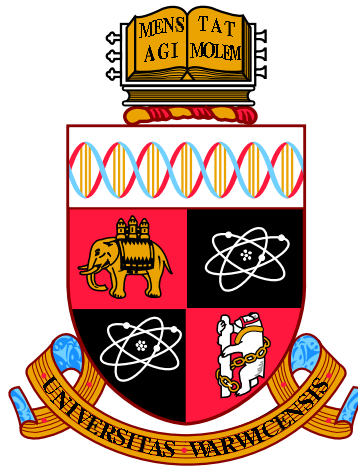
This thesis is made available online and is protected by original copyright.

Please scroll down to view the document itself.

Please refer to the repository record for this item for information to help you to cite it.

Our policy information is available from the repository home page.

For more information, please contact the WRAP Team at: wrap@warwick.ac.uk



MHD Waves and Oscillations in Solar Coronal Waveguides

by

Christopher Rhys Goddard

Thesis

Submitted to the University of Warwick

for the degree of

Doctor of Philosophy

Physics

April 2018

THE UNIVERSITY OF
WARWICK

Contents

List of Tables	iv
List of Figures	v
Acknowledgments	xv
Declarations	xvi
Abstract	xviii
Chapter 1 Introduction	1
1.1 The Sun	1
1.1.1 The solar interior	1
1.1.2 The solar atmosphere	2
1.1.3 Magnetic field and solar cycle	5
1.1.4 Active regions and coronal loops	7
1.1.5 Solar activity	8
1.1.6 Gaps in our understanding	10
1.2 Coronal waves and oscillations	10
1.3 MHD description of coronal plasma	13
1.3.1 MHD waves	15
1.3.2 MHD waves in structured plasma	17
1.4 Kink oscillations of coronal loops	20
1.4.1 Damping	23
1.4.2 Generalised damping	25
1.4.3 Seismology	26
1.4.4 Non-linear effects	31
1.5 QFP wave trains	34
1.6 SDO/AIA	38
1.6.1 Introduction	38
1.6.2 The AIA instrument	39
1.7 Data analysis techniques	40

1.7.1	EUV image analysis	40
1.7.2	Time series analysis	42
1.7.3	Bayesian inference	43
1.7.4	Bayesian inference implementation	45
Chapter 2	Statistical studies of decaying kink oscillations	47
2.1	Introduction	47
2.2	Observations and Analysis	50
2.3	Results	53
2.3.1	Oscillation parameter histograms	53
2.3.2	Dependence of the period on loop length	54
2.3.3	Relationship between the damping time and period	54
2.4	Amplitude dependence of kink oscillation damping	56
2.4.1	Observations	56
2.4.2	Results	56
2.5	Discussion and conclusions	59
2.5.1	Oscillation parameter histograms	59
2.5.2	Dependence of the period on loop length	60
2.5.3	Relationship between the damping time and period	61
2.5.4	Amplitude dependence of the damping	62
2.5.5	Conclusion	63
Chapter 3	Coronal seismology with kink oscillations in the era of SDO/AIA	70
3.1	Introduction	70
3.2	Damping profiles of coronal loops	70
3.2.1	Observations	71
3.2.2	Damping profile analysis	71
3.2.3	Discussion and conclusion	76
3.3	Coronal seismology based on resonant absorption	77
3.4	Coronal Seismology using Bayesian inference	80
3.5	Coronal loop density profile inference	83
3.5.1	Density profile inference	85
3.5.2	Results	86
3.5.3	Discussion and conclusion	87
Chapter 4	The transverse density structure of coronal waveguides	90
4.1	Introduction	90
4.2	Observations	92
4.3	Method	93

4.3.1	Constructed intensity profiles	93
4.3.2	Bayesian inference	93
4.4	Results	96
4.4.1	Model Comparisons	96
4.4.2	Parameter dependencies	98
4.5	Discussion	101
4.6	Conclusions	103

Chapter 5 Observation and simulation of dispersive coronal QFP

wave trains	105
5.1	Introduction 105
5.2	Solar radio emission 106
5.3	Instruments and data 107
5.4	Observations and analysis 109
5.4.1	EUV observations 110
5.4.2	Radio observations 112
5.4.3	Further analysis 116
5.5	Discussion of observational results 117
5.6	Summary of observational results 120
5.7	Modelling of non-linear dispersively formed QFP wave trains 120
5.7.1	Numerical setup 121
5.7.2	Numerical results 123
5.7.3	Discussion and Summary of numerical results 127

Chapter 6 Summary 132

List of Tables

2.1	Damping times, periods, and apparent amplitudes of kink oscillations of coronal loops.	57
2.2	A list of 120 coronal loop kink oscillations detected with AIA/SDO and their measured parameters. The event ID corresponds to the events catalogued in Zimovets & Nakariakov [2015] , and the loop ID distinguishes the different loops in each event (this does not correspond to those in the cited paper). The position of the slit used to produce each time-distance map is given in arcsec, along with the date and oscillation start time in UT. The period and error obtained from fitting the loop oscillation are given, as well as the estimated loop length. The column “Disp Amp” lists the estimated initial loop displacement, and “Osc Amp” is the estimated initial amplitude of the oscillation. The number of cycles that were observed is listed in “N Cyc”. Finally, the exponential damping time and error from fitting the damping profile, and the form of the damping profile (exponential (E), non-exponential(NE), or a combination of both), are listed in the final two columns.	64
3.1	Seismologically determined loop parameters.	79
3.2	Inferred parameters for the density profile models M_i for slit 10. . .	88
4.1	Percentages of coronal loop intensity profiles falling into three evidence thresholds for each permutation of the Bayes factor for Models L , G and S	98
4.2	Rows 1–4: percentages of coronal loop intensity profiles falling into three evidence thresholds for each density model. For a loop to be counted for a given model and threshold it’s Bayes factor from comparison to both other models, K_{ij} and K_{ik} , must be greater than that threshold. Row 5: summed probability values (P_i) for each density model, showing how the evidence is distributed between the three models for the 233 analysed loops.	98

List of Figures

1.1	The structure of the solar interior. Courtesy of NASA.	2
1.2	Solar temperature plot. Courtesy of MSU.	3
1.3	Granulation in the photosphere. Courtesy of NASA.	4
1.4	A HMI magnetogram. Courtesy of NASA.	4
1.5	Top: the corona imaged in white light during an eclipse. Bottom: the corona and lower layers imaged in multiple EUV wavelengths. From left to right these are; 1700 Å (photosphere), 1600 Å (upper photosphere and transition region), 335 Å (corona), 304 Å (chromosphere), 211 Å (corona), 193 Å (corona), 171 Å (corona), 131 Å (corona) and 94 Å (corona). The background segment is the white light continuum emission from HMI. Courtesy of NASA.	6
1.6	Top: the butterfly diagram, which shows the evolution of sunspots locations in latitude over time. Bottom: the average sunspot area as a percentage of the visible solar hemisphere. Both data sets clearly show the 11 year solar cycle. Courtesy of NASA.	7
1.7	A CME imaged by the SOHO satellite. Courtesy of NASA/ESA. . .	9
1.8	A collection of coronal loops imaged with AIA/SDO. Courtesy of NASA.	11
1.9	A global coronal magnetic field extrapolation for open (green) and closed (red) magnetic field lines [Wiegmann et al., 2017].	11
1.10	The methodology of MHD coronal seismology [Nakariakov & Verwichte, 2005].	13
1.11	Top: phase speeds for the three MHD wave modes in a uniform plasma for the case $C_A > C_S$, with ϕ being the angle between the direction of propagation and the magnetic field and the x and y axis being the wave velocities as a fraction of the Alfvén speed (C_A). The fast speed is plotted in black, the Alfvén speed is plotted in red, and the slow speed is in blue. Bottom: as above but with the group speeds plotted.	16

1.12	The straight magnetic cylinder model, with the addition of a finite layer (of width l) where the density varies linearly between the internal and external values [Nakariakov & Verwichte, 2005].	18
1.13	The Dispersion relations of MHD modes in structured coronal plasma. The hashed regions are where modes with real frequency and wavenumber are excluded. The dashed horizontal lines denote the wave speeds indicated on the axis. The solid and dashed curves are the dispersion relations of the modes indicated, with azimuthal wavenumbers 0 and 1 respectively [Edwin & Roberts, 1983].	20
1.14	An example of a kink oscillation of a coronal loop observed with TRACE. On the left is the active region showing the flare and the loop which becomes perturbed and on the right is the time series of the oscillation, approximated by an exponentially damped [Nakariakov et al., 1999].	21
1.15	An example of a kink oscillation of a coronal loop observed with AIA. On the left are 3 Time-Distance (TD) maps showing the kink oscillation at three different positions along the loop, and the right are the corresponding time series and fits [White & Verwichte, 2012].	22
1.16	Scaling of the exponential damping time of kink oscillations with the oscillation period [Verwichte et al., 2013b]	27
1.17	Analytic and numerical inversion curves for three coronal loop parameters; the internal Alfvén travel time (τ_A), the density contrast (ζ) and the inhomogeneous layer width (l/R) [Goossens et al., 2008].	29
1.18	Left: time-distance maps forward modelled to EUV emission from numerical simulations of the KHI instability in oscillating coronal loops. Right: The same simulations, shown as a cross section of the emissivity depicting how the loop cross-section is perturbed during the oscillation [Antolin et al., 2016].	32
1.19	The evolution of a fast sausage wave in the low- β limit, showing the three main phases of the evolution [Roberts et al., 1984].	34
1.20	Numerical simulation of a dispersively generated fast magnetoacoustic wave train generated from a single impulsive perturbation. In the lower panel is the wavelet spectra of the density time series in the upper panel [Nakariakov et al., 2004].	35
1.21	Quasi-periodic fast propagating waves in a funnel structure detected with the AIA instrument [Liu et al., 2011].	36

1.22	Left: Multiple QFP wave trains analysed in Yuan et al. [2013] . Middle: A time-distance map showing the wave fronts of the QFP waves. The bottom panel shows flare pulsations detected with RHESSI, which may be related to the detected waves [Liu et al., 2010] . Right: Fourier power diagram produced from the data to the left, which allowed the wave speed to be measured. Also taken from Liu et al. [2010]	37
1.23	The Solar Dynamics Observatory (SDO) with its three instruments labelled. Courtesy of NASA.	39
1.24	Temperature response functions for six EUV channels of AIA [Lemen et al., 2012]	40
2.1	Left: The active region from event number 40 from Table 2.2. The three blue lines show some of the slits used to create time-distance maps for analysing the oscillations of the corresponding loops. Right: The slit positions (x_1, y_1 from Table 2.2) used to produce the sample of time-distance maps to analyse kink oscillations of coronal loops, plotted as blue asterisks. The overplotted red circles are the average slit position for each event.	48
2.2	Three typical time-distance maps, corresponding to loop 1 from event 32, loop 4 from event 40, and loop 2 from event 48. The fits correspond to the detrending polynomial added to the sinusoidal fit, and multiplied by the exponential damping profile for panels a) and b). The red points in panel c) were taken by eye to map out the oscillation and used for the subsequent fitting. The vertical blue bars represent the measurement of the initial displacement (a_0) and the initial oscillation amplitude (a_{osc} in the figure, A_0 throughout the text) of the upper loop edge.	49
2.3	Left: The distribution of the measured initial displacement of 120 kink oscillations of coronal loops. Right: The distribution of the measured initial oscillation amplitude of 120 kink oscillations of coronal loops, recorded from the first cycle of oscillation after the initial displacement. The bin size of both histograms is 2 Mm.	52
2.4	The initial oscillation amplitude of 120 kink oscillations of coronal loops, plotted against the initial displacement of the loop position. A linear fit of the data passing through the origin is shown by the solid black line, with a gradient of 0.87 ± 0.01	52

2.5	Left: The distribution of the measured periods of 120 individual kink oscillations of coronal loops. The bin size is 1 min. Right: The distribution of the measured loop lengths for 118 individual coronal loops, which undergo kink oscillations. The bin size is 20 Mm. . . .	55
2.6	Left: period plotted against loop length for 118 kink oscillations of coronal loops. The solid black line correspond to an unweighted linear fit of the data. The best fitting linear function gives a kink speed of $C_k=(1300\pm50)\text{km s}^{-1}$ from its gradient. The dashed lines correspond to kink speeds of 800 and 3300 km s^{-1} for the upper and lower lines respectively. Right: damping time plotted against period for 54 kink oscillations of coronal loops. The solid black line correspond to a weighted linear fit of the data. The best fitting linear function is $\tau[\text{min}]= (1.53\pm0.03)P[\text{min}]$. The red circles correspond to damping envelopes best described by an exponential profile, and the blue squares correspond to those best described by a combination of a non-exponential and exponential profiles.	55
2.7	Distribution of the measured apparent initial amplitude of kink oscillations of coronal loops, detected with SDO/AIA, TRACE, and STEREO/EUVI. The bin size is 2 Mm.	58
2.8	Left: the quality factor of kink oscillations of coronal loops determined as the ratio of damping time to the oscillation period, plotted against the apparent oscillation amplitude. The red points are taken from Table 2.2. The blue points correspond to those listed in Table 2.1. The grey line shows the scaling of the quality factor with the maximum apparent amplitude. Right: the quality factor plotted against the apparent amplitude of the initial displacement that excited the oscillation. The data is taken from Table 2.2.	58
3.1	Four examples of the analysed coronal loops. The fit to the loop axis is given by the red dashed line and the blue line shows the position of the chosen slit. From left to right, top to bottom the loops are 43_4, 31_1, 32_1 and 40_10 (see Table. 2.2). The labels at the top of the plots number the loops for discussion in later sections of this chapter.	72
3.2	Time-distance maps for the 6 chosen kink oscillations for damping profile analysis. The slits used to produce four of them are shown in Fig. 3.1.	73

3.3	Kink oscillation observations where the damping profile is better fit by a Gaussian damping envelope than an exponential one. Left: the fitted position of the loop axis as a function of time, with the sinusoidal fits overplotted with Gaussian (blue lines) and exponential (red lines) damping envelopes. The χ^2 values are given for the two fits. Right: the absolute values of the extrema of the oscillations, with the same fitted damping envelopes overplotted and the Gaussian and exponential damping times given.	74
3.4	As for Fig. 3.3 but for two cases where exponential damping profiles were found to be favorable (top two panels) and one inconclusive case (bottom panel).	75
3.5	Left: least-squares fits of the time series of the fitted loop centre position. In blue is the fit with a purely Gaussian envelope, in red with a purely exponential envelope and in green the generalised damping profile which includes both regimes. The dashed line corresponds to the fitted background trend and the dashed-dotted line marks the start of the oscillation. Right: the extrema of the oscillations detrended using the fitted background trend. The colour scheme for the fits is the same as for the left panel. The dashed lines denotes the fitted value of t_s , the time of the switch between the Gaussian and exponential damping profiles.	81
3.6	Left: seismologically determined values of ϵ and ρ_0/ρ_e and their uncertainties (red points). The solid line corresponds to the inversion curve obtained by using the exponential damping time alone, and the dashed lines correspond to the error bars. Right: density profiles for the transverse density structure obtained seismologically. The corresponding LOS intensity for that density profile is shown by the dashed curves.	82
3.7	The seismologically determined transverse structure of the of the coronal loops forward modelled to the corresponding EUV emission (blue). The observed transverse intensity profile is given by the crosses. The green dashed curves correspond to a Gaussian fit to the intensity profile.	83

- 3.8 Analysis for Loop #1 using the oscillation model without dispersion. Top left: the fitted loop position time series (points) and the most credible model as determined by the Bayesian inference (green line), which includes the background trend determined by spline fitting (blue line). The red shaded region shows the 99% credible intervals for the loop position predicted by the model, including fitted noise σ_Y . The dotted and dashed lines show the start of the oscillation, and the switch time of the first harmonic respectively. Top right: wavelet spectrum of the loop position time series with colours representing the normalised spectral amplitude. The three dashed lines show the periods of oscillation in the model, determined by the Bayesian inference. Middle left: detrended loop position (symbols) with the first (green), second (blue), and third (red) longitudinal harmonics. Damping profile switch times for these harmonics are plotted as the dashed lines in the same colour. Middle right: the posterior 2D histogram of the transverse density profile parameters, determined from the oscillation damping envelope. The red bars are based on the median values and the 95% credible intervals, shown in the histograms below. Bottom panels: the posterior histograms for the two density profile parameters, the solid curves are fits using the exponentially modified Gaussian function. The dashed lines are the 95% credible intervals, used to produce the error bars in the 2D histogram above. The dotted lines are the median values. 84
- 3.9 Left: SDO/AIA 171Å image of the analysed loop, observed at 08:58:00 UT on 30 May 2012. The blue lines indicate the locations of the slits used to generate transverse intensity profiles. Right: arbitrary transverse density profiles for the four models. These are; Model S (dotted), Model L (solid), Model G (dashed) and Model E (dashed-dotted). 88
- 3.10 Left: SDO/AIA 171Å EUV intensity (points) across the loop described by Model *L* (blue line) which includes a background trend described by a second order polynomial. The shaded regions represent the 99% confidence intervals for the intensity predicted by the model, with (red) and without (blue) modelled noise. The vertical dotted and dashed lines denote x_0 and $x_0 \pm R$, respectively. Right: the inferred loop density profiles for Models *L* (solid), *E* (dashed), *S* (dotted), and *G* (dash-dot). 89

3.11	Top: normalised layer width ϵ (left) and loop radius R (right) estimated by forward modelling, as a function of length along the loop. The symbols show the median values while the solid curves denote the 95% credible interval. The horizontal dotted lines correspond to the seismologically estimated values. Bottom: the Bayes factors K_{LS} (solid), K_{ES} (dashed), K_{EL} (dotted), and K_{LG} (dash-dot) as a function of length along the loop.	89
4.1	Examples of loops for which Models L (top), G (middle), and S (bottom) were found to best describe the data. Left: SDO/AIA 171 Å image of an analysed loop. The blue line indicates the location of the slits used to generate the transverse intensity profiles. The white box and inset show a magnified region around the loop. Middle: 171 Å EUV intensity profile (symbols) across the selected loop. Model L , G or S (blue line) is plotted, with the model values being the median values from the corresponding probability distributions. The shaded areas represent the 99% confidence region for the intensity predicted by the model, with (red) and without (blue) modelled noise. The vertical dotted and dashed lines denote x_0 and $x_0 \pm R$, respectively. Right: The inferred density profiles for Models S (solid), L (dashed) and G (dotted).	94
4.2	First column: histograms of the Bayes factor (K_{ij}) comparisons of Models L , G and S . Second column: histograms of the model probabilities (P_i) calculated from the evidence values for each model. . .	95
4.3	Left: histograms of the normalised layer width ϵ for the combined thresholds of K_{LS} and K_{LG} given in Tab. 4.1. Right: the normalised layer width, ϵ , plotted against the loop minor radius for Model L , R_L . . .	99
4.4	Comparison of the loop minor radius determined by the three models. Top left: distribution of the median radii from Model S , R_S . Top right: the loop radii from Model L , R_L , plotted against R_S . Bottom: The loop radii from Model G , R_G , plotted against R_S . The blue lines correspond to $R_L=R_S$ and $R_G=R_S$ respectively. The error bars correspond to the 95th percentile.	99
4.5	Top left: Bayes factor K_{LS} plotted against loop radius R_L . Top right: Bayes factor K_{GS} plotted against loop radius R_G . Bottom: Bayes factor K_{LG} plotted against loop radius R_L	100

5.1	Panel a): SDO/AIA 171 Å image during the observed event at 22:00.00 UT centred on the active region of interest (AR 12205). The green boxes show the fields of view used for Fig. 5.2 (solid) and Fig. 5.7 (dashed). Panel b): the analysed region at 22:40:12 UT, F1 and F2 show the apparent extrema of the propagation path of the observed periodic intensity enhancements along a funnel structure, and the blue fit shows the slit used in the analysis. The red points P1 and P2 indicate the positions at which the time series plotted in Fig. 5.4 were extracted from.	108
5.2	Three SDO/AIA images of the active region. In all panels a region of enhanced emission, associated with the ejection of the wave train, is highlighted by a blue box. The red points F1 and F2 indicate the observed start and end points of a guiding funnel structure. Panel a) shows the 171 Å image. Panel b) also shows a 171 image, with the previous frame subtracted. The red arrow indicates an enhancement propagating along the funnel. Panel c) shows a 131 Å image, the orange arrow indicates the direction of a propagating outflow.	109
5.3	Two running difference images of the funnel structure at 171 Å. There is a one frame (12 seconds) separation between the two images. The vertical blue lines approximate the position of the propagating wave front. The dashed red curve indicates the position of the solar limb.	110
5.4	Panel a): Time-distance map formed from the slit along the path of intensity enhancements, between points F1 and F2, shown in Fig. 5.1. The intensity profiles labelled P1 and P2 show the intensity profile at different positions along the slit, and the green arrows indicate the position of main peaks, labelled E1-E6. Panel b): a TD map formed from a slit along the path of intensity enhancements in the running difference images. The diagonal green lines show the propagating intensity enhancements, and the dashed vertical lines indicate the enhancements where no propagation is seen. Box B1 highlights a series of enhancements of shorter spatial and temporal extent. Panel c): an intensity time series extracted from D in panel b), the intensity enhancements E1-E5 are labelled (E6 is missed as it is not prominent at the chosen distance along the slit). Panel d): Morlet wavelet spectra for the intensity time series, showing the distribution of the oscillation power with period as a function of time. The time axis of the four panels refers to the time elapsed since 22:00 UT.	111

5.5	Learmonth, panel a), and BIRS, panel b), radio spectrograms in the ranges 25-170 MHz and 5-60 MHz respectively. Four regions of enhanced emission are indicated in panel a) by R1, R2, R3 and R4. R2-R4 are also indicated in panel b). The time axis refers to the time elapsed since 22:00 UT.	113
5.6	The Learmonth radio spectrograms. Three lanes of fundamental emission are indicated by F1, F2 and F3. Three lanes of harmonic emission are indicated by H1, H2 and H3. Four discrete regions of enhanced emission are indicated by R1, R2, R3 and R4. The time axis refers to the time elapsed since 22:00 UT.	114
5.7	Panel a): a 131 Å image showing three separate components of the expanding CME labelled as C1, C2 and C3. Panel b) and c): 211 Å images with the CME and the leading edge which precedes it indicated in orange in panel b) and red in the difference image in panel c). The solid green line in panel b) indicates the position of the slit used to analyse the expanding feature ahead of the CME.	114
5.8	A TD map from the 211 Å running difference images, formed from the slit marked in panel b) of Fig. 5.7. The red points and linear fit mark the propagating feature, corresponding to a speed of 500 km s ⁻¹ . The time axis refers to the time elapsed since 22:00 UT.	115
5.9	A schematic synopsis of the event. A flare occurs which is followed by a CME comprising of the leading edge or EUV wave (green) and the main CME plasmoid (blue). A funnel structure (red) within the active region is seen to host a series of rapidly propagating quasi-periodic waves. A brightening is observed at the base of this structure and is interpreted as a reconnection site. After a certain delay periodic radio sparks are observed, which occur at an estimated height consistent with the leading feature of the CME, and a periodicity consistent with the fast wave period.	117
5.10	An overview of the numerical setup, showing the centre of the domain (the full domain is 300 length units in both directions). The density structure is shown, with white corresponding to the internal density of 4, and black to the external density of 1. The blue arrow denotes the direction of the uniform magnetic field. The red arrows denote the position and direction of the initial velocity perturbation.	122

5.11	Snapshot of a region of the numerical domain for the largest amplitude initial perturbation ($v_{y0}/C_{Ae} = 1.5$) showing the density perturbation towards the end of the simulation run-time. The leaky and guided components are labelled. The red asterisks show the locations where the time series are taken for the guided and leaky wave trains.	124
5.12	Top: the absolute density at time $t = 125$ in the region of the numerical domain around the density enhancement. Bottom: the one dimensional density profile at $y = 0$ in the top panel.	125
5.13	Dependence of the maximum amplitude of the leaky wave train measured at $x = 0$ on propagation distance y for different amplitudes of the initial perturbation.	127
5.14	Guided wave train time series and wavelet analysis for different amplitude initial perturbations. The applied perturbation amplitude, v_{y0}/C_{Ae} , is 0:004 (top), 0:30 (middle), and 1:50 (bottom).	128
5.15	Leaky wave train time series and wavelet analysis for different amplitude initial perturbations. The applied perturbation amplitude, v_{y0}/C_{Ae} , is 0:004 (top), 0:30 (middle), and 1:50 (bottom).	129

Acknowledgments

Firstly, I would like to thank my supervisor, Valery Nakariakov, for his continuous support and enthusiasm throughout the course of my PhD. This included fruitful suggestions for changes in research direction and the opportunity to attend conferences and research meetings in far flung places. Importantly, being part of his research team allowed me to gain knowledge from, and collaborate with, his Post-docs past and present. I would like to thank my collaborators in Warwick and further afield for their time and valuable contributions to the research presented in this thesis. Next I would like to thank my parents for their continued support and encouragement throughout my education. This ranges from dropping me off at Warwick when I first started 8 years ago, to my Dad proof reading the introduction of this thesis. Finally, I would like to thank the other PhD students in CFSA, and more broadly in Physics, for providing welcome distractions and encouragement throughout my PhD. This can also be said of the wonderful members of the Warwick Mountains club.

This thesis was typeset with L^AT_EX 2_ε¹ by the author.

¹L^AT_EX 2_ε is an extension of L^AT_EX. L^AT_EX is a collection of macros for T_EX. T_EX is a trademark of the American Mathematical Society. The style package warwickthesis was used.

Declarations

This thesis is submitted to the University of Warwick in support of the authors application for the degree of Doctor of Philosophy. It has been composed by the author and has not been submitted in any previous application for any degree or other university. The following published papers were first authored by the author of this thesis, as such all figures and text in the corresponding chapters and sections is the original work of the author.

- ‘*A statistical study of decaying kink oscillations detected using SDO/AIA*’, Goddard, C. R., Nisticó, G., Nakariakov, V. M., Zimovets, I. V., 2016, AA. G. Nisticó provided aid with the data analysis. I.V Zimovets provided the kink oscillation catalogue, and useful discussions. Presented in Chapter 2.
- ‘*Dependence of kink oscillation damping on the amplitude*’, Goddard, C. R.; Nakariakov, V. M., 2016AA...590L...5G. Presented in Chapter 2
- ‘*A statistical study of the inferred transverse density profile of coronal loop threads observed with SDO/AIA*’, Goddard, C. R.; Pascoe, D. J.; Anfinogentov, S.; Nakariakov, V. M., 2017AA...605A..65G. D. Pascoe provided aid with the implementation of the forward modelling procedure. S. Anfinogentov wrote the MCMC Bayesian inference code used. Presented in Chapter 4
- ‘*Observation of quasi-periodic solar radio bursts associated with propagating fast-mode waves*’, Goddard, C. R.; Nisticó, G.; Nakariakov, V. M.; Zimovets, I. V.; White, S. M. 2016AA...594A..96G. G. Nisticó provided aid in the data analysis, and useful discussion. S. M. White provided aid in the acquisition and interpretation of the radio spectrographs. I.V Zimovets provided useful discussion. Presented in Chapter 5.

The following published papers were second authored by the thesis author, and significant contribution to the research was made. Figures in these works were not produced by the author unless listed below, and are presented with the first authors permission. The text in the corresponding sections is based on the text from the respective papers, with the first authors permission.

- ‘*Damping profile of standing kink oscillations observed by SDO/AIA*’, Pascoe, D. J., Goddard, C. R., Nisticó, G., Anfinogentov, S., Nakariakov, V. M., 2016, AA, 585, L6. Wrote sections of the text and produced Figs. 3.1 and 3.2. Presented in Section. 3.2.
- ‘*Coronal loop density profile estimated by forward modelling of EUV intensity*’, Pascoe, D. J.; Goddard, C. R.; Anfinogentov, S.; Nakariakov, V. M., 2017AA...600L...7P. Produced left panel of Fig. 3.9. Presented in Section. 3.5.
- ‘*Dispersive Evolution of Nonlinear Fast Magnetoacoustic Wave Trains*’, Pascoe, D. J.; Goddard, C. R.; Nakariakov, V. M., 2017ApJ...847L..21P. Ran all numerical simulations and produced all figures. Presented in Section. 5.7.

The author was involved in the following co-authored papers, they are briefly included with the first authors permission as they are based on some of the work presented in this thesis, and relevant to discussions throughout the thesis.

- ‘*Coronal loop seismology using damping of standing kink oscillations by mode coupling*’, Pascoe, D. J.; Goddard, C. R.; Nisticó, G.; Anfinogentov, S.; Nakariakov, V. M., 2016AA...589A.136P. Presented in Section. 3.3.
- ‘*Coronal loop seismology using damping of standing kink oscillations by mode coupling. II. additional physical effects and Bayesian analysis*’, Pascoe, D. J.; Anfinogentov, S.; Nisticó, G.; Goddard, C. R.; Nakariakov, V. M. 2017AA...600A..78P. Presented in Section. 3.4.

Abstract

Perturbations of coronal structures by impulsive events such as solar flares generate waves which are interpreted with MHD theory. These waves allow plasma processes to be studied, and seismology of the local plasma parameters to be performed. The focus of this thesis is the detailed observational study of these waves.

A statistically significant number of kink oscillations of coronal loops were analysed. The measured periods scale linearly with the estimated loop length, as expected from the standard interpretation of the waves as the global fundamental standing mode. A typical kink speed of $C_k=(1300\pm50)$ kms⁻¹ is obtained. A linear scaling of the damping time with period is observed, and non-exponential damping profiles were noted. The study was then extended to determine if there is any scaling between the quality factor of the oscillations and the oscillation amplitude. Selected events from the kink oscillation catalogue were analysed in detail, and it was found that the damping profiles of several oscillations were better fit by a Gaussian envelope than an exponential one. These damping profiles were then used to perform seismological inversions, including the transverse density structure of the loops. The obtained transverse density profile was compared to the observed intensity profile for one loop, using forward modelling and Bayesian inference, where good agreement was found.

The intensity cross-sections of 233 coronal loops were analysed. Assuming an isothermal and cylindrical cross-section the transverse density structure of the coronal loop plasma was inferred. Several models for the transverse density profile were quantitatively compared. Very strong evidence was found for the existence of an inhomogeneous layer where the density varies smoothly between the rarefied background plasma and the dense centre of the loop. In a significant number of cases the width of this layer was high enough to conclude that the loop does not have a core at all and has a continuously varying transverse density profile.

Finally, a flaring event was analysed which excites a series of propagating EUV intensity perturbations, and simultaneously produces a series of features in radio spectrometer data. This is the first observation which links quasi-periodic fast waves observed in the EUV band to quasi-periodic features in radio spectra. 2D numerical simulations of impulsively generated wave trains in coronal density enhancements are presented. This aims to establish how these waves are affected by initial perturbations which enter the non-linear regime, thereby establishing the feasibility of some of the mechanisms by which the observations presented could be explained.

Chapter 1

Introduction

1.1 The Sun

The Sun has been worshipped, philosophised over and studied throughout human history, and our knowledge of it has accelerated rapidly over the last 100 years. The Sun was formed around 4.5 billion years ago and it is currently in the main sequence phase of its life-cycle, after which it will expand and become a red giant, engulfing its nearest planets. It has a mass of 2×10^{30} kg, and a radius 6.96×10^8 m. The plasma that the Sun is comprised of is largely Hydrogen, and a small amount of Helium, in various states of ionisation depending on the local temperature.

1.1.1 The solar interior

Our knowledge of the Sun's interior comes from indirect sources. These indirect observations have been combined with direct observables to create a Standard Solar Model (SSM) [e.g. [Lodders, 2003](#)], which assumes the Sun is perfectly spherical and that the effects of the rotation and magnetic field can be ignored. Measurements of the solar neutrino flux can be made from Earth, and let us probe the nature of the fusion reactions which occur in the core. Initially there was a deficit in the detected neutrino flux compared to the predicted value from the SSM, known as the solar neutrino problem. This was solved by neutrino oscillations [[Ahmad et al., 2001](#)].

The fusion reactions occurring in the Sun's core produce energy which is eventually emitted as photons from the solar surface, as well as the energy which drives energetic and dynamic processes higher in its atmosphere. The temperature of the Sun's core is ≈ 15 MK. Above the inner core lies the radiative zone. Here the energy from the fusion reactions is transferred to the upper layers via radiative diffusion, which takes over 100,000 years. At the boundary of the next layer, the convection zone, the temperature has dropped to 1.5 MK. As the name suggests, in this layer the energy transport and plasma dynamics are dominated by convection

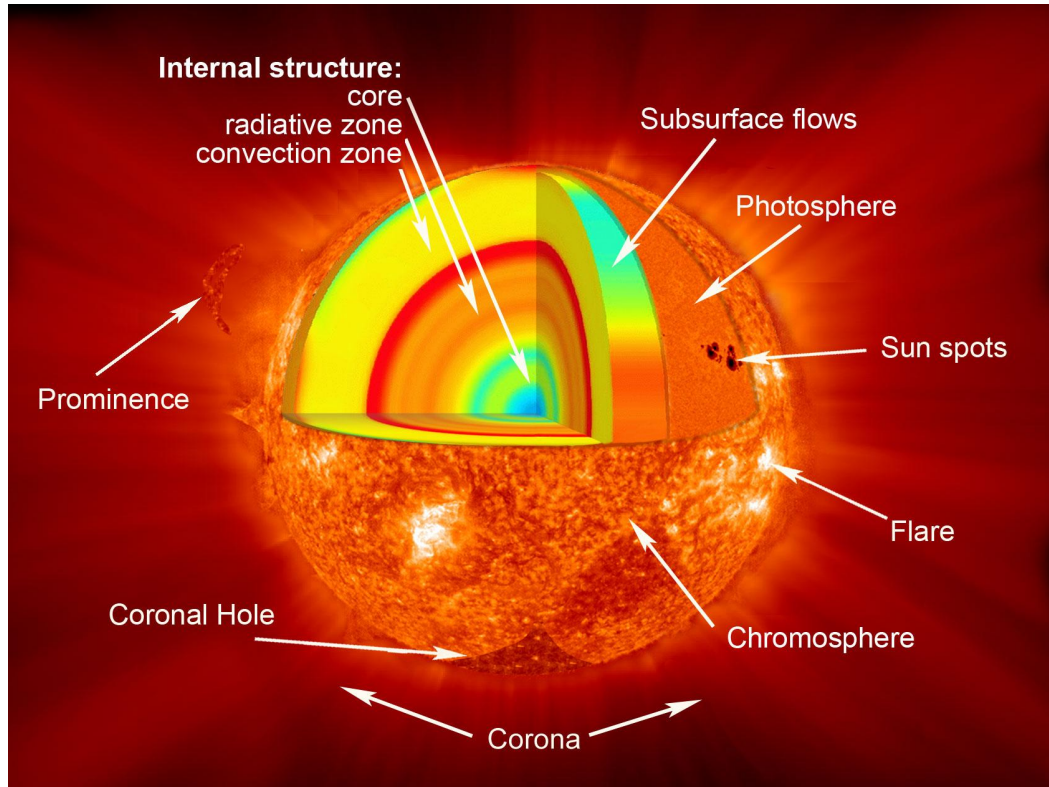


Figure 1.1: The structure of the solar interior. Courtesy of NASA.

cells. This is the last layer of the solar interior, before the solar atmosphere is reached. These interior layers are shown in Fig. 1.1.

Helioseismology uses acoustic wave modes (or p modes), which have the pressure gradient as their main restoring force, to probe the interior and the processes that occur there [e.g [Deubner & Gough, 1984](#)]. The waves are excited by fluid turbulence in the convective zone and allow us to probe the region below the photosphere (the visible surface). The sound speed changes with depth in the solar interior, meaning that waves with different frequencies are refracted at different depths. Local helioseismology (in contrast to global) is used to study local features such as sunspots by interpreting the full wave field measured at the surface [e.g [Gizon et al., 2010](#)].

1.1.2 The solar atmosphere

There are order of magnitude variations of the temperature in the Sun's atmosphere, plotted in Fig. 1.2. The solar atmosphere begins with the photosphere, which has a temperature of less than 10,000 K. The majority of the energy from the Sun is emitted from this layer as white light, as the photosphere is transparent to visible wavelengths. Hence, it is the first directly observable section of the Sun. The

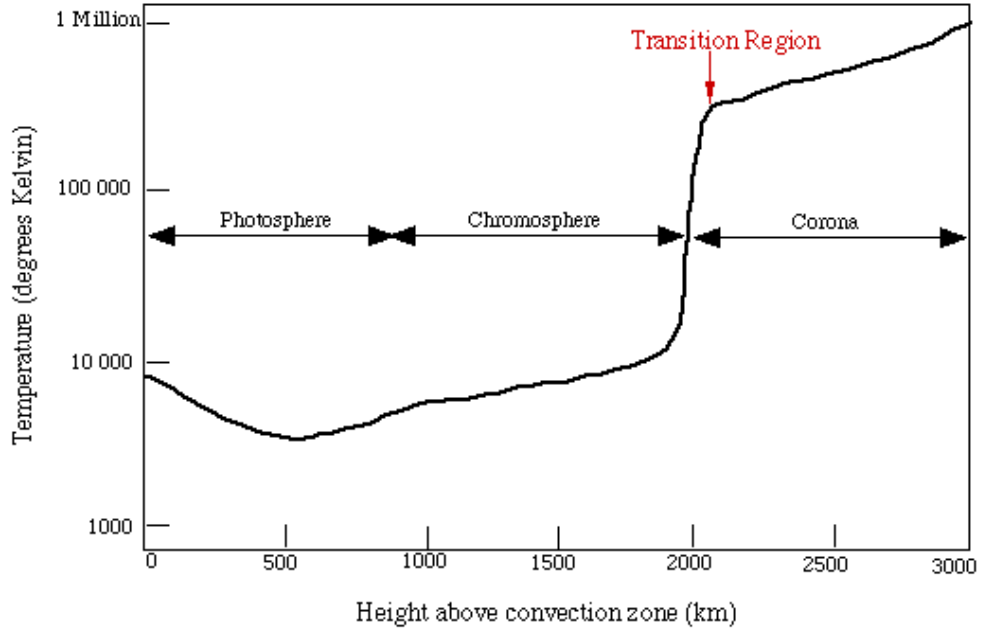


Figure 1.2: Solar temperature plot. Courtesy of MSU.

influence of the Sun's strong and dynamic magnetic field can be observed here, with the presence of magnetic features such as sunspots and faculae. Sunspots appear as dark regions due to their enhanced magnetic field, whereas faculae appear as brightenings in the vicinity of sunspots. Granulation patterns can also be seen in the photosphere, which are caused by convection cells in the convection zone below (Fig. 1.3). Much of our knowledge about the Sun's magnetic field comes from this layer, as instruments such as the Helioseismic and Magnetic Imager (HMI) on the Solar Dynamics Observatory (SDO) [Lemen et al., 2012] produce magnetograms, showing the distribution and polarity of the magnetic field. An example is shown in Fig. 1.4.

Above the photosphere is the chromosphere. This layer extends 2000–3000 km above the temperature minimum in the photosphere. Here the main emission is from the H-alpha line of the hydrogen atoms in the plasma, which has a wavelength peaking at 656.28 nm. The temperature here is higher than in the photosphere, as can be seen in the temperature plot in Fig. 1.2. Neutral Hydrogen still exists at chromospheric temperatures, so the plasma is partially ionised. The dynamics here are dominated by strong convection and granulation can be seen, as in the photosphere. In this layer structuring of the plasma due to the magnetic field is evident, such as loops and prominences, which can be formed here by hot plasma upflows and eruptions from below.

The transition region lies between the chromosphere and the corona. It

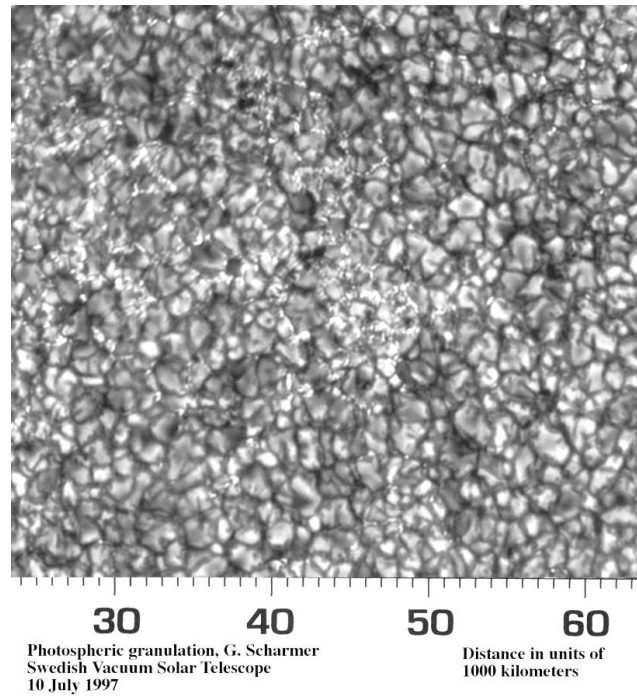


Figure 1.3: Granulation in the photosphere. Courtesy of NASA.

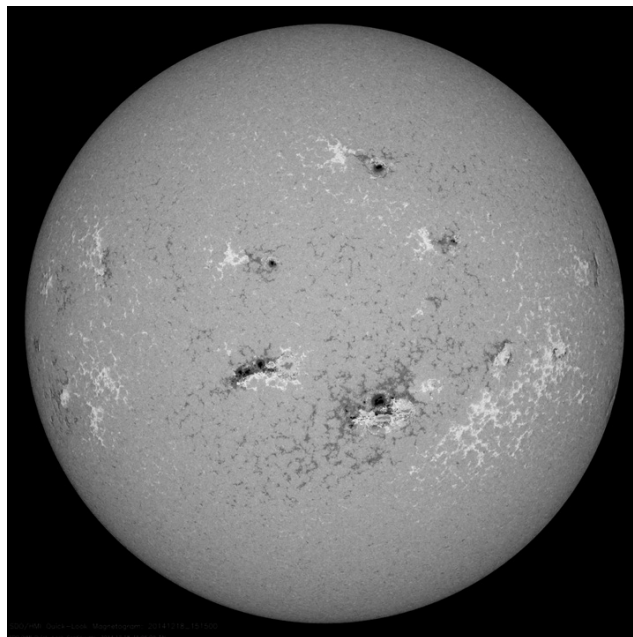


Figure 1.4: A HMI magnetogram. Courtesy of NASA.

is a very thin layer (≈ 100 km) where the plasma becomes fully ionised and the temperature increases rapidly in the radial direction.

The corona is the outer layer of the Sun’s atmosphere and extends up to several solar radii out from the solar surface. The temperature here is of a comparable magnitude to the temperature in the core (> 1 MK). This was first noted in the 19th century via observations of emission lines from highly ionised iron [see [Vand, 1943](#)]. Despite the thermal emission of the coronal plasma peaking at EUV wavelengths, the corona can be clearly imaged during eclipses via scattered white light (Fig. 1.5). The structure of the plasma here is determined by the magnetic field. EUV imagers typically image the corona at different wavelengths, corresponding to different temperature ranges. An example image is shown in the lower panel of Fig. 1.5. The corona can be divided into three main regions; active regions, coronal holes and quiet Sun regions. Active regions are highly structured and dynamic, and are formed as a result of emerging magnetic flux from lower in the Sun, which will now be discussed.

1.1.3 Magnetic field and solar cycle

Sunspots on the solar surface have been recorded for hundreds of years. These are regions of enhanced magnetic field, which appear as dark regions on the photosphere. From variations in the number of sunspots the 11 year solar cycle was discovered, often plotted as the well known butterfly diagram (Fig. 1.6). This clearly shows the solar cycle, and how the locations of emerging sunspots, and therefore the overlying active regions, drift from high latitudes at the start of each cycle towards the equator. The polarity of the two hemispheres is flipped every 11 years and so the full cycle is 22 years, known as the Hale cycle. Evidence for the solar cycle can also be seen using helioseismology. It causes a modulation in the frequencies of the p modes [[Broomhall et al., 2009](#)], linking the variation in the sunspots on the surface to processes deeper in the interior. The solar cycle is of high importance as the solar activity discussed in the next section varies strongly over the 11 years.

It is widely accepted that the solar cycle is caused by the solar dynamo, which is the mechanism that generates the Sun’s strong magnetic field. Due to the more gaseous nature of the outer layers of the solar interior the Sun experiences differential rotation. The high latitude regions rotate slower than the equatorial regions causing the magnetic field generated in the tachocline to shear and twist. This creates complex magnetic structures and regions of amplified magnetic field strength, which emerge as sunspots and active regions higher in the Sun’s atmosphere. Additionally this generates small scale magnetic elements covering the entire surface. The efficiency of this process varies during the solar cycle. The magnetic field structure that is generated can be directly observed in the photosphere via magnetograms,

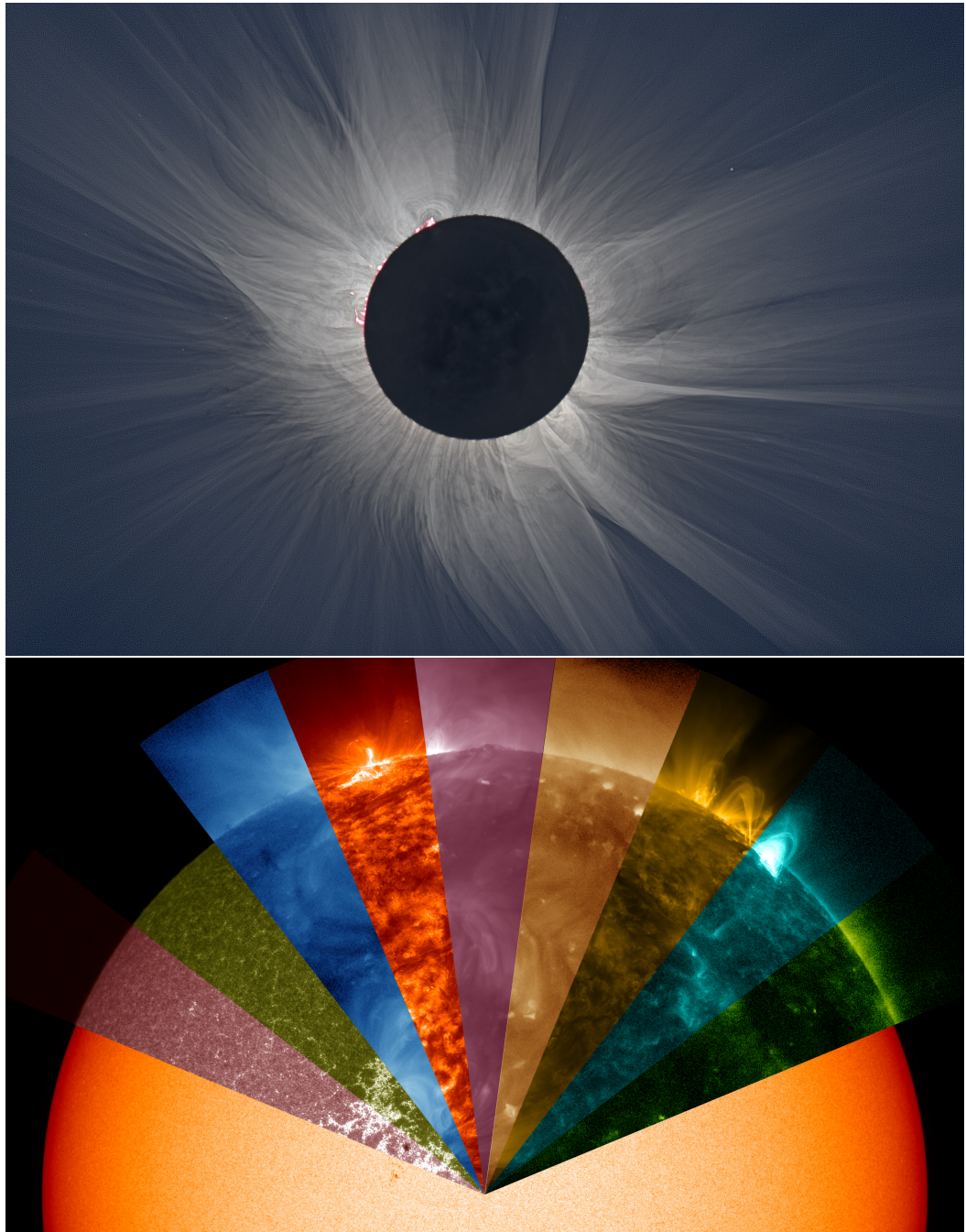


Figure 1.5: Top: the corona imaged in white light during an eclipse. Bottom: the corona and lower layers imaged in multiple EUV wavelengths. From left to right these are; 1700 Å (photosphere), 1600 Å (upper photosphere and transition region), 335 Å (corona), 304 Å (chromosphere), 211 Å (corona), 193 Å (corona), 171 Å (corona), 131 Å (corona) and 94 Å (corona). The background segment is the white light continuum emission from HMI. Courtesy of NASA.

DAILY SUNSPOT AREA AVERAGED OVER INDIVIDUAL SOLAR ROTATIONS

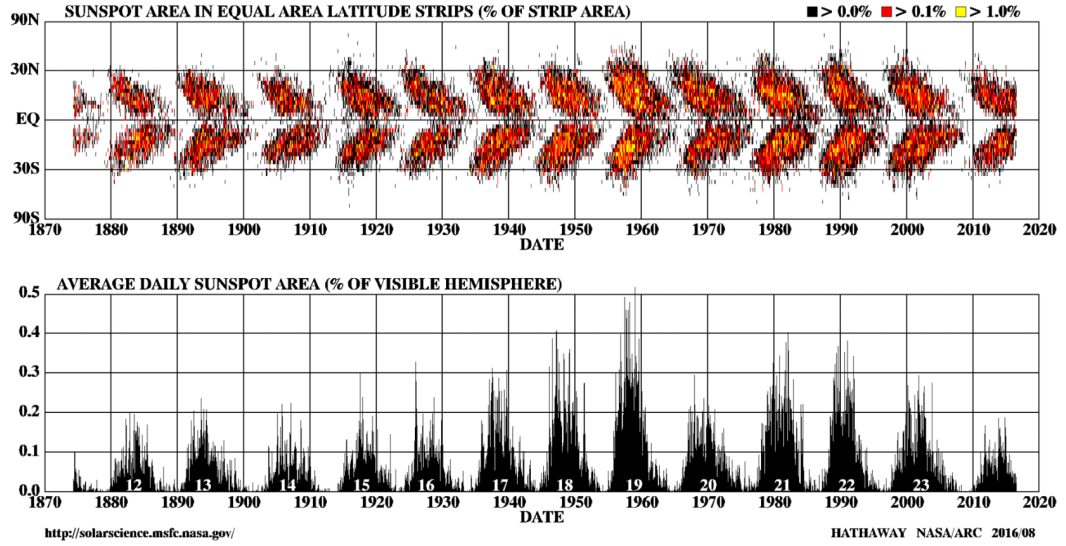


Figure 1.6: Top: the butterfly diagram, which shows the evolution of sunspots locations in latitude over time. Bottom: the average sunspot area as a percentage of the visible solar hemisphere. Both data sets clearly show the 11 year solar cycle. Courtesy of NASA.

and indirectly in the chromosphere and corona via the structuring of the plasma which is believed to highlight magnetic field lines.

1.1.4 Active regions and coronal loops

Active regions appear in the Sun's atmosphere where the complex magnetic field structures generated in the convection zone emerge from below. They are seen in the corona as bright regions with complex networks of arc shaped structures which are known as coronal loops (see Fig. 1.8), and normally lie above sunspots observed in the photosphere. The magnetic field topology often becomes unstable, resulting in eruptions and flares which release some of the stored magnetic energy.

Coronal loops are one of the most obvious consequences of the dominance of the magnetic pressure over the gas pressure in solar active regions. They are considered to be cylindrical tubes of plasma which follow the curvature of magnetic field lines. This makes them useful in testing magnetic field extrapolation codes which are based on the magnetic field measured in the photosphere [e.g. [Wiegmann & Sakurai, 2012](#)]. There are many poorly understood aspects of coronal loops and the Magnetohydrodynamic (MHD) oscillations they undergo, making their study compelling. They are normally considered to be overdense [[Aschwanden, 2005](#)], compared to the expected density due to hydrostatic pressure balance, and are often modelled as having a uniform core surrounded by a layer where the density

varies between the external and internal values.

Loops can be categorised based on their average temperature. Generally these are; cool loops (< 1 MK), warm loops (≈ 1 MK) and hot loops (> 1 MK) [Reale, 2010]. The exact determination of a loop's internal temperature, how it varies along the length of the loop, and its comparison to the external temperature are still topics of research and debate. Analysed coronal loops have been found to range from near isothermal to highly multi-thermal. Aschwanden & Boerner [2011] performed a systematic study of the cross-sectional temperature structure of coronal loops using the Atmospheric Imaging Assembly (AIA) on the Solar Dynamics Observatory [SDO; Lemen et al., 2012], finding evidence for near isothermal loop cross-sections. High-resolution Coronal Imager (Hi-C) data was used to measure the Gaussian widths of multiple loops, finding a distribution that peaked at 270 km, the temperature distributions were also found to be narrow [Brooks et al., 2013]. Further examples for narrow temperature ranges in coronal loops include [e.g. Warren et al., 2008]. However, there are many examples of multi-thermal loops [Schmelz et al., 2010; Nisticò et al., 2014a, 2017] and hot flaring loops are also multi-thermal [Aschwanden, 2005].

The unresolved sub-structure of coronal loops is also debated, i.e loops (or threads) which appear monolithic may be comprised of multiple smaller threads with a certain filling factor. Despite numerous studies using multiple instruments no clear consensus has been reached [e.g. Reale et al., 2011; Brooks et al., 2012; Peter et al., 2013; Brooks et al., 2016]. However, it appears the lower limit of thread widths is close to being resolved, with a lower limit of 100 km predicted [Aschwanden & Peter, 2017].

1.1.5 Solar activity

Solar flares are energetic events where magnetic energy is released and cause heating and the generation of energetic particles [see reviews by Shibata & Magara, 2011; Fletcher et al., 2011]. The first recorded observation of a solar flare was in white light, despite the majority of the flare energy being released at other wavelengths. The Carrington Flare occurred in 1859, and remains the strongest solar flare recorded. Flares mostly occur in active regions and so their occurrence rate also varies with the solar cycle. Coronal mass ejections (CMEs) often occur during solar flares [e.g. Chen, 2011; Webb & Howard, 2012]. They are releases of magnetic field and plasma from the corona, but occur due to emergence of magnetic field structures from deeper in the Sun. Understanding and predicting these phenomena is important as they can affect the local environment around Earth. The effects of this include the generation of Aurora, the damaging of satellites and even the disruption of power grids. Due to their intrinsic link to solar flares and active regions their occurrence rate also varies

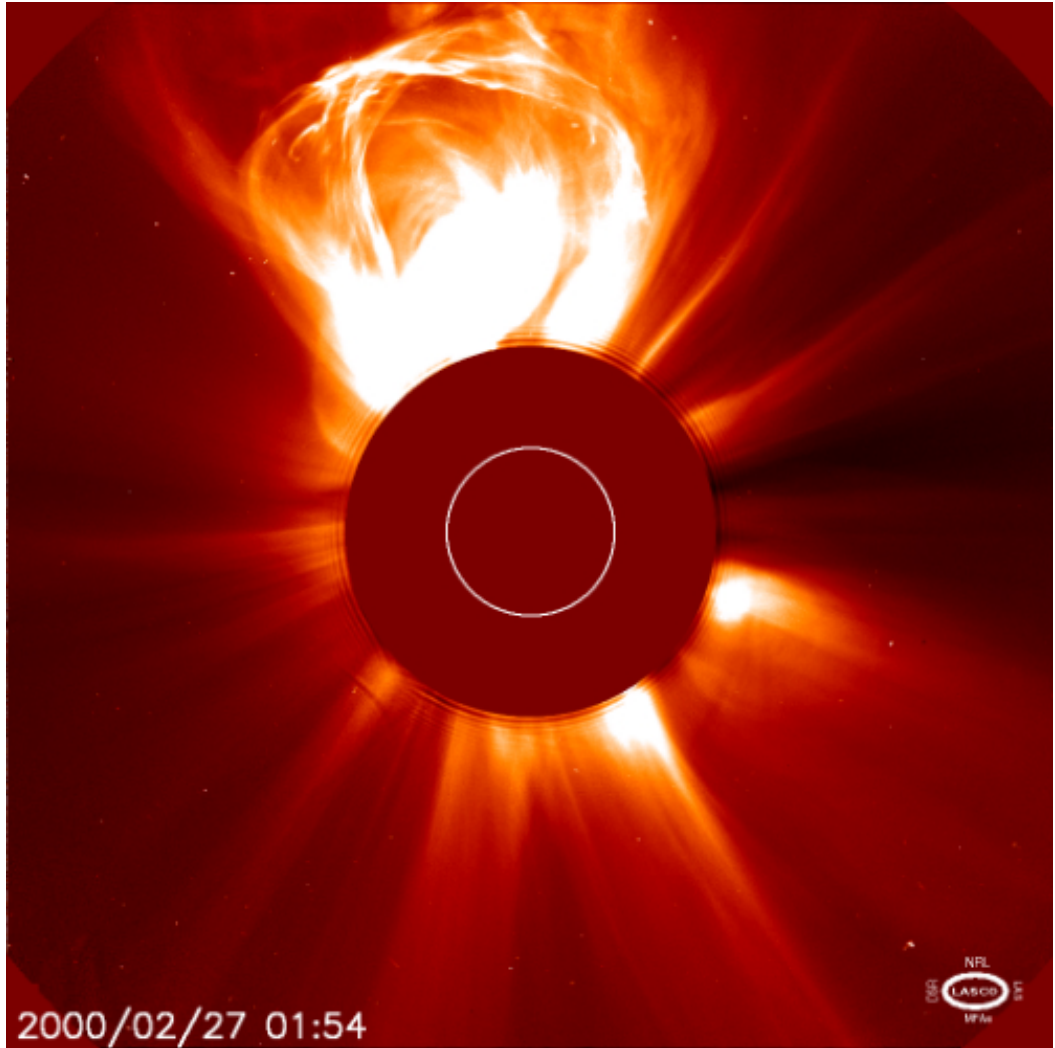


Figure 1.7: A CME imaged by the SOHO satellite. Courtesy of NASA/ESA.

with the solar cycle.

Another form of solar activity is the solar wind. In contrast to the phenomena described above this is a more constant effect. There is a continuous stream of charged particles released from the Sun's atmosphere, in two components, the fast and slow solar wind. The slow solar wind appears to emanate from the streamer belt, at mid latitudes, whereas the fast solar wind seems to dominate in the polar regions, where coronal holes are found. There is still variance of the wind with solar activity, as active regions release a flux of charged particles during flares and CMEs. The solar wind is also subject to interesting MHD wave behaviour [see [Ofman, 2010](#)].

Events such as flares and CMEs cause strong localised heating and impulsive perturbations to the coronal plasma and magnetic field. As such they can drive waves and oscillations in coronal structures, which will be discussed in Section 1.2.

1.1.6 Gaps in our understanding

Despite the significant progress made in solar physics over several decades, a number of fundamental questions remain unanswered. It is not understood why the solar corona is more than an order of magnitude hotter than the chromosphere below it, and the mechanism for this heating has been the subject of countless studies and conjectures. Waves and oscillations must deposit some energy in the corona, however current observations of MHD waves indicate that it is only a small fraction of the energy needed to continuously heat the corona [e.g. Klimchuk, 2015]. The acceleration of the fast solar wind is another unsolved problem, as is the exact nature of solar flares and eruptions.

More specific questions relate to the waves and oscillations observed on the Sun, and the nature of the structures in which they are observed. Quasi-Periodic Pulsations (QPP's) have been detected in solar and stellar flares, and conclusive evidence as to the source of this periodicity has not been found. One potential mechanism is modulation of the flare emission via MHD waves, introduced in Section 1.3. The formation and equilibrium conditions of coronal loops are still a debated topic, as well as their internal structure. The resolution of these questions may be aided through studies of MHD wave modes seen in coronal loops. There are also observed waves which are poorly understood, and their seismological potential is yet to be unlocked. The study of waves and oscillations in the corona, and the coronal waveguides in which they propagate will be the focus of this thesis.

1.2 Coronal waves and oscillations

The corona of the Sun is highly structured due to the influence of the magnetic field emerging from lower in the atmosphere. The dominance of the magnetic field over the gas pressure causes it to determine the spatial distribution of the plasma. This forms closed structures such as prominences and coronal loops (see Fig. 1.8, and the red field lines in Fig. 1.9), as well as structures with open magnetic field lines such as coronal holes and funnels (see the green field lines in Fig. 1.9). These structures can act as wave guides for MHD waves and oscillations (see Section 1.3).

Dynamic events such as solar flares and CMEs (see Section 1.1) occur in the solar corona. These events can trigger waves and oscillations in coronal wave guides. An intensively studied example are kink, or transverse, oscillations of coronal loops, one of the focuses of this thesis and discussed further in Section 1.4. Other wave activity includes global EUV waves [e.g. Patsourakos et al., 2009; Gallagher & Long, 2011], and their coronal and chromospheric counterparts [e.g. Moreton, 1960; Chen et al., 2005; Warmuth, 2015], propagating and standing slow magnetoacoustic waves [e.g. De Moortel, 2009; Wang, 2011] and rapidly propagating quasi-periodic wave

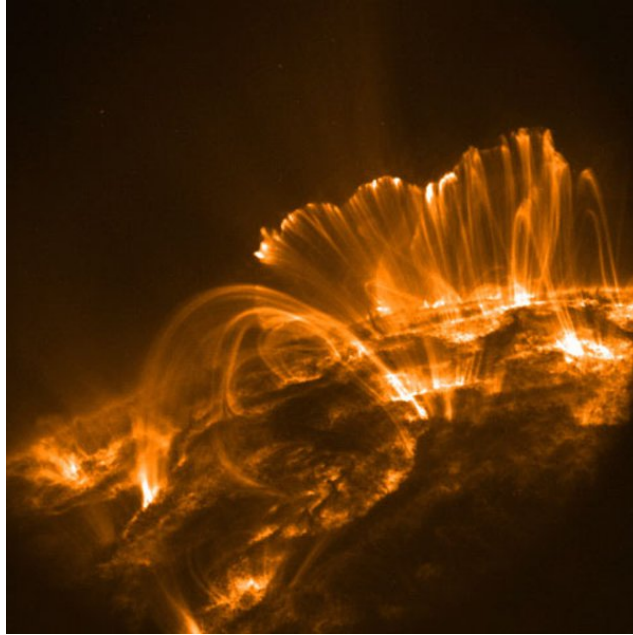


Figure 1.8: A collection of coronal loops imaged with AIA/SDO. Courtesy of NASA.

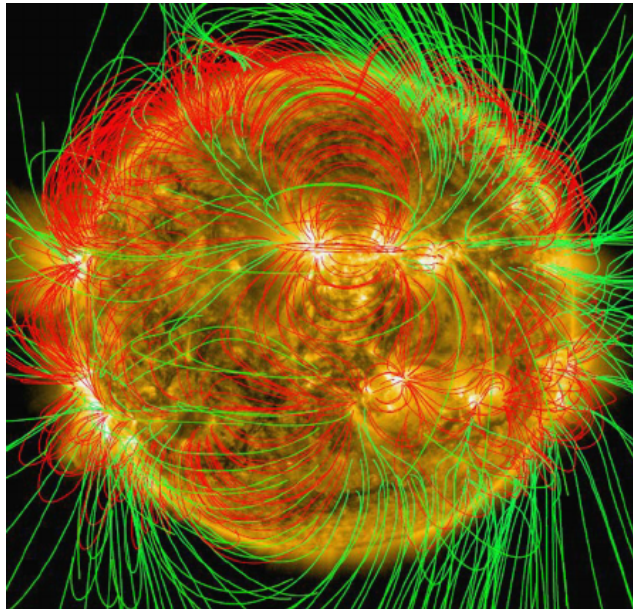


Figure 1.9: A global coronal magnetic field extrapolation for open (green) and closed (red) magnetic field lines [[Wiegmann et al., 2017](#)].

trains [e.g. [Liu et al., 2011](#)] discussed further in Section 1.5.

The detection of waves in the corona can be difficult. The typical spatial scale of coronal structures may determine the wavelength and therefore the period of the waves they exhibit. This results in periods ranging from several seconds up to several minutes. For spatial imaging of these waves sufficient cadence to resolve a few points per wave period is required, as well as sufficient spatial resolution to resolve the wavelength. The seminal EUV imager was the Transition Region and Coronal Explorer (TRACE) [[Handy et al., 1999](#)] which was launched in 1998 and operated at EUV wavelengths, obtaining its last science image in 2010. This has subsequently been superseded by modern instruments, such as SDO/AIA, the focus of Section 1.7.

The interest in wave activity in the Sun’s atmosphere stems from several sources. It serves as a natural laboratory for the study of plasma waves and processes. This can supplement studies performed with laboratory plasmas, or the understanding of other solar system plasmas and beyond. MHD waves in the Sun’s atmosphere have been intensively studied over the last 30 years, often in the context of the coronal heating problem and the acceleration of the fast solar wind. In addition, there has been a growing interest in performing seismology with these waves, known as MHD seismology.

To study the processes which occur in the Sun’s atmosphere in more detail accurate knowledge of the local plasma environment is required. This includes the magnetic field, temperature and density, as well as the gradients of these parameters in certain locations. The exact value of the coronal magnetic field remains unknown, because of intrinsic difficulties with direct methods (e.g., Zeeman splitting and gyroresonant emission). Extrapolations of the magnetic field from magnetograms still have unknown uncertainty and do not perform well for specific small scale features. There is expected to be a large variance of the magnetic field within different regions of the corona, both large and small scale. Additionally, specific coronal transport coefficients, such as the shear viscosity, resistivity, and thermal conduction, are still not accurately determined, especially locally in different coronal structures. Finally, it is believed that many coronal structures observed may have unresolved sub-structure, which may also be probed by using MHD waves and oscillations.

The idea of MHD seismology is most often seen in the context of coronal seismology [see [Nakariakov & Verwichte, 2005](#); [De Moortel & Nakariakov, 2012](#); [Liu & Ofman, 2014](#), for comprehensive reviews]. It is similar to helioseismology of the solar interior using sound waves, however there are three main MHD waves (introduced in Section 1.3) with very different properties in different coronal structures. The detection and analysis of waves and oscillations in the corona combined with analytic theory or numerical modelling of the wave modes involved can allow local plasma

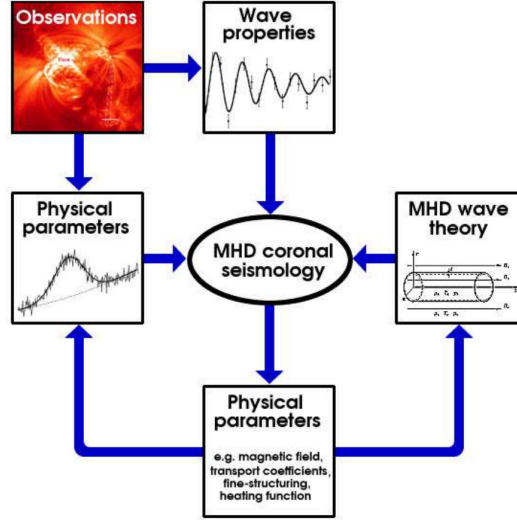


Figure 1.10: The methodology of MHD coronal seismology [Nakariakov & Verwichte, 2005].

parameters to be determined, such as those mentioned above. This method was first suggested in Uchida [1970] and Roberts et al. [1984] and the general methodology is represented in Fig. 1.10. It has since been applied to numerous different types of waves and oscillations in different coronal structures. As observations as well as theory advance, the opportunity to perform more complex seismological inversions from the wave properties has arisen. The details are discussed in detail in Section 1.4.3, and related results will be presented in Section 3.

1.3 MHD description of coronal plasma

Magnetohydrodynamics (MHD) is the approach used to describe the dynamics of an electrically conductive fluid. The plasma of the Sun's atmosphere can be modelled and understood with such an approach if certain conditions are fulfilled. The structuring of the Sun's atmosphere is on a scale many orders of magnitude higher than individual electrons and ions that the plasma is comprised of, and an extremely large number of particles fill the studied volumes. This makes the modelling of the individual particles impossible, however this is not necessary in MHD. The use of this approach requires the following:

- Characteristic velocities are non-relativistic (i.e $v \ll c$).
- Characteristic length scales are significantly higher than the ion Larmor radius (i.e $L \gg r_{li}$).
- Characteristic time scales are significantly longer than the ion gyro-period (i.e

$$T \gg p_{gi}).$$

- The assumption of quasi-neutrality should be applicable, i.e the total net charge of the plasma should be zero.

In other words the plasma must be Maxwellian and describable by hydrodynamics. In the coronal plasma $r_{li} < 10$ km and $p_{gi} < 10^{-4}$ s for the majority of physical parameter combinations [Nakariakov & Verwichte, 2005]. As such, it is appropriate to describe large scale, slow plasma motions in the corona with MHD. First the set of governing equations will be set out before considering how MHD can be applied to the coronal plasma. This can be done by combining the equations of fluid mechanics and Maxwell's equations of electrodynamics. Derivations of the following equations are readily available [e.g Aschwanden, 2005].

The MHD equations can be written as follows. Mass (particle) conservation;

$$\frac{\partial \rho}{\partial t} + \nabla \cdot (\rho \mathbf{v}) = 0. \quad (1.1)$$

The momentum equation;

$$\rho \frac{\partial \mathbf{v}}{\partial t} + \rho(\mathbf{v} \cdot \nabla) \mathbf{v} = -\nabla p - \rho \mathbf{g} + \mathbf{j} \times \mathbf{B} + F. \quad (1.2)$$

The induction equation;

$$\frac{\partial \mathbf{B}}{\partial t} = \nabla \times (\mathbf{v} \times \mathbf{B}) + \eta \nabla^2 \mathbf{B}. \quad (1.3)$$

Energy conservation;

$$\frac{\rho^\gamma}{\gamma - 1} \frac{d}{dt} \left(\frac{p}{\rho^\gamma} \right) = -L. \quad (1.4)$$

Here ρ is the total plasma density which is given by $\rho = n_e m_p$ if quasi-neutrality is assumed and $m_p \gg m_e$ is taken. \mathbf{v} is bulk velocity, p is the isotropic pressure, \mathbf{B} is the vector magnetic field, γ is the adiabatic index (usually taken to be 5/3 in the solar corona), \mathbf{g} is the gravitational field vector, F represents any additional forces (e.g viscosity), \mathbf{j} is the electric current density, η is the magnetic resistivity and L is the energy loss (or gain) function. When $\eta = 0$, as well as any other coefficients such as viscosity and thermal conductivity, this is ideal MHD, which is considered in this thesis.

It is also important to mention the frozen-in condition. This states that the number of magnetic field lines passing through a closed surface must remain constant. This has the implication that moving magnetic field lines will cause the local plasma to be 'dragged' with them, and vice versa. This can be expressed

mathematically as;

$$\Phi = \int_S \mathbf{B} \cdot d\mathbf{A} = \text{const}, \quad (1.5)$$

where Φ is the flux, S is a closed surface, and \mathbf{A} defines an area vector normal to the closed surface S .

A relevant quantity to define which has been mentioned numerous time is the plasma beta (β). This is the ratio of the gas and magnetic pressure;

$$\beta = \frac{p}{B^2/2\mu_0}. \quad (1.6)$$

This quantity can be used to determine if the plasma dynamics will be dominated by thermal effects or the magnetic field. In some circumstances it can be used as a proxy for the stability of a given plasma system, such as the solar active regions mentioned above. This is important, when considered with the frozen-in condition it means that the plasma observed should trace out magnetic fields lines, and that magnetic field eruptions result in eruptions of plasma. The plasma β in active regions and coronal loops is usually taken to be small, around 0.1 and 0.01 respectively, although it may increase during flaring and eruptive events.

1.3.1 MHD waves

The description of MHD waves begins by considering a uniform plasma (with constant density ρ_0 , and pressure p_0) within a uniform magnetic field oriented in an arbitrary direction with a magnitude B_0 , in a stationary equilibrium. A perturbation of the form $p = p_0 + p_1$ is applied, and quadratic and higher order terms are ignored. This results in linear equations which can be Fourier decomposed in the form;

$$p_1(\mathbf{r}, t) = \delta p_0 e^{i(\mathbf{k} \cdot \mathbf{r} - \omega t)}, \quad (1.7)$$

where r is the spatial coordinate and t the temporal. ω corresponds to the wave frequency and k the wavenumber. This results in a linear set of equations with the general form;

$$A \cdot u = 0, \quad (1.8)$$

where A is matrix representing the linearised MHD equation set and $u = (p_1, \rho_1, \mathbf{v}_1, \mathbf{B}_1)$ and the index 1 denotes that they are the perturbed quantities. The condition for the existence of a nontrivial solution to this set of algebraic equations is

$$\det|A| = 0. \quad (1.9)$$

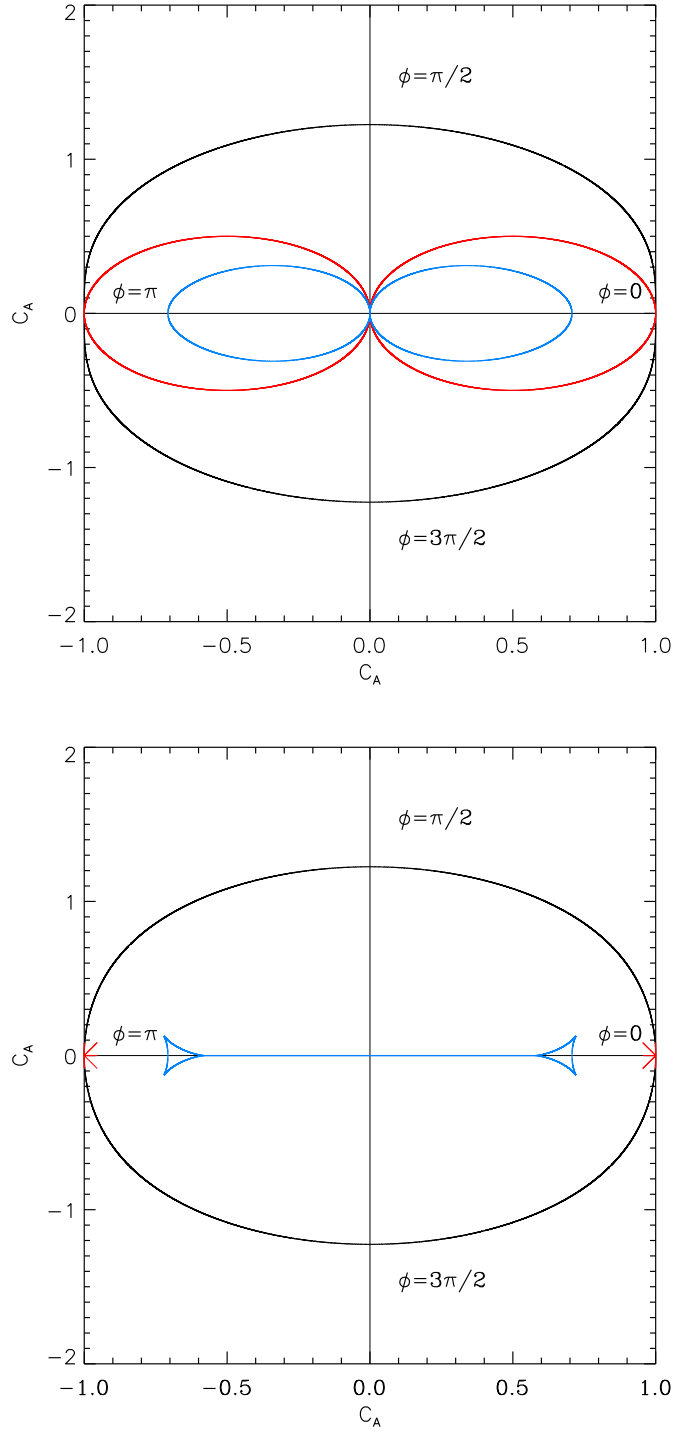


Figure 1.11: Top: phase speeds for the three MHD wave modes in a uniform plasma for the case $C_A > C_S$, with ϕ being the angle between the direction of propagation and the magnetic field and the x and y axis being the wave velocities as a fraction of the Alfvén speed (C_A). The fast speed is plotted in black, the Alfvén speed is plotted in red, and the slow speed is in blue. Bottom: as above but with the group speeds plotted.

This condition can be written in the following way. Firstly, the solution which corresponds to the dispersion relation of fast and slow magnetoacoustic waves;

$$(\omega^2 - C_A^2 k^2 \cos^2 \alpha)(\omega^2 - C_S^2 k^2) - C_A^2 \omega^2 k^2 \sin^2 \alpha = 0, \quad (1.10)$$

where the Alfvén speed (C_A) is given by

$$C_A = \frac{B_0}{\sqrt{\mu_0 \rho}}, \quad (1.11)$$

and the sound speed (C_S) is given by

$$C_S = \sqrt{\gamma p / \rho}. \quad (1.12)$$

and α the angle between the wave vector (i.e the direction of propagation) and equilibrium field. The fast speed is a combination of these two speeds, $C_F = \sqrt{C_A^2 + C_S^2}$. The second solution is the dispersion relation for Alfvén waves;

$$\omega^2 - C_A^2 k^2 \cos^2 \alpha = 0. \quad (1.13)$$

For Alfvén waves the following can be written;

$$\omega = C_A k \cos \alpha, \quad (1.14)$$

$$v_A = \omega / k = C_A \cos \alpha, \quad (1.15)$$

$$\mathbf{v}_g = \nabla_{\mathbf{k}} \omega = v_A \mathbf{B}. \quad (1.16)$$

Here v_A is the phase speed and v_g is the group speed. Important Alfvén wave properties to note are their incompressible nature (no change of p , $|\mathbf{B}^2|$ or ρ), and their group speed is directed along the direction of B . Therefore they cannot transfer information across field lines. Fast and slow magnetoacoustic waves are compressive and can propagate energy in all directions between them. The phase (upper panel) and group (lower panel) speeds for these waves (for the case $C_A > C_S$) are plotted on the same axis to summarise this information (see Fig. 1.11).

1.3.2 MHD waves in structured plasma

MHD wave theory in structured plasma, such as the corona, was developed in the 1970's and 80's [Zajtsev & Stepanov, 1975; Roberts, 1981a,b; Edwin & Roberts, 1983]. A variety of wave modes and oscillations were predicted, many of them listed in Section 1.2.

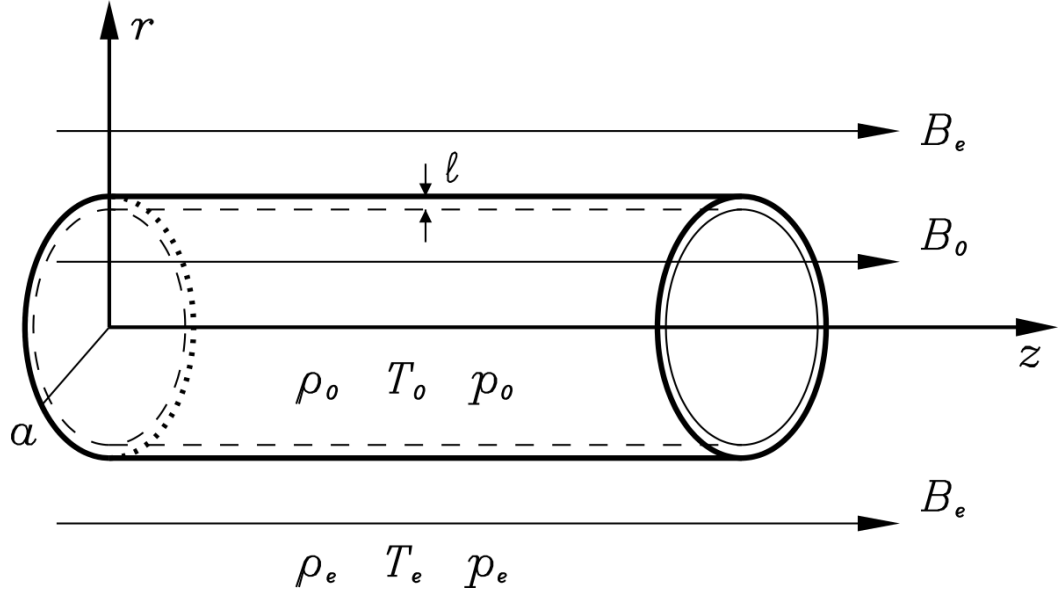


Figure 1.12: The straight magnetic cylinder model, with the addition of a finite layer (of width l) where the density varies linearly between the internal and external values [Nakariakov & Verwichte, 2005].

Four important characteristic speeds defined from the MHD description of plasma are the sound speed (C_S), the Alfvén speed (C_A), the fast speed (C_F) and the tube speed (C_T), given by $C_T = C_S C_A / (C_A^2 + C_S^2)^{1/2}$.

A frequently used model which has been applied to solar physics problems for decades is the MHD modes of a straight plasma cylinder. A straight cylinder of homogeneous plasma is considered, with a uniform density ρ_0 , pressure p_0 and magnetic field $B_0 \mathbf{e}_z$ along the axis of the cylinder. The plasma in which the cylinder is embedded is also homogeneous, with a uniform density ρ_e , pressure p_e and magnetic field $B_e \mathbf{e}_z$ in the same plane as the internal magnetic field. A sketch of this configuration is shown in Fig. 1.12.

For this system to be in equilibrium there must be a balance of the total pressure (p_{tot}) inside and outside the loop, which is the sum of the magnetic and gas pressure. From this it follows that;

$$p_0 + \frac{B_0^2}{2\mu_0} = p_e + \frac{B_e^2}{2\mu_0}. \quad (1.17)$$

C_{Se} , C_{Ae} , C_{Te} are the characteristic speeds in the external medium and C_{Si} , C_{Ai} , C_{Ti} are the corresponding speeds inside the plasma cylinder. Since a characteristic spacial scale has been introduced via the radius R , waves within the cylinder undergo dispersion. The dispersion relation can be derived by considering linear

perturbations to the equilibrium, such as;

$$p_1 = \delta p_{tot}(r)e^{i(k_z z + m\phi - \omega t)}, \quad (1.18)$$

where k_z is the wave number along the axis of the cylinder and m is the azimuthal wave number.

The following set of ordinary differential equations describe the behaviour of the plasma cylinder when the above linear perturbation is applied, for a full derivation see [Sakurai et al. \[1991\]](#).

$$D \frac{d}{dr}(r\xi_r) = (C_A^2 + C_S^2)(\omega^2 - C_T^2 k_z^2)(\kappa^2 + \frac{m^2}{r^2})r\delta p_{tot}. \quad (1.19)$$

$$\frac{d\delta p_{tot}}{dr} = \rho_0(\omega^2 - C_A^2 k_z^2)\xi_r. \quad (1.20)$$

$$\rho_0(\omega^2 - C_A^2 k_z^2)\xi_\phi = -\frac{im}{r}\delta p_{tot}. \quad (1.21)$$

The symbols take their previous meaning. ξ_r and ξ_ϕ are the displacements in the radial and azimuthal directions. D is given by

$$D = \rho_0(C_A^2 + C_S^2)(\omega^2 - C_A^2 k_z^2)(\omega^2 - C_T^2 k_z^2), \quad (1.22)$$

and κ is the transverse wave number defined as

$$\kappa^2(\omega) = -\frac{(\omega^2 - C_S^2 k_z^2)(\omega^2 - C_A^2 k_z^2)}{(C_A^2 + C_S^2)(\omega^2 - C_T^2 k_z^2)}. \quad (1.23)$$

Reducing this set of equations in the external and internal medium and solving the resulting equations gives us the classic dispersion relation for magnetoacoustic waves in the plasma cylinder [[Edwin & Roberts, 1983](#); [Nakariakov & Verwichte, 2005](#)]

$$\rho_e(\omega^2 - k_z^2 C_{Ae}^2)k_0 \frac{I'_m(\kappa_0 a)}{I_m(\kappa_0 a)} + \rho_0(k_z^2 C_{A0}^2 - \omega^2)\kappa_e \frac{K'_m(\kappa_e a)}{K_m(\kappa_e a)} = 0, \quad (1.24)$$

where $I_m(x)$ and $K_m(x)$ are modified Bessel functions of order m , and the prime denotes their derivatives with respect to x . κ_e and κ_0 are the transverse wave numbers in the external and internal plasma. The solutions to this dispersion relation for coronal parameters are plotted in Fig. 1.13. m is an integer which corresponds to the azimuthal structure of the wave modes, sausage modes are waves with $m = 0$, and kink modes are waves with $|m| = 1$. Body waves (which require $\kappa_e^2 > 0$) have oscillatory behaviour within the plasma cylinder and evanescent behaviour outside, whereas surface wave modes have evanescent behaviour in both cases (if both

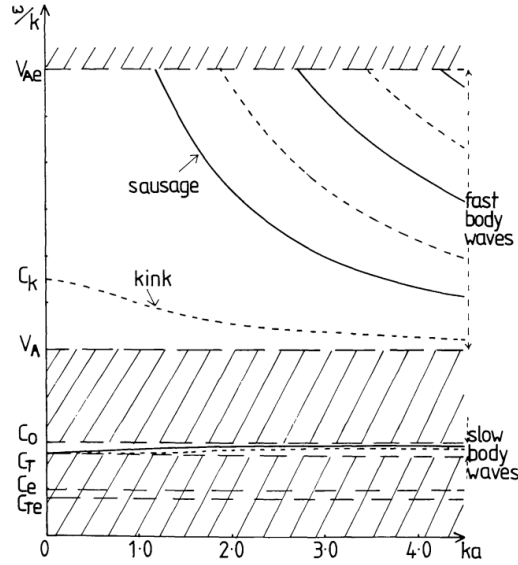


Figure 1.13: The Dispersion relations of MHD modes in structured coronal plasma. The hashed regions are where modes with real frequency and wavenumber are excluded. The dashed horizontal lines denote the wave speeds indicated on the axis. The solid and dashed curves are the dispersion relations of the modes indicated, with azimuthal wavenumbers 0 and 1 respectively [Edwin & Roberts, 1983].

the external and internal plasmas are of low β). The wave modes are traditionally split into two categories, fast (between C_{A0} and C_{Ae}) and slow (between C_{T0} and C_{Ae}). The fast modes are strongly dispersive, highlighted by their departure from a horizontal line in the dispersion plots (see Fig. 1.13).

If the long wavelength limit is taken then the phase speed of all modes apart from the fast sausage modes tends to the kink speed,

$$C_k = \left(\frac{B_0^2/\mu_0 + B_e^2/\mu_0}{\rho_0 + \rho_e} \right)^{1/2} = \left(\frac{\rho_0 C_{A0}^2 + \rho_e C_{Ae}^2}{\rho_0 + \rho_e} \right)^{1/2}. \quad (1.25)$$

The sausage mode approaches its cut-off frequency at the external Alfvén speed, waves with lower wavenumbers (i.e lower frequencies) are not trapped within the structure. This is illustrated in the dispersion plot in Fig. 1.13.

1.4 Kink oscillations of coronal loops

Kink (or transverse) oscillations of coronal loops have been intensively studied since their detection with TRACE just before the turn of the Millennium [Aschwanden et al., 1999; Nakariakov et al., 1999]. Prior to their detection they were the subject of a range of theoretical and numerical studies [e.g. Zaitsev & Stepanov, 1982; Edwin & Roberts, 1983; Roberts et al., 1984; Murawski & Roberts, 1994]. Their study is compelling due to the many poorly understood aspects of coronal loops, some of

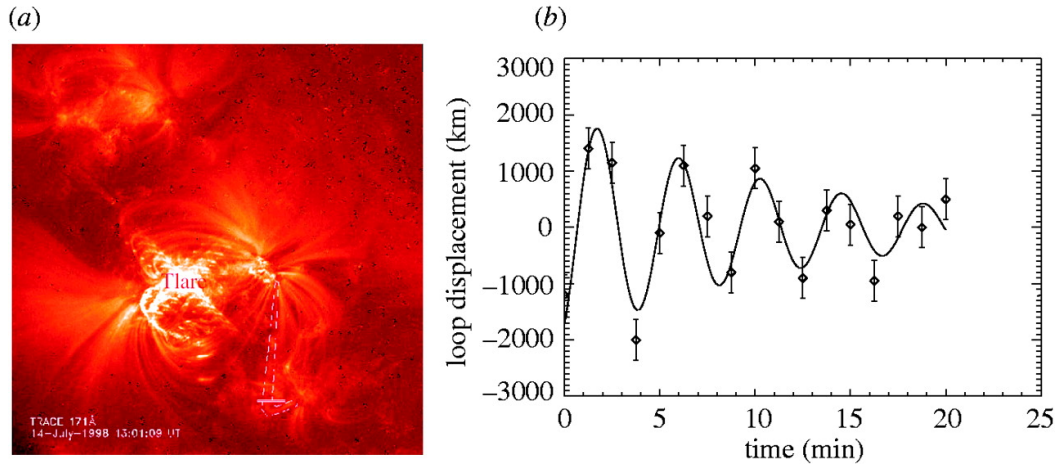


Figure 1.14: An example of a kink oscillation of a coronal loop observed with TRACE. On the left is the active region showing the flare and the loop which becomes perturbed and on the right is the time series of the oscillation, approximated by an exponentially damped [Nakariakov et al., 1999].

which were discussed in Section 1.1.4.

Standing global modes induced by flaring activity are the most commonly detected form of kink oscillation [e.g. Nakariakov et al., 1999; Schrijver et al., 2002; White & Verwichte, 2012]. For a standing mode with wavelength λ in a coronal loop of length L ;

$$C_k = \lambda/P, \quad (1.26)$$

with $\lambda = 2L$ for the fundamental standing mode. This should also be equal to this expression for the kink speed given in Eqn. 1.25.

This phenomenon is clearly observed with the spatial and temporal resolution of recent EUV imagers, such as TRACE, and the Atmospheric Imaging Assembly (AIA) onboard the Solar Dynamics Observatory (SDO) [Lemen et al., 2012]. An example observation with TRACE is shown in Fig. 1.14, and an example observation with AIA is shown in Fig. 1.15. Other types of detections have included higher spatial harmonics in coronal loops [e.g. Verwichte et al., 2005; De Moortel & Brady, 2007; Van Doorselaere et al., 2007], their propagating form [Tomczyk et al., 2007], oscillations of polar plumes [Thurgood et al., 2014], and kink waves in coronal jets [Vasheghani Farahani et al., 2009].

Observations of coronal loops and their oscillations have improved in the years since the launch of SDO, as discussed in Section 1.1.4. Cross-sectional structure and intensity oscillations were found in an oscillating coronal loop analysed in detail [Aschwanden & Schrijver, 2011]. Several oscillations observed with AIA were analysed in White & Verwichte [2012]. More recent studies include; White et al. [2013]; Russell et al. [2015]; Sarkar et al. [2016].

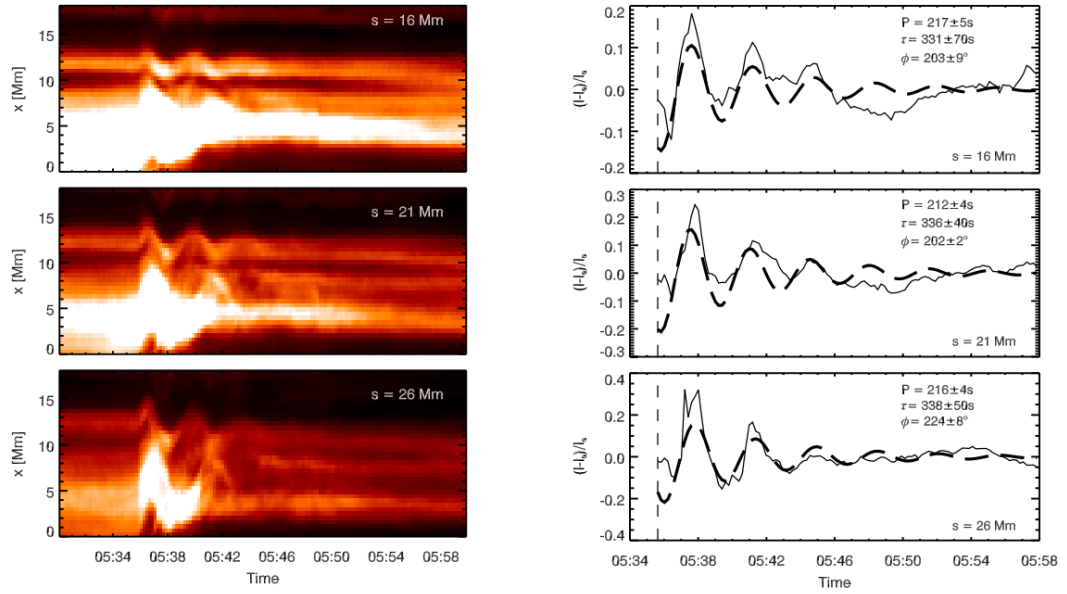


Figure 1.15: An example of a kink oscillation of a coronal loop observed with AIA. On the left are 3 Time-Distance (TD) maps showing the kink oscillation at three different positions along the loop, and the right are the corresponding time series and fits [White & Verwichte, 2012].

A decayless regime of these oscillations was detected before and after a large amplitude decaying kink oscillation [Nisticò et al., 2013]. Recently a statistical study of these oscillations found that they are present in the majority of the active regions analysed [Anfinogentov et al., 2015b]. This results in the opportunity to use these oscillations to perform seismology at any time, in contrast to the flare triggered decaying oscillations. It was also noted that the period of the oscillations scales with the estimated length of the loop, indicating that they are the fundamental standing kink mode. The existence of these ubiquitous low amplitude oscillations heightens the need to understand coronal loops and extract as much information as possible from the oscillations they exhibit.

There are several proposed mechanisms for the initiation of the large amplitude decaying kink oscillations, including via a blast wave from the flare epicentre, restructuring of the active region after the flare and CME or through direct mechanical displacement by the erupting plasma. In Zimovets & Nakariakov [2015] 58 eruptive events, including 169 individual kink oscillations, were catalogued and analysed. It was found that the dominant mechanism for the perturbation was a direct perturbation from a CME or Low Coronal Eruption (LCE).

1.4.1 Damping

In [Nakariakov et al. \[1999\]](#) the rapid damping of the observed kink oscillation was noted. The damping mechanism considered was dissipative and resistive damping, meaning that coronal dissipation coefficients were noted to be eight or nine orders of magnitude higher than the theoretically predicted values. The numerically determined scaling law for damping via dissipative and resistive effects is [see [Ofman et al., 1994a](#)]

$$\frac{\tau}{P} = 16.3 R_e^{0.22}, \quad (1.27)$$

where τ is the damping time, P is the period and R_e is the Reynolds number. This is given by $R_e = LC_{A0}/\nu$, where ν is the shear viscosity and L is the relevant length scale. Several observational studies noted that this cannot account for the rapid damping observed without unrealistic dissipative parameters, as mentioned above.

The observed rapid decay of kink oscillations has now been explained in terms of linear coupling of the collective kink (fast magnetoacoustic) mode to torsional (shear) Alfvén waves in a narrow resonant layer, where the phase speed of the kink wave matches the local Alfvén speed [e.g. [Ruderman & Roberts, 2002](#); [Goossens et al., 2002](#)]. This is known as resonant absorption or mode coupling, and occurs due to the wave guide having an inhomogeneous transverse structure, which causes C_A to vary, and match the kink speed in a certain location. Strong gradients in density, and therefore in the value of C_A , cause this process to occur more efficiently, resulting in faster damping. The resulting Alfvén waves in the inhomogeneous layer are expected to decay via phase mixing, which is discussed below.

A convenient description of resonant absorption in coronal loops can be formed by assuming the loop has a core of uniform density surrounded by an inhomogeneous layer where the density varies linearly between the external and internal values (see Fig. 1.12). This model (Model L) is defined as;

$$\rho(r) = \begin{cases} A, & |r| \leq r_1 \\ A \left(1 - \frac{r-r_1}{r_2-r_1}\right), & r_1 < |r| \leq r_2 \\ 0, & |r| > r_2 \end{cases}, \quad (1.28)$$

where $r_1 = R_L (1 - \epsilon/2)$, $r_2 = R_L (1 + \epsilon/2)$, and $\epsilon = l/R$ is the transition layer width l normalised to the minor radius R_L and defined to be in the range $\epsilon \in [0, 2]$.

For the fundamental kink mode in a plasma cylinder with this transverse density profile the damping is exponential, and the scaling law for this damping via

resonant absorption is given by [see [Ruderman & Roberts, 2002](#)]

$$\frac{\tau}{P} = \frac{2}{\pi\epsilon} \left(\frac{\rho_0 + \rho_e}{\rho_0 - \rho_e} \right), \quad (1.29)$$

where τ is the exponential damping time, and the other symbols have their previous meanings.

This mechanism has been shown to produce damping profiles and rates consistent with observational results [e.g. [Aschwanden et al., 2003](#); [Verth et al., 2010](#)]. In [Aschwanden et al. \[2003\]](#) it was found that a transverse density profile with an inhomogeneous layer was consistent with the observed transverse intensity profile of the loops. The damping times measured were consistent with damping via resonant absorption when the estimated density contrast was taken into account.

Phase mixing is a mechanism for dissipating wave energy in inhomogeneous media through a process which can be thought of as friction between nearby magnetic field lines. The scaling law for damping of the standing kink mode via phase mixing can be given by

$$\frac{\tau}{P} = \left(\frac{3}{4\pi^2} \right)^{1/3} \left(\frac{l}{L} \right)^{2/3} R_e^{1/3}, \quad (1.30)$$

where the quantities are as described previously. This relation can be approximated as $\tau \sim P^{4/3}$ for coronal loops [[Ofman & Aschwanden, 2002](#)].

Due to the success of resonant absorption in describing the damping of kink oscillations phase mixing is now explored as the mechanism by which the torsional Alfvén waves generated are dissipated. The deposition of the energy from the kink mode is therefore determined by the phase mixing timescale and length scale. Alfvén wave phase mixing was first described in [Heyvaerts & Priest \[1983\]](#). In the context of Alfvén waves in the magnetosphere of the Earth, the time dependence of the phase mixing length was found to be [[Mann et al., 1995b](#)]

$$L_{ph} = \frac{2\pi}{\omega'_A t}, \quad (1.31)$$

where $\omega'_A \approx k_{||} v'_A$ and for the transverse loop density Model L $v'_A = (C_{Ae} - C_{A0})/l$. This approximation was found to closely describe numerical results of Alfvén waves generated by resonant absorption of kink waves propagating along coronal loops [[Pascoe et al., 2010](#)].

[Mann & Wright \[1995\]](#) estimated the lifetime of Alfvén waves in the Earth’s magnetosphere as $\tau_A = k_a/\omega'_A$, where k_a is the azimuthal wavenumber. For kink modes $k_a = 1/R$, where R is the minor radius of the loop, and the Alfvén waves generated via resonant absorption retain this symmetry. In terms of the parameters

used in the study of kink oscillations τ_A can be written as

$$\tau_A = \frac{\epsilon L}{\pi (C_{Ae} - C_{A0})}, \quad (1.32)$$

where the parameters have their previous meanings. This shows how the time scale of the Alfvén wave damping depends on the loop parameters, and could result in different post oscillation heating rates for different loops.

Additional damping mechanisms which have been considered include wave leakage to the external medium [Brady & Arber, 2005] and additional damping via cooling of the loop [Morton & Erdélyi, 2009b].

There have been several attempts to match the observed scaling of the damping time and period with the scaling predicted by numerical and analytical studies of the potential damping mechanisms. This was attempted with TRACE data in Ofman & Aschwanden [2002]. These results, along with several more, were collated in Nakariakov et al. [2005] and this has since been continued using AIA data and COMP observations of propagating waves in Verwichte et al. [2013b]. These studies generally find that it is not possible to distinguish between different damping mechanisms from the scaling law alone, but that constraints can be put on parameters such as the density contrast and inhomogeneous layer width if a particular damping mechanism is used. An example is shown in Fig. 1.16.

1.4.2 Generalised damping

More recently, a general spatial damping profile for resonant absorption which describes the damping envelope of propagating kink waves was proposed and its seismological application was explored [Pascoe et al., 2013a]. The work was based on the full analytical solution derived in Hood et al. [2013]. The spatial damping profile proposed consists of two approximations of the full analytical solution, a Gaussian profile for early times, with damping length scale L_g , and an exponential profile for later times, with damping length scale L_d . This extra observable has the potential to make the seismological inversion based on this theory well posed. The damping profile is given by

$$A(z) = \begin{cases} A_0 \exp\left(-\frac{z^2}{2L_g^2}\right) & z \leq h \\ A_h \exp\left(-\frac{z-h}{L_d}\right) & z > h \end{cases}, \quad (1.33)$$

where $A_h = A(z = h)$, the height/distance of the switch in profiles is given by the damping lengths

$$h = L_g^2/L_d. \quad (1.34)$$

This can be extended to standing kink oscillations of coronal loops. The

change of variable $t = z/C_k$ can be used, which corresponds to the long wavelength limit for which the kink mode phase speed is the kink speed C_k , as given in Eqn. 1.26. The damping time and length scales can be related to the coronal loop transverse density profile via

$$\frac{\tau_g}{P} = \frac{L_g}{\lambda} = \frac{2}{\pi\kappa\epsilon^{1/2}}, \quad (1.35)$$

and

$$\frac{\tau_d}{P} = \frac{L_d}{\lambda} = \frac{4}{\pi^2\epsilon\kappa}, \quad (1.36)$$

where τ_g is the Gaussian damping time, τ_d is the exponential damping time, $\epsilon = l/R$ is the normalised inhomogeneous layer width and $\kappa = (\rho_0 - \rho_e)/(\rho_0 + \rho_e)$ is a ratio of the internal density ρ_0 and the external density ρ_e . The two relationships depend on the chosen density profile in the inhomogeneous layer. Here it is given for Model L, defined in Eqn. 1.28. The constant of proportionality is known for the exponential damping profile for other density profiles [see [Goossens et al., 2002](#); [Roberts, 2008](#)]. However, for the damping profile with the transition from a Gaussian regime to an exponential regime only model L has a known solution.

The damping profile for standing kink waves can now be given by

$$A(t) = \begin{cases} A_0 \exp\left(-\frac{t^2}{2\tau_g^2}\right) & t \leq t_s \\ A_s \exp\left(-\frac{t-t_s}{\tau_d}\right) & t > t_s \end{cases}, \quad (1.37)$$

where $A_s = A(t = t_s)$ and the switch in profiles occurs at a time t_s , given by

$$t_s = h/C_k = \tau_g^2/\tau_d. \quad (1.38)$$

1.4.3 Seismology

The principles behind MHD seismology of the solar corona were outlined in Section 1.2, and now the specific application of kink oscillations of coronal loops will be considered. The phase speed is equal to the kink speed, C_k , which is given by

$$C_k \approx \left(\frac{2}{1 + \rho_e/\rho_0}\right)^{1/2} C_{A0}. \quad (1.39)$$

From this the Alfvén speed can be given by

$$C_{A0} = C_k \sqrt{\left(\frac{1 + \rho_e/\rho_0}{2}\right)}. \quad (1.40)$$

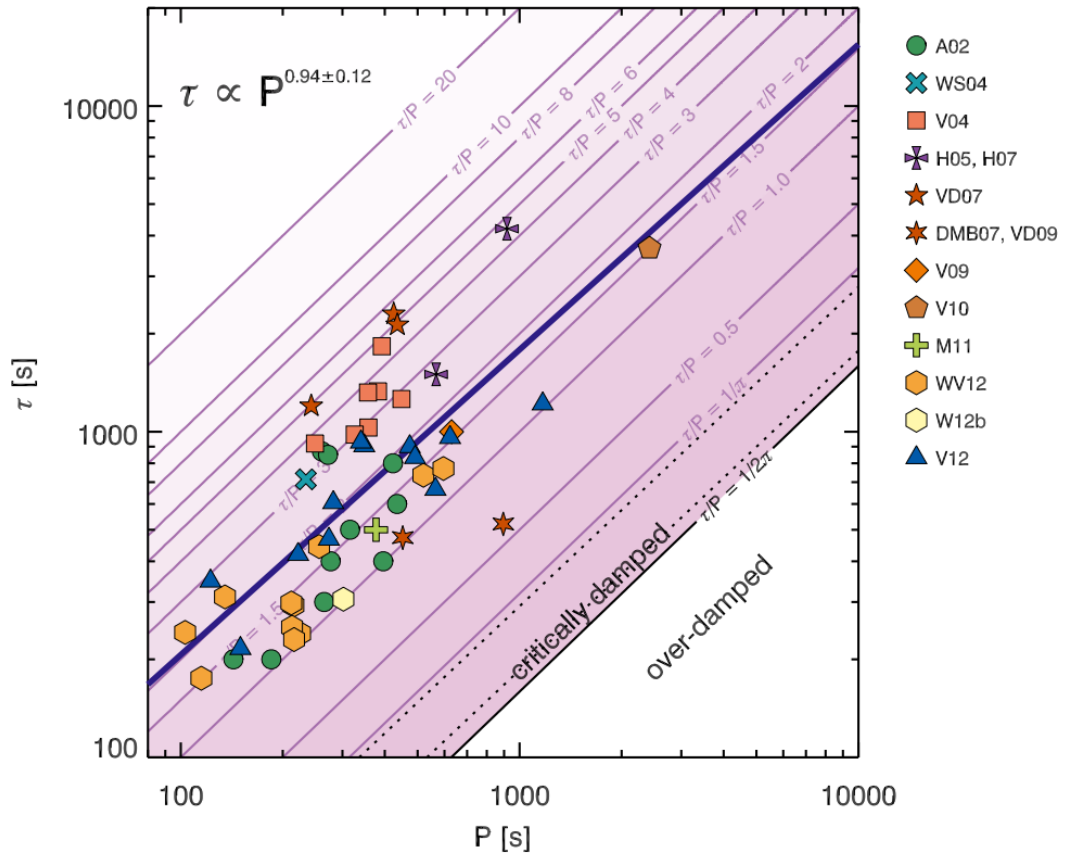


Figure 1.16: Scaling of the exponential damping time of kink oscillations with the oscillation period [Verwichte et al., 2013b]

This means the magnetic field can be estimated as

$$B_0 = C_{A0}\sqrt{\mu_0\rho_0} \approx \frac{\sqrt{2\mu_0 L}}{P}\sqrt{\rho_0(1 + \rho_e/\rho_0)}. \quad (1.41)$$

Thus the magnetic field in an oscillating loop can be estimated by simply recording the period of the oscillation and the length of the loop. In addition an estimate of the density contrast and absolute value of one of the densities must be made. This approximation was first applied to observations in [Nakariakov & Ofman \[2001\]](#), yielding an estimate of the magnetic field in the loop of 13 ± 9 G. Similar estimates were made by [Aschwanden et al. \[2002\]](#) and [Verwichte et al. \[2004\]](#), finding field strengths ranging from 3-90 G and 9-46 G respectively.

A new series of studies took place after the launch of SDO/AIA, due to its advanced time resolution and sensitivity. A single loop oscillation was studied by [Aschwanden & Schrijver \[2011\]](#), who compared the seismologically determined magnetic field strength in the oscillating loop of 4 ± 0.7 G to the value obtained from magnetic field extrapolation, 11 G. In [Verwichte et al. \[2013a\]](#) a detailed comparison of field strengths from seismology and from magnetic field extrapolations was performed. It found that the extrapolated values averaged along the loop are systematically higher. The differential emission measure (DEM) technique was used to obtain values for the density, meaning that the use of guessed values was avoided. The inhomogeneous layer width, ϵ , was calculated, but covered most of the possible values due to the large uncertainties. Statistical seismology was explored in [Verwichte et al. \[2013b\]](#), which was discussed above in context of the damping mechanisms considered. By considering a large sample of kink oscillations with measured damping times and periods, constraints were put on physical loop parameters based on the distribution of the quality factors of the oscillations, i.e the ratio of the damping time to the period.

There has also been a growing interest in the use of seismological inversion techniques. These have most commonly been applied to kink oscillations assumed to damp via resonant absorption. The full analytical description is used to produce inversion curves for each parameter to be determined based on the observed characteristics of the oscillations. This technique was explored in [Goossens et al. \[2008\]](#) under the thin tube and thin boundary approximations. The inversion was applied to several kink oscillations observed with TRACE. For one loop the inversion curves were plotted for the internal Alfvén travel time (τ_A), the density contrast (ζ) and the inhomogeneous layer width (l/R), which are plotted in Fig. 1.17.

The recently proposed generalised damping profile with a switch from a Gaussian to exponential damping regime was discussed in Section. 1.4.2. The extra seismological information made available by this damping profile comes from the link

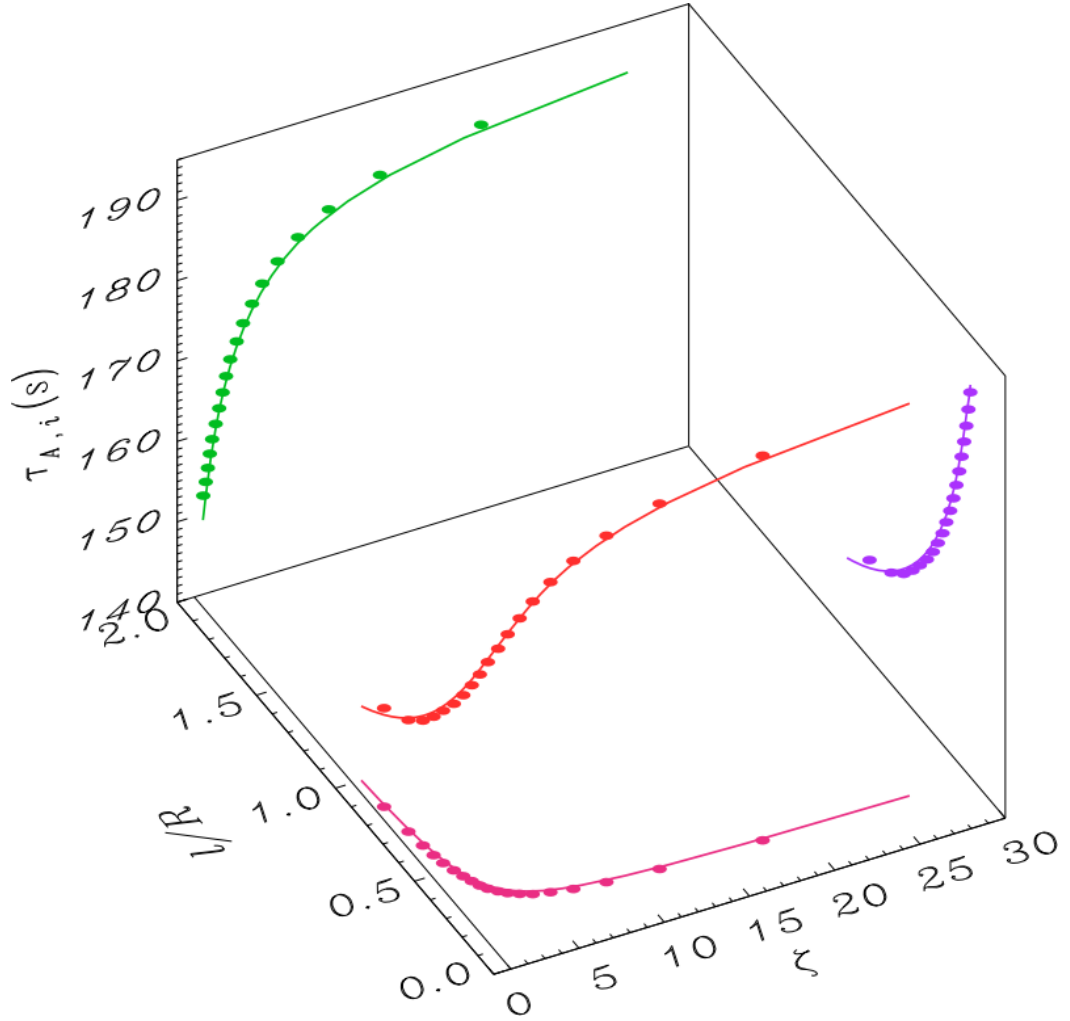


Figure 1.17: Analytic and numerical inversion curves for three coronal loop parameters; the internal Alfvén travel time (τ_A), the density contrast (ζ) and the inhomogeneous layer width (l/R) [Goossens et al., 2008].

between t_s and ρ_0/ρ_e . They can be related in terms of N_c , the number of cycles of oscillation before the switch occurs

$$N_c = \frac{t_s}{P} = \frac{h}{\lambda} = \frac{1}{\kappa} = \frac{\rho_0 + \rho_e}{\rho_0 - \rho_e} = \frac{\rho_0/\rho_e + 1}{\rho_0/\rho_e - 1}. \quad (1.42)$$

Therefore loops with larger density contrasts are expected to transition from the Gaussian to the exponential profile sooner than loops with smaller density contrasts. This forms the basis of the seismological method for determining κ for an observed oscillation. The value of ϵ can then be calculated from the relation in Eq. (1.35) or (1.36). This extra parameter allows the inversion to give us singular values for the transverse structuring parameters of the loop rather than dependencies between them.

The seismological inversion may be calculated with the following set of equations;

$$\tau_d = \tau_g^2/t_s, \quad (1.43)$$

$$\kappa = P/t_s, \quad (1.44)$$

$$\rho_0/\rho_e = (1 + \kappa)/(1 - \kappa), \quad (1.45)$$

$$\epsilon = 4P/(\tau_d \pi^2 \kappa), \quad (1.46)$$

$$C_k = 2L/P, \quad (1.47)$$

$$C_{A0} = C_k/\sqrt{2/(1 + \rho_e/\rho_0)}, \quad (1.48)$$

$$C_{Ae} = C_{A0}\sqrt{\rho_0/\rho_e}, \quad (1.49)$$

$$B_0 = C_{A0}\sqrt{\mu_0 \bar{\mu} m_p n_0}, \quad (1.50)$$

where $\mu_0 = 4\pi \times 10^{-7}$ H/m, $\bar{\mu} = 1.27$, $m_p = 1.6726 \times 10^{-27}$ kg, $n_0 = n_e \rho_0/\rho_e$ and the other values take their previous meanings. The seismological potential demonstrated above makes the accurate analysis of coronal loop damping profiles extremely important. This would allow the detection of the profile given in equation 1.37 and confirm its applicability to real observational data. This in turn would allow unique seismological inversions to be made, giving a more accurate estimate of the magnetic field and allowing the transverse density structure of the loop to be inferred

for the first time. This was one of the motivations behind the work presented in Chapter 2. It should be noted that using this seismological inversion the absolute value of the density still needs to be estimated via other means.

The detection of different harmonics of the same wave mode in the same coronal loop may allow additional seismological information to be extracted. For standing modes the longitudinal wavenumber k is an integer multiple of π/L i.e. $k_n = n\pi/L$. The fundamental kink mode is denoted by $n = 1$ and the second harmonic is $n = 2$ and so on. In the long wavelength limit, kink waves are weakly dispersive, however non-uniformity of the kink speed along the loop results in the periods of longitudinal harmonics no longer being integer multiples of the fundamental mode; for example $P_1/2P_2$ is varied from unity by several effects. [Andries et al. \[2005\]](#) used the period ratios detected observationally [[Verwichte et al., 2004](#)] to estimate the density scale height. [McEwan et al. \[2006\]](#) performed a similar study, and an analytical expression for the dependence of the period ratio on the density scale height was derived in [McEwan et al. \[2008\]](#). Other effects considered include elliptic curvature of the loop axis [[Morton & Erdélyi, 2009a](#)] and the effect of steady siphon flows [[Chen et al., 2014](#)].

There have been several observations and seismological applications of higher harmonics of kink oscillations of coronal loops [e.g [De Moortel & Brady, 2007](#); [Van Doorselaere et al., 2007](#); [Srivastava et al., 2013](#)]. Recently [Guo et al. \[2015\]](#) analysed AIA data and looked at the anti-node positions of the detected harmonics, which were found to shift towards the region of weak magnetic field. They also used the fundamental kink mode to estimate the magnetic field strength, obtaining $B = 8 \pm 1$ G, and used DEM to estimate the temperature and density. The shift of the anti-node positions indicated that the density stratification and the temperature difference effects on the period ratio are larger than the magnetic field variation effect.

1.4.4 Non-linear effects

The majority of theoretical studies of kink oscillations are performed in the linear regime and in these studies the finite amplitude effects are neglected in the governing MHD equations. In kink oscillations the amplitudes of the perturbations of the magnetic field and density, as well as the speeds of the displacement, are observed to be just a few percent of the equilibrium parameters and the Alfvén speed, respectively, justifying the linear nature of the oscillation.

However, the displacement amplitude is often similar to, or greater than, the minor radius of the loop, suggesting that the assumption of the linearity of the observed kink oscillations might not be fully applicable to all oscillating loops. Non-linearity may modify the efficiency of the damping mechanisms or introduce

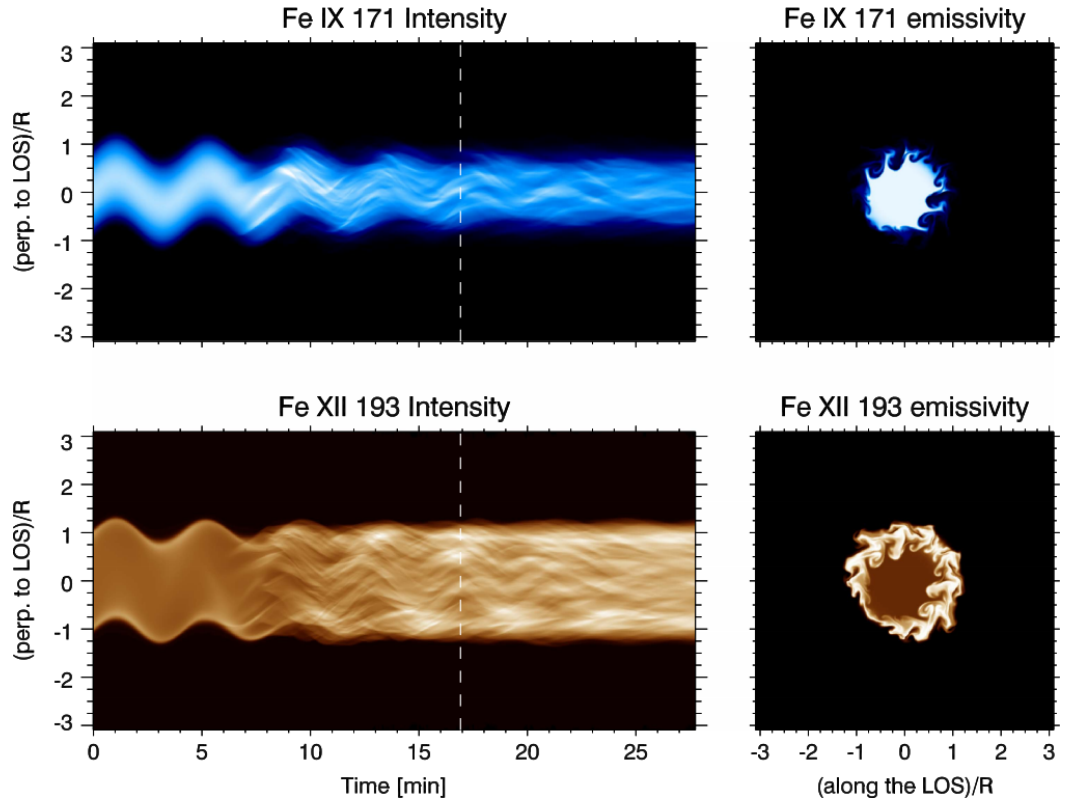


Figure 1.18: Left: time-distance maps forward modelled to EUV emission from numerical simulations of the KHI instability in oscillating coronal loops. Right: The same simulations, shown as a cross section of the emissivity depicting how the loop cross-section is perturbed during the oscillation [[Antolin et al., 2016](#)].

additional sources of damping or dissipation. With the lack of direct observational evidence of non-linear effects in the kink mode dynamics, the theory of non-linear kink oscillations has only been addressed in several dedicated studies. The shear Alfvén waves produced after the damping of kink modes via resonant absorption may become large amplitude due to their very narrow localisation at the resonant shell inside the oscillating loop and their inability to spread across the field. However, consideration of the time-dependent evolution of this process has shown that the shear Alfvén waves are not exclusively confined to the hypothetical narrow resonant layer, but spread along the whole non-uniform layer because of phase mixing, gradually lowering their resulting amplitude [e.g. [Soler & Terradas, 2015](#)].

Several theoretical studies have generalised the effect of resonant absorption in the non-linear regime. For example, large amplitude kink waves can induce field-aligned plasma flows and density perturbations by the ponderomotive force, which is similar to the well-known non-linear effect in linearly or elliptically polarised Alfvén waves [see [Vasheghani Farahani et al., 2012](#), for a recent discussion]. For example, [Terradas & Ofman \[2004\]](#) showed that this effect leads to the accumulation of mass at the loop top. The resulting redistribution of the matter in the oscillating loop would change the location of resonant layers and therefore the efficiency of wave damping. Usually these induced flows are essentially sub-sonic and sub-Alfvénic, as they are proportional to the square of the relative amplitude of the mother kink waves. However, these induced flows are likely to be non-uniform in the transverse direction [e.g. [Clack & Ballai, 2009](#)]. These flows may cause various shear-flow instabilities that enhance the transport coefficients locally and, hence, the damping [e.g. [Ofman & Davila, 1995](#)].

[Ofman et al. \[1994b\]](#) showed that the Kelvin–Helmholtz Instability (KHI) for torsional Alfvén waves, first described by [Browning & Priest \[1984\]](#) in the context of Alfvén phase mixing, can occur at the resonant layer of an oscillating loop resulting in enhanced dissipation. [Terradas et al. \[2008\]](#) performed a high-resolution, three-dimensional numerical study of non-linear kink oscillations and found that shear-flow instabilities develop and deform the boundary of the flux tube, and that the evolution of the tube is very sensitive to the amplitude of the initial perturbation. They relate their results to the development of KHI. It was found that KHI can develop over timescales comparable to the kink oscillation period [[Soler et al., 2010](#)]. Further numerical studies of KHI in oscillating structures in the corona include transverse prominence oscillations [[Antolin et al., 2015](#)] and coronal loops [[Antolin et al., 2016](#)] (Fig. 1.18). Additionally, numerical simulations of [Magyar & Van Doorselaere \[2016b\]](#) suggested that highly multi-threaded, or braided, loops could be unstable to transverse oscillations and that the KHI is also efficiently generated in this case. In all of these examples the transverse structure is perturbed, which

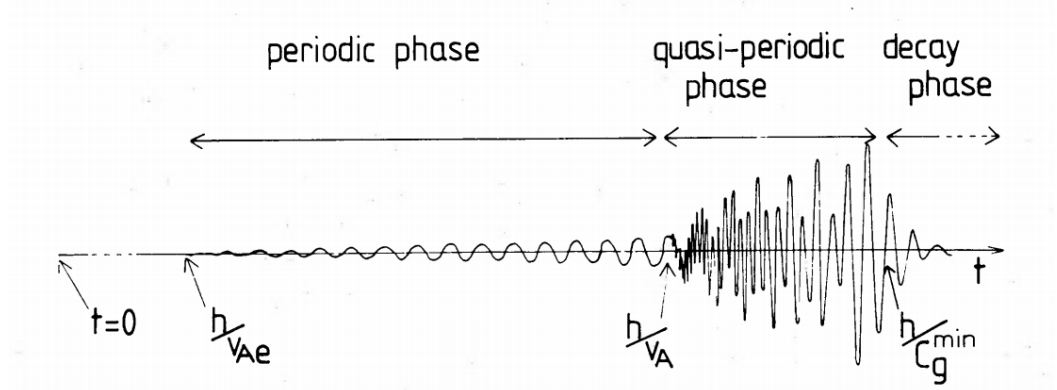


Figure 1.19: The evolution of a fast sausage wave in the low- β limit, showing the three main phases of the evolution [Roberts et al., 1984].

is of theoretical and observational significance in the study of kink oscillations of coronal loops.

1.5 QFP wave trains

Another example of MHD waves in coronal wave guides are Quasi-periodic Fast Propagating wave trains (QFP wave trains). These have recently been imaged with AIA, however they remain poorly understood and their seismological potential has yet to be exploited.

The dispersive evolution of a broadband sausage fast magnetoacoustic wave when propagating in a coronal plasma wave guide was shown to result in a propagating quasi-periodic wave train (see Fig. 1.19 [Roberts et al., 1984]). This phenomenon occurs at a certain distance from the initial perturbation, depending on the width of the wave guide, the fast magnetoacoustic speed and the spatial spectrum of the propagating perturbation. The time signature of the developed wave train can show a characteristic “crazy tadpole” wavelet spectrum, where a narrowband tail precedes a broadband head (see Fig. 1.20 [Nakariakov et al., 2004]). This feature will only occur if the spectrum of the initial perturbation is broad, sitting largely above the cut-off wave number [Nakariakov et al., 2005]. This signature of dispersive evolution was shown to be a robust feature of plane fast magnetoacoustic waveguides with different perpendicular profiles of the plasma density [Yu et al., 2015, 2016] and was found to be consistent with analytical estimations [Oliver et al., 2015]. The wavelet signatures of impulsively-generated fast wave trains formed in cylindrical waveguides appear “head-first” due to the change in geometry [Shestov et al., 2015].

The first detection of this phenomenon came from analysis of the radio emission of flares using the ICARUS spectrometer [Roberts et al., 1983]. This revealed coronal wave trains qualitatively similar to theoretical predictions. An observation

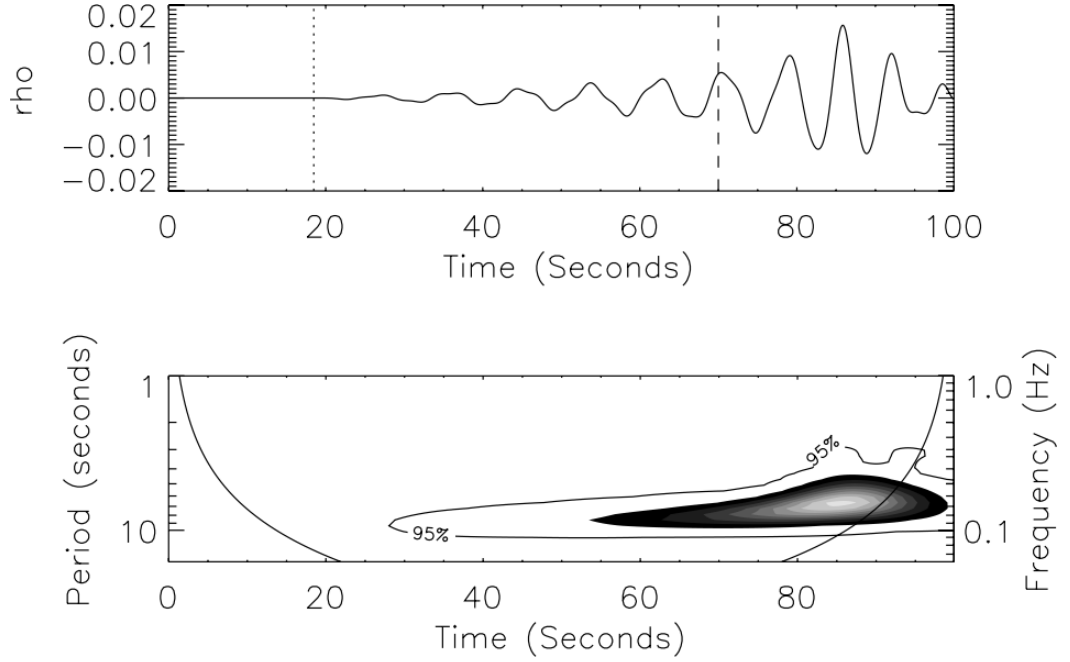


Figure 1.20: Numerical simulation of a dispersively generated fast magnetoacoustic wave train generated from a single impulsive perturbation. In the lower panel is the wavelet spectra of the density time series in the upper panel [Nakariakov et al., 2004].

of fast propagating waves from the Solar Eclipse Coronal Imaging System (SECIS) exhibited a characteristic crazy tadpole wavelet spectrum. This led to its interpretation as a dispersively generated fast propagating wave train guided by a field-aligned non-uniformity of plasma density [Katsiyannis et al., 2003; Cooper et al., 2003].

The high spatial and temporal resolution of the SDO/AIA instrument has recently allowed the detection of QFP wave trains at EUV wavelengths. These wave trains appear to be triggered by a variety of flaring and eruptive events, with differing propagation speeds and periods. Liu et al. [2010, 2011] detected EUV emission disturbances at 171 \AA , propagating from a flaring source along a coronal funnel, with a projected phase speed of 2000 km s^{-1} and a 3 minute period (see Fig. 1.21 and Fig. 1.22). Liu et al. [2012] detected wave trains running ahead of and behind a CME front at 171 and 193 \AA , with a dominant 2 minute period. More recently, Nisticò et al. [2014b] detected and modelled a fast coronal wave train propagating along two different paths, with a speed of $\leq 1000 \text{ km s}^{-1}$ and period of 1 minute. In that study a numerical simulation of fast magnetoacoustic waves undergoing leakage and dispersive evolution in a coronal loop was performed and found to be consistent with the observational results. An overview of these waves and their observation with AIA was given in Liu & Ofman [2014]. Similar signatures are also frequently detected in post-flare radio emission [e.g. Mészárosóvá

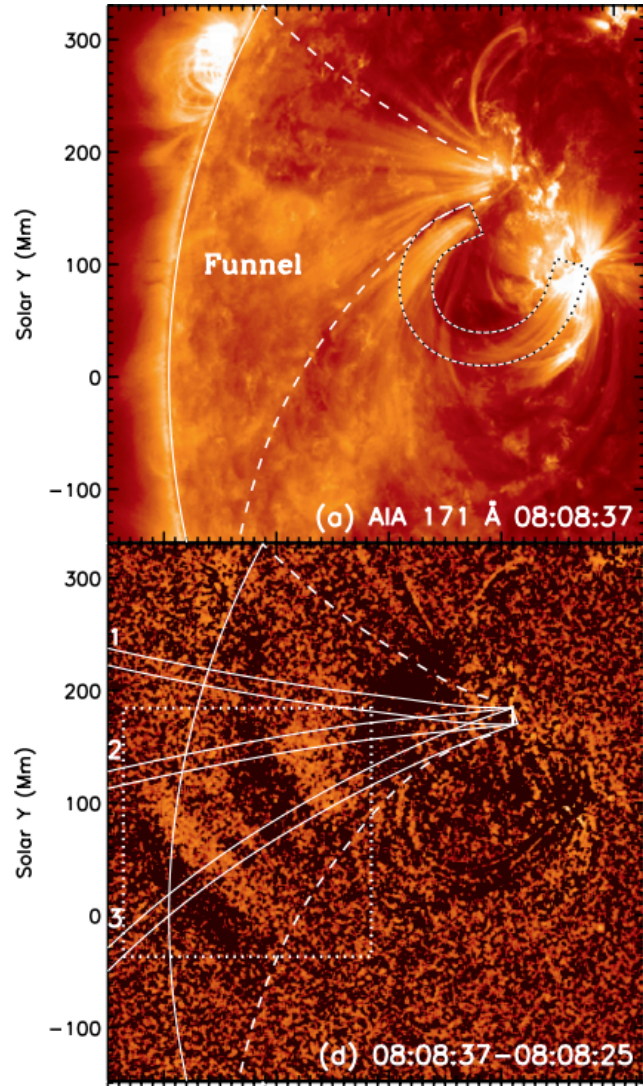


Figure 1.21: Quasi-periodic fast propagating waves in a funnel structure detected with the AIA instrument [Liu et al., 2011].

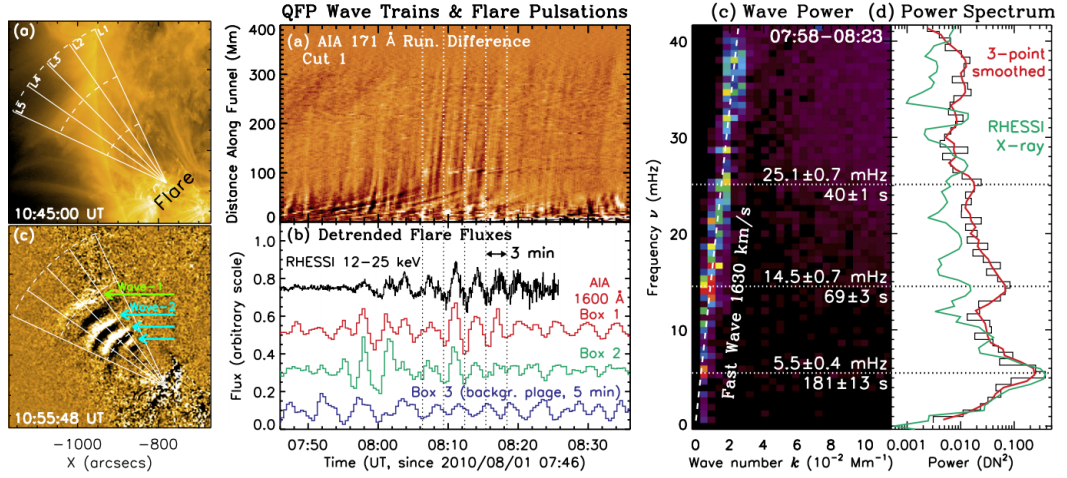


Figure 1.22: Left: Multiple QFP wave trains analysed in [Yuan et al. \[2013\]](#). Middle: A time-distance map showing the wave fronts of the QFP waves. The bottom panel shows flare pulsations detected with RHESSI, which may be related to the detected waves [[Liu et al., 2010](#)]. Right: Fourier power diagram produced from the data to the left, which allowed the wave speed to be measured. Also taken from [Liu et al. \[2010\]](#).

[et al., 2009a, 2016; Karlický et al., 2013](#)], suggesting a common physical cause.

The detected QFP wave trains are generally considered to be a series of quasi-periodic fast magnetoacoustic waves, due to the measured speed and how they appear to be guided by coronal structures. In most EUV imaging detections they appear as a series of arc shaped intensity perturbations, with an amplitude of a few percent, propagating away from flaring active regions. They are often noted to exhibit strong decelerations, explained by the expected reduction of the fast magnetoacoustic speed with distance from the flare epicentre. Normally the waves appear to be propagating upwards into the corona along an open funnel structure, although there are cases where the waves are observed to propagate along closed loop systems. These waves seem to be detected best at 171 Å, which may be due to compressive or thermal properties of the wave, or due to favourable observational conditions with this AIA filter.

Consideration of the driver of these events has led to various interpretations. [Nisticò et al. \[2014b\]](#) considered dispersive evolution as the mechanism for the production of the observed wave train. This is supported by numerical and analytical modelling from [Pascoe et al. \[2013b\]](#), [Pascoe et al. \[2014\]](#) and [Oliver et al. \[2014\]](#), which has produced results consistent with observations, by considering the dispersion and leakage of fast magnetoacoustic waves in funnels, holes and loops, respectively. However, [Liu et al. \[2011\]](#) and [Shen & Liu \[2012\]](#) showed a common periodicity between the quasi-periodic fast propagating wave and the flare quasi-periodic pulsations, suggesting a common origin. [Yuan et al. \[2013\]](#) re-analysed the

second of these events, finding distinct wave trains with start times correlated with radio bursts emitted by non-thermal electrons. This correlation with pulsations in the flaring emission has led to an interpretation of the observed wave trains as the result of repetitive magnetic reconnection associated with the flare, or another mechanism which periodically excites broadband pulses of fast magnetoacoustic waves. Recent modelling results from [Yang et al. \[2015\]](#) have confirmed this as a viable mechanism for the production of a series of fast magnetoacoustic waves with phase speeds and observational signatures which match observations.

As mentioned above, the seismological potential of these waves remains to be fully explored, both theoretically and observationally. If they do indeed propagate at the fast speed, then this may be used to obtain an estimate for the magnetic field if the density is measured or estimated. Additionally, if the quasi-periodicity is generated via dispersion, then it depends on physical properties of the wave guide. As such, the wavelet spectra or time-series may be used to infer some aspects of the physical properties of the wave guides, if dispersive evolution is assumed to take place.

1.6 SDO/AIA

1.6.1 Introduction

The strongest emission from the solar corona is at EUV, soft X-ray, hard X-ray and radio wavelengths. The detailed study of waves and oscillations in the corona requires EUV imaging with sufficient spatial and temporal resolution.

The Transition Region and Coronal Explorer (TRACE, see Fig. 1.6 and [Handy et al. 1999](#)) was a satellite aimed at investigating the dynamics of the magnetised plasma in the transition region and corona with high temporal and spatial resolution. It included four filters which imaged different EUV wavelengths corresponding to different temperatures of plasma. This made it well suited to the detection of waves and oscillations in the corona, described in Section. 1.2. Another EUV instrument was included in the Solar Terrestrial Relations Observatory (STEREO) spacecraft. This mission consists of two spacecraft in orbit around the Sun, giving different line-of-sight images, allowing 3D information about coronal structures to be obtained. The potential applications of this data included inference of the 3D coronal loop geometry [e.g. [Aschwanden et al., 2008](#)]. The Coronal Multi-channel Polarimeter (COMP) began observing in 2009, and was a dedicated low-coronal imager, which detected ubiquitous propagating kink waves in structures low in the corona [[Tomczyk et al., 2008](#)]. However, observations were confined to a narrow spatial region of the corona (i.e not full disc images) and the data required heavy processing to extract the oscillatory signals.

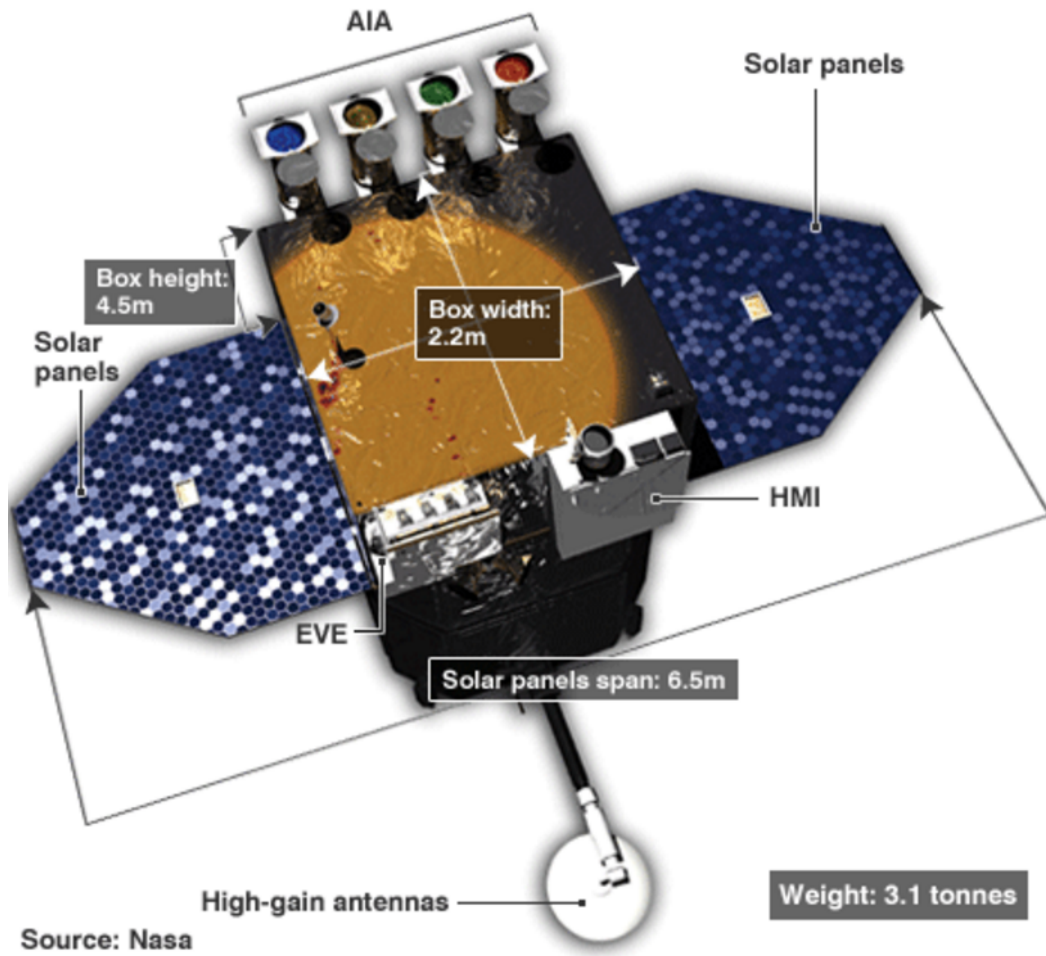


Figure 1.23: The Solar Dynamics Observatory (SDO) with its three instruments labelled. Courtesy of NASA.

The Solar Dynamics Observatory (SDO) was launched in 2010 as part of NASA's 'Living With a Star' program (see Fig. 1.23). Its aim is to investigate the generation and structuring of the Sun's magnetic field, and how this energy is released into the heliosphere as CMEs, the solar wind and energetic particles [Pesnell et al., 2012]. The satellite includes three instruments, the Atmospheric Imaging Assembly (AIA), the Helioseismic and Magnetic Imager (HMI) and the Extreme Ultraviolet Variability Experiment (EVE), shown in Fig. 1.23. AIA, as its name suggests, is dedicated to imaging the Sun's atmosphere.

1.6.2 The AIA instrument

AIA provides continuous, full disc monitoring of the solar corona [Lemen et al., 2012]. It produces images which extend up to 1.5 solar radii with $4k \times 4k$ pixels, at a spatial resolution of 0.6 arcsec/pixel. It also has a cadence of 12 s. The Sun

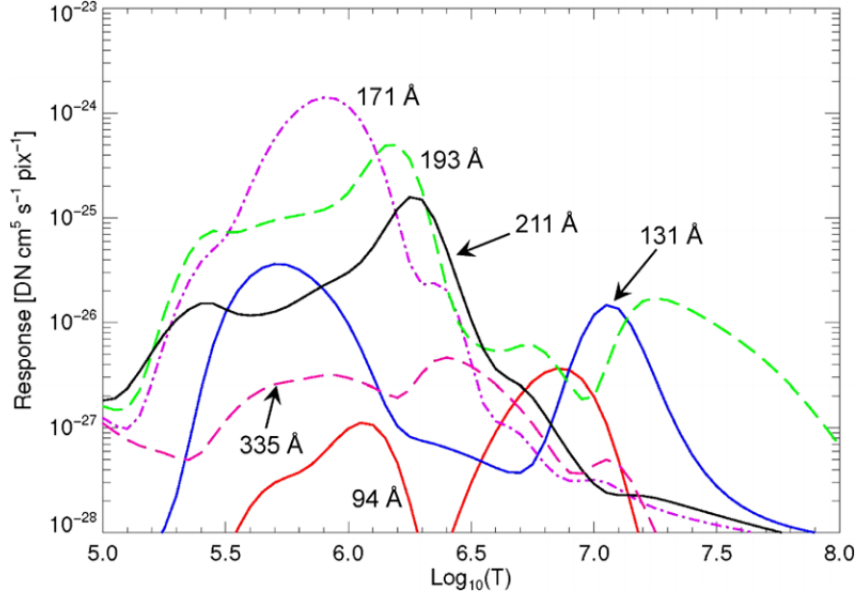


Figure 1.24: Temperature response functions for six EUV channels of AIA [Lemen et al., 2012].

is imaged in 10 different narrow-band channels, seven of which correspond to EUV wavelengths: Fe XVIII (94 Å), Fe VIII, XXI (131 Å), Fe IX (171 Å), Fe XII, XXIV (193 Å), Fe XIV (211 Å), He II (304 Å), FeXVI (335 Å). The temperature of the plasma observed in these EUV bands ranges from about 0.6 MK to about 16 MK. In addition there are two UV channels: C IV line (1,600 Å) and the continuum emission (1,700 Å). These wavelengths correspond to the transition region, upper photosphere and temperature minimum. Finally, a white light channel (4,500 Å) images the visible surface of the Sun.

The response functions of the six main EUV channels of AIA are shown in Fig. 1.24. The different EUV filters mean that the data corresponds to different temperatures of plasma. However, there is overlap between some of the channels and some have peaks at several temperatures, meaning that complex analysis is required to accurately determine the temperature of the plasma being observed. The different channels also have different point spread functions (PSFs) associated with them [Grigis et al., 2013]. The processing and analysis of the EUV imaging data from AIA will be discussed in Section. 1.7.1.

1.7 Data analysis techniques

1.7.1 EUV image analysis

The strength of the electromagnetic emission from the coronal plasma depends on its density and temperature. Plasma of different temperatures contains different

excited states of the constituent ions, resulting in emission at different wavelengths. Different EUV filters relate to different temperatures of plasma, and the response function of a given wavelength varies with temperature. As mentioned above, some EUV filters have multiple peaks in their response functions. Additionally, coronal plasma is optically thin and so multiple structures or waves along the observational Line Of Sight (LOS) appear superposed. All of these effects mean that analysing EUV images of the corona is a complicated process.

A widely used quantity is the Differential Emission Measure (DEM), which measures the amount of plasma along the LOS that contributes to the observed emission within a temperature interval [Aschwanden, 2005];

$$DEM(T) = n_e n_H \frac{dz}{dT}, \quad (1.51)$$

where z is the coordinate along the LOS, n_e is the electron density and n_H is the elemental hydrogen density, often $n_H/n_e \approx 0.83$ is assumed. The intensity at a given wavelength can then be formed as;

$$I(\lambda_i) = \int_0^\infty G(T, \lambda_i, A, n_e) \frac{DEM(T)}{dT} dT, \quad (1.52)$$

where λ_i is the wavelength of interest, G is the instrumental response function and A is the abundance factor which incorporates the parameters related to atomic physics of the plasma.

DEMs can be obtained from inversions of EUV images using multiple wavelengths, providing the temperature response of the different channels and appropriate model DEMs from the different EUV lines are used. From the obtained DEMs temperatures and densities of coronal structures, and their uncertainties, can be obtained, however it is important to note that this is an ill-posed inversion. An example procedure for SDO data is described in Hannah & Kontar [2012]. In this thesis the DEM inversion technique will not be used, however it is important to understand the complex relationship between the observed EUV intensity and the plasma from which it comes. The limitations of any analysis procedure which does not account for any of the effects described above should be considered.

The EUV data sets can be retrieved in the Flexible Image Transport System (FITS) format at full resolution ($4k \times 4k$) from the Joint Science Operations Center (JSOC), with spatial and temporal resolution of 0.6 arcsec and 12 s respectively, using the standard SolarSoftware (SSW) function `vso_search.pro`. The images should then be prepared and corrected using the SSW routine `aia_prep.pro`, including normalisation by the exposure time of the instrument, which can vary during flare emission. A series of images can be obtained for a region of interest within a given time interval by submitting a SSW cut-out request. The data cubes obtained

will have the standard pixel size of 0.6 arcsec, and a temporal cadence of 12 s, or 24 s in some cases when the intermediate image was not returned owing to an insufficiently short exposure time, which should be accounted for in any analysis in the time domain. Time-Distance (TD) maps are a frequently used method of detecting and analysing waves and oscillations in imaging data. One axis corresponds to time, and the other to a one-dimensional distance along the selected slit in the images. They will be frequently used to present data throughout this thesis.

1.7.2 Time series analysis

Time series analysis is an important aspect in most branches of science. It is absolutely critical in fields such as astrophysics, where spatial information is not normally available, so variations in time series must be analysed in great detail to infer any spatial information. In solar physics, despite the often abundant spatial and spectral information the data must often still be reduced to a time series for further analysis, including the proper treatment of uncertainties.

An important aspect of time series analysis is the detrending of the data. This can be done in a number of ways. To highlight waves and oscillations in imaging data the images themselves can be detrended. Previous images may be subtracted from the current image to produce a running difference image, which highlights the changes which have occurred between the two images as positive and negative values. Alternative options include taking the ratio of the image to a previous image. The same ideas can be applied to one dimensional time series, which can include taking the derivative (similar to running difference images), smoothing, or subtracting a fit to the background trend.

One technique to analyse time series is to use least-squares fitting to fit the data with a model which has either empirical or theoretical justification. This procedure involves finding the best fitting curve to the data points by minimising the sum of the squares of the offsets between the data and the fit, i.e the residuals. For vertical least squares fitting this can be expressed as

$$R^2 = \sum [y_i - f(x_i, a_1, a_2, \dots, a_n)]^2, \quad (1.53)$$

where y_i represents the data to be fit, and f the function to be fit, which depends on the independent variable at each point, x_i , and the adjustable vector of parameters, \mathbf{a} . R^2 is then minimised, i.e the condition

$$\frac{\partial(R^2)}{\partial a_i} = 0, \quad (1.54)$$

is enforced. The most commonly used implementation of this procedure is Levenberg-Marquardt least-squares fitting with the data points weighted according to their

errors. There are multiple different functions which use this technique within IDL (Interactive Data Language), such as `mpfit.pro` [Markwardt, 2009], `gaussfit.pro` and `curvefit.pro`.

One of the major branches of time-series analysis is the detection of periodicities. This is due to many physical processes having a built in periodicity, which often depends on physical parameters, such as in coronal seismology. One method is to detrend the time-series, and then fit a periodic function to the data using least-squares fitting. When this is not possible then significant peaks in the frequency domain can be searched for, via a Fourier transform or construction of a periodogram [Scargle, 1982].

If temporal information about a non-stationary periodicity is required, then other spectral analysis techniques are required. The Windowed Fourier Transform (WFT) performs a Fourier transform on discrete portions of a time series, allowing the local spectra to be obtained for different times, allowing the time evolution of periodicities within the signal to be examined. In the time domain it is equivalent to multiplying a signal by a window function that scans the time-series. Similar to a WFT, the wavelet transform allows time-dependent power spectra to be obtained, allowing the evolution of detected periodicities to be analysed. The wavelet transform is defined as the convolution of a time series with a scaled version of a mother function, such as the Morlet function. A commonly applied wavelet analysis software is available online in multiple programming languages, including IDL [see Torrence & Compo, 1998].

1.7.3 Bayesian inference

In solar physics the best-fitting parameters for a particular model of interest are often determined by a Levenberg-Marquardt least-squares fit to the relevant data, with each point weighted according to its error. Now a method based on Bayesian statistics will be discussed. Bayesian analysis allows robust estimation of how the output of the proposed model depends on the input parameters. It can be used to determine information about model parameters from data (inference) and to compare how well different models explain the observed data (model comparison) [see von Toussaint, 2011]. Bayesian inference is well used in many branches of physics, in particular astrophysics. Recently, it has been used to seismologically infer coronal loop parameters from observations of damped kink oscillations, as discussed several times in Section. 1.4 [e.g., Arregui & Asensio Ramos, 2011; Arregui et al., 2013a, 2015; Arregui, 2018]. In particular, Arregui et al. [2013b] used the Gaussian and exponential damping regimes described in Section 1.4.2, and describe an inversion procedure based on Bayesian analysis, conversely Arregui & Asensio Ramos [2014] apply Bayesian analysis to the ill-posed case, where only exponential

damping is considered.

The general methodology behind parameter inference and model comparison will now be described, in the next section the specific implementation used in this thesis will then be discussed. A parameter inference problem assumes that the observed data D can be fully interpreted by an assumed model M , which has a parameter set $\theta = [\theta_1, \theta_2, \dots, \theta_N]$. The aim is to obtain the values of the model parameters θ that best described the observed data D , or to compare multiple different models and determine which is the most probable based on the data. The standard formulation of Bayesian parameter inference relies on three definitions:

1. The prior probability density function (PDF) $P(\theta)$ represents the knowledge about the model parameters θ before considering the observational data D . This is where knowledge from previous measurements or a model parameter being confined to a certain range may be included, and how the results are influenced by this prior information can be readily quantified.
2. The likelihood function $P(D|\theta)$ describes the conditional probability to obtain the observed data D for a set of values, θ , of the model parameters, i.e a function of θ with fixed D .
3. The posterior PDF $P(\theta|D)$ describes the conditional probability that the model parameters are equal to θ under condition of observed data being equal to D and the assumed model, i.e a function of D with fixed θ . Computing this distribution is normally the main goal in Bayesian inference codes.

These three quantities are connected via the Bayes theorem

$$P(\theta|D) = \frac{P(D|\theta) P(\theta)}{P(D)}. \quad (1.55)$$

where the normalisation constant $P(D)$ in denominator is the Bayesian evidence or marginal likelihood, given by

$$P(D) = \int P(D|\theta) P(\theta) d\theta. \quad (1.56)$$

This is an integral of the likelihood over the prior distribution, which normalises the likelihood such that it becomes a probability.

For the prior probability $P(\theta)$ and likelihood $P(D|\theta)$ functions, the posterior probability distribution $P(\theta|D)$ can be calculated for any value of the parameter set θ using Eq. (1.55). For seismological applications the aim is to obtain the most probable value and corresponding uncertainties for each parameter θ_i , which are the physical parameters which best explain the observed data, given model M . To

obtain these values the full marginalised posterior is calculated for each parameter as

$$P(\theta_i|D) = \int P(\theta_1, \theta_2, \dots, \theta_N|D) d\theta_{k \neq i}. \quad (1.57)$$

This posterior distribution includes all the information for the given model parameter, from both the prior and the data. The uncertainty from all of the model parameters is taken into account in the uncertainty of the parameter of interest for which the integral is computed. To define a particular value for model parameter θ_i , the median value, or peak value of the distribution can be taken. Alternatively, the maximum a posteriori value of the parameter can be estimated, θ_i^{MAP} , which is the value which maximises the posterior, $P(\theta|D)$.

For low-parametric models the integrals in Equation (1.57) can be calculated directly using standard numerical integration methods. However, this is not possible for models with a large set of parameters due to the increase in the computation time. Therefore, sampling methods, such as Markov Chain Monte Carlo (MCMC), are often used for complex models. This is described further in Section 1.7.4.

For model comparison purposes the Bayes factor can be obtained from the ratio of the Bayesian evidence (1.56) for two models to be compared. This allows us to quantify how plausible one model is compared to the other. For two models M_i and M_j the Bayes factor is defined as

$$B_{ij} = \frac{P(D|M_i)}{P(D|M_j)}, \quad (1.58)$$

where $P(D|M)$ are defined as above. To define evidence thresholds the natural logarithm of this factor, *i.e.*

$$K_{ij} = 2 \ln B_{ij}, \quad (1.59)$$

is often considered, where values of K_{ij} greater than 2, 6 and 10 correspond to “positive”, “strong”, and “very strong” evidence for model M_i over model M_j , respectively [Kass & Raftery, 1995]. Negative values indicate evidence for model M_j subject to the same thresholds.

1.7.4 Bayesian inference implementation

For the applications presented in this thesis, the marginalised posteriors (Equation 1.57) cannot be practically calculated by direct or numerical integration. Therefore a sampling approach is employed which uses Markov-Chain Monte-Carlo (MCMC) sampling, which allows us to obtain samples from the posterior probability distribution $P(\theta|D)$. When a sufficient number of samples are obtained, the marginalised posterior can be approximated by constructing a histogram for the desired model

parameter θ_i .

The sampling algorithm used generates samples from the posterior distribution using a function which is proportional to that distribution. The classic Metropolis-Hasting random walk algorithm is used [Metropolis et al., 1953] (See Allison & Dunkley [2014] for a comparison of different sampling techniques). The multivariate normal distribution is used as the proposal distribution. The sampling algorithm finds the maximum probability area in the parameter space and is then carried out again to obtain a chain which explores this high probability region, and removes any dependence on the starting values of the parameters. The generated samples are accepted or rejected based on a certain criteria, and can then be used to produce histograms which represent the marginalised posteriors $P(\theta_i|D)$.

Finally, the fitting routine used assumes that the error corresponding to the measurements (Y_i) is normally distributed with a standard deviation of σ_Y . In this case, the likelihood function to be computed as part of Equation 1.55 is the product of N_d Gaussian functions

$$P(D|\theta) = \frac{1}{(2\pi\sigma_Y^2)^{\frac{N_d}{2}}} \prod_{i=1}^{N_d} \exp \left\{ -\frac{[Y_i - M(X, \theta)]^2}{2\sigma_Y^2} \right\}. \quad (1.60)$$

The measurement error σ_Y is considered as one of the unknown parameters. This approach allows robust estimation of the uncertainties of the inferred parameters, irrespective of whether the data have reliable uncertainties themselves.

Together, this approach allows the construction of a histogram which approximates the posterior probability distribution for each model parameter, which is independent of the starting parameters. From this, inferred values of the parameter and the corresponding uncertainty can be obtained, which includes the uncertainty from the variation of the other model parameters. This also allows the calculation of the Bayesian evidence for a given model and data, which allows quantitative comparison of different models for a given data set.

Chapter 2

Statistical studies of decaying kink oscillations

2.1 Introduction

Despite intensive studies of large amplitude kink (transverse) oscillations of coronal loops over the two last decades, a large scale statistical investigation of the oscillation parameters has not been made. Previous studies have analysed a handful of oscillations at a time [e.g. [White & Verwichte, 2012](#)], or have compiled the results from several studies [e.g. [Verwichte et al., 2013b](#)]. In this chapter the first large scale statistical study of kink oscillations using SDO/AIA EUV imaging data is presented. Details of this instrument are given in Section 1.6, and details of the oscillations themselves are given in Section 1.4. 58 kink oscillation events were analysed, observed during 2010-2014. Parameters of the oscillations, including the initial apparent amplitude, period, length of the oscillating loop, and damping are studied for 120 individual loop oscillations. This is done with the aim of establishing the typical parameters of the oscillations and loops, which will help inform future numerical and analytical studies, as well as designs and expectations for future coronal imaging instruments. As mentioned in Section 1.4.1 the damping of these oscillations is an intensively studied area so this is also an aim of the study. Finally, motivated by the discussion in Section 1.4.4 the discovery of signatures of non-linearity within the oscillations is also an aim. In Section 2.2 the data and analysis are described, in Section 2.3 the results are presented. In Section 2.4 a search for signatures of non-linearity in the data set presented here as well as historic kink oscillation data is presented. Discussion and conclusions are given in Section 2.5.

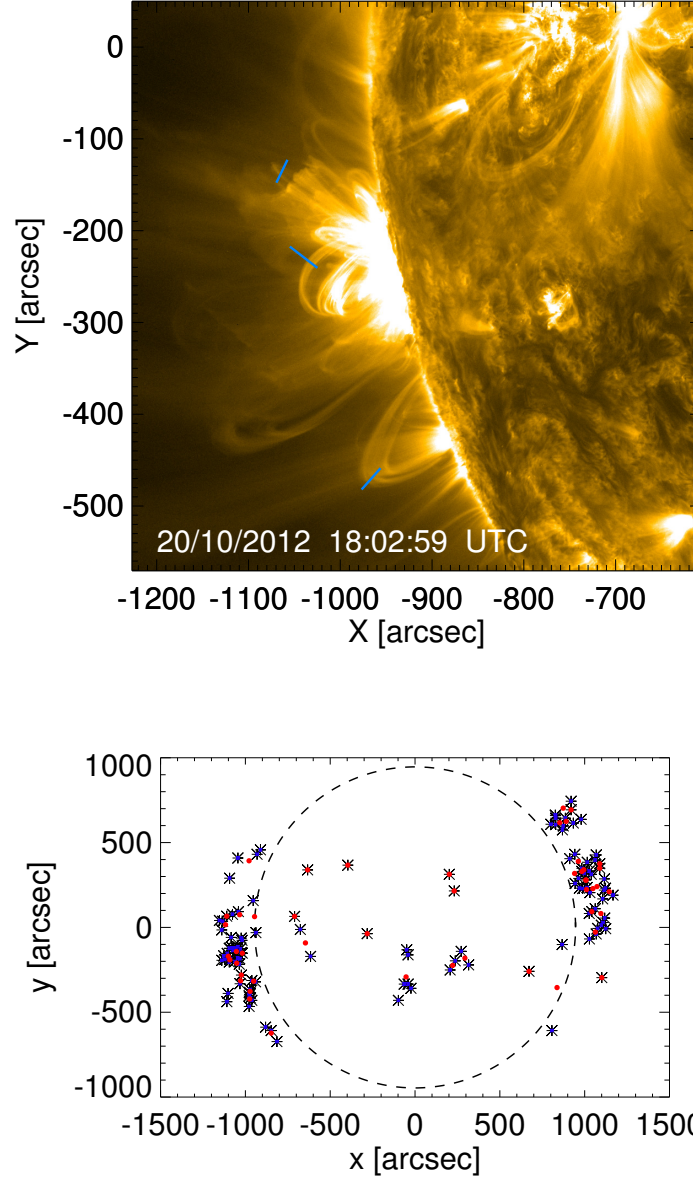


Figure 2.1: Left: The active region from event number 40 from Table 2.2. The three blue lines show some of the slits used to create time-distance maps for analysing the oscillations of the corresponding loops. Right: The slit positions (x_1, y_1 from Table 2.2) used to produce the sample of time-distance maps to analyse kink oscillations of coronal loops, plotted as blue asterisks. The overplotted red circles are the average slit position for each event.

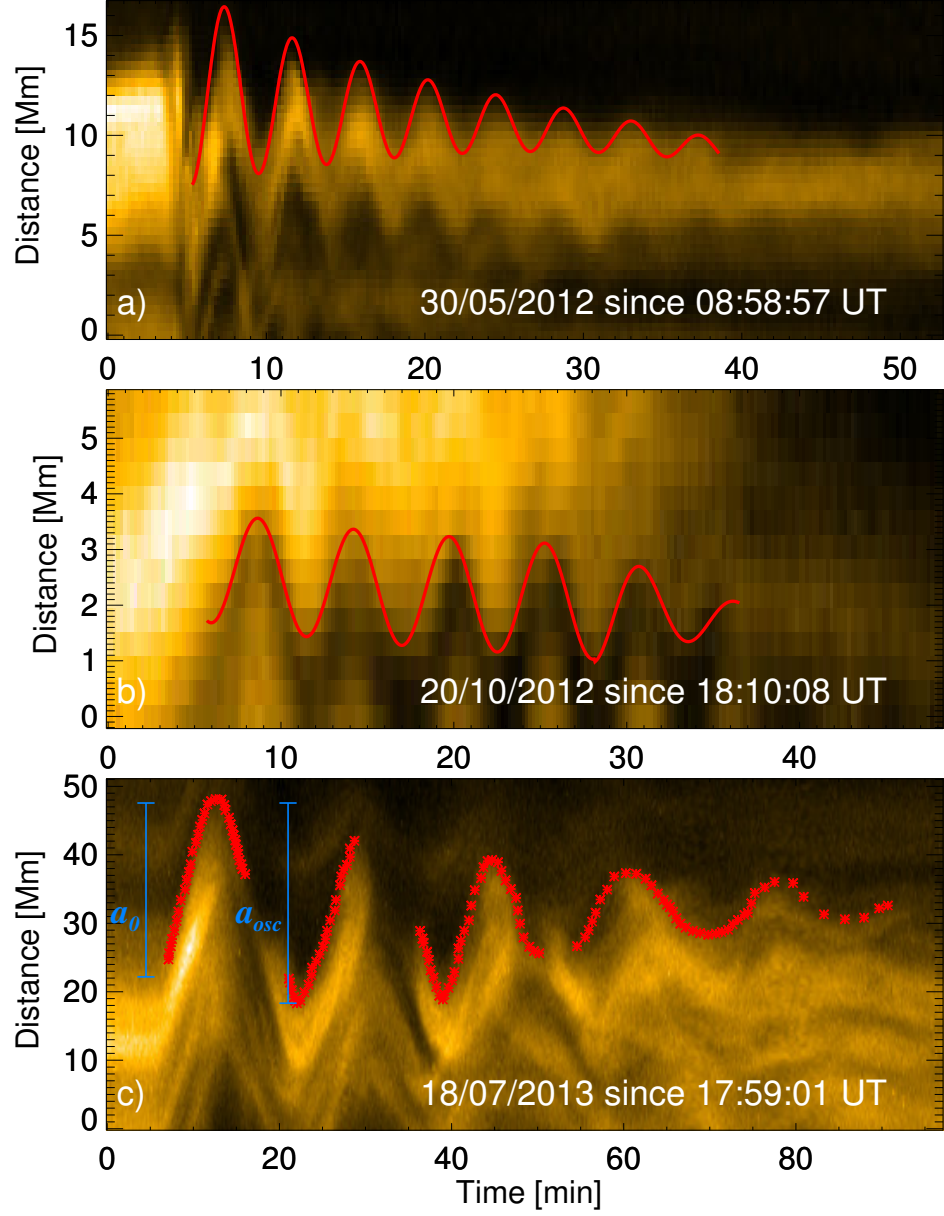


Figure 2.2: Three typical time-distance maps, corresponding to loop 1 from event 32, loop 4 from event 40, and loop 2 from event 48. The fits correspond to the detrending polynomial added to the sinusoidal fit, and multiplied by the exponential damping profile for panels a) and b). The red points in panel c) were taken by eye to map out the oscillation and used for the subsequent fitting. The vertical blue bars represent the measurement of the initial displacement (a_0) and the initial oscillation amplitude (a_{osc} in the figure, A_0 throughout the text) of the upper loop edge.

2.2 Observations and Analysis

Large amplitude decaying kink oscillations of coronal loops from the catalogue in [Zimovets & Nakariakov \[2015\]](#) are analysed using 171 Å data from SDO/AIA, discussed in Section 1.7. A series of images was obtained for each of the 58 eruptive events listed using the provided date, oscillation time and location to define a field of view and time interval which were subsequently submitted as a SSW cut-out request. The data cubes obtained had a time span of 30 or 45 minutes (which was extended for long period oscillations), the standard pixel size of 0.6 arcsec, and a temporal cadence of 12 s, or 24 s in some cases, when the intermediate image was not returned due to a short exposure time.

Movies created from the data cubes were initially inspected by eye, and loop oscillations with sufficient quality for TD analysis were noted. TD maps were created by taking linear slits with a 5 pixel width perpendicular to the oscillating loop and stacking the intensities along the slit (averaged over the width to increase the signal-to-noise ratio) in time, as described in Section 1.7.1. An example of an active region is shown in Fig. 2.1, with the slits used to create TD maps of different loops overplotted. This process resulted in 127 TD maps, which were interpolated to an equispaced temporal grid of 12 s. The extrema of the slits used are listed in Table 2.2, along with the event number from [Zimovets & Nakariakov \[2015\]](#) and a loop ID. The locations of the first extrema of each slit is overplotted on the disk in Fig. 2.1 in blue, and the average slit position for each event is plotted in red.

The projected loop length was estimated for each oscillating loop. The major radius (via the apparent loop height) or diameter (via the distance between footpoints) was measured by eye, depending on the orientation of the loop with respect to the Line Of Sight (LOS), and a semicircular loop approximation was used, $L = \pi R$, where R is the loops major radius. The loop lengths are listed in Table 2.2. In a few cases the loop length could not be estimated as the footpoint positions or height could not be determined.

For each TD map the amplitude of the initial displacement and the initial oscillation amplitude were estimated. The initial displacement is defined as the difference between the initial loop position and the first maxima, and the initial amplitude is defined between the first maxima and minima, as shown in Fig. 2.2, panel c). In this case the displacement of the loops upper edge was estimated. The start time of the oscillation was also recorded, in addition to the number of oscillation cycles observed, all listed in Table 2.2.

Automatic tracking of the loop to record the oscillation was not appropriate in many cases due to the overlap of multiple loops, or only the edge of the oscillating loop being clearly defined. Due to this the oscillations were mapped out by taking a series of points along the centre or edge of the loops by hand, and an error for

the points was defined based on the clarity of the time-distance map, ± 1 pixel in most cases. Three examples of TD maps are shown in Fig. 2.2, the points used to define the oscillation are overplotted in panel c) of Fig. 2.2, where the loop edge was mapped out and points were not taken when its position could not be reliably determined.

There is a certain degree of subjectiveness and error associated with the loop length measurement, the displacement measurements and the points taken to map out the oscillation, however the sample size is large enough that this will not affect the overall results.

The data points for each oscillation were detrended by fitting with a second order polynomial function of the form $y = B_0 + B_1t + B_2t^2$, and subtracting this from the data. All fitting was performed with user defined functions and the IDL routine `mpfitexpr.pro`. Fitting with a sinusoidal function, of the form $y = A \sin(2\pi t/P + \phi)$, was performed for each detrended oscillation, with the period (P) as one of the free parameters. The best fitting period and the corresponding error were recorded for each well defined oscillation.

To analyse the damping behaviour of the oscillations the absolute value of the detrended oscillatory signal was taken and scrutinised by eye. For $>50\%$ of the TD maps clear damping could not be seen, or the number of oscillation cycles was not sufficient to perform fitting of the damping envelope. However these oscillations are still clearly part of the decaying, rather than decayless, regime, discussed in Section 1.4. For oscillations with a clear exponential decaying trend a weighted fit, of the form $A(t) = A_0 e^{-t/\tau}$, was performed on the maxima of the absolute value of the detrended signal. The damping time (τ) and the corresponding error were recorded. For cases where the damping was not observed for the whole duration of the signal, or where there were clearly non-exponential regions of the damping envelope, the fit was only made for the region which was approximated well by an exponential decay. By eye it was determined whether each damping profile was best described by a purely exponential profile (see Fig. 2.2 panel a)), or a combination of both non-exponential and exponential profiles (see Fig. 2.2 panel b)).

The result of the whole fitting process is overplotted on the TD maps in Fig. 2.2, where the detrending polynomial has been added to the sinusoidal fit, as well as the damping profile for panels a) and b). For panel a) the damping profile was measured for the whole signal, for panel b) it was only measured for the last 2 cycles.

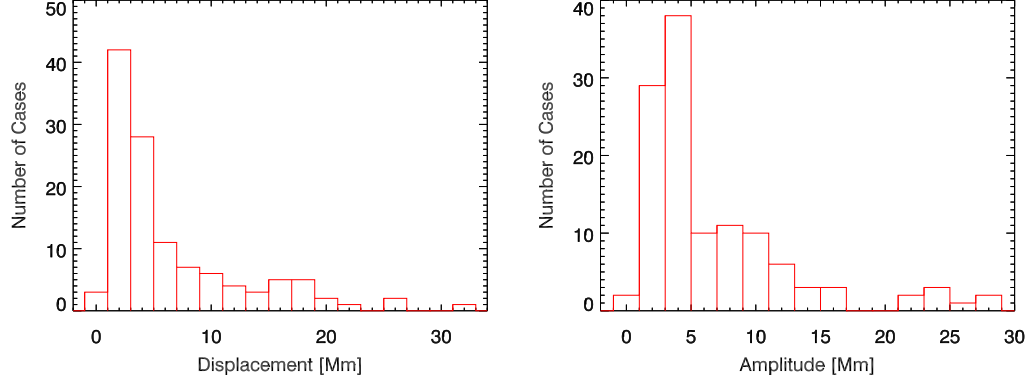


Figure 2.3: Left: The distribution of the measured initial displacement of 120 kink oscillations of coronal loops. Right: The distribution of the measured initial oscillation amplitude of 120 kink oscillations of coronal loops, recorded from the first cycle of oscillation after the initial displacement. The bin size of both histograms is 2 Mm.

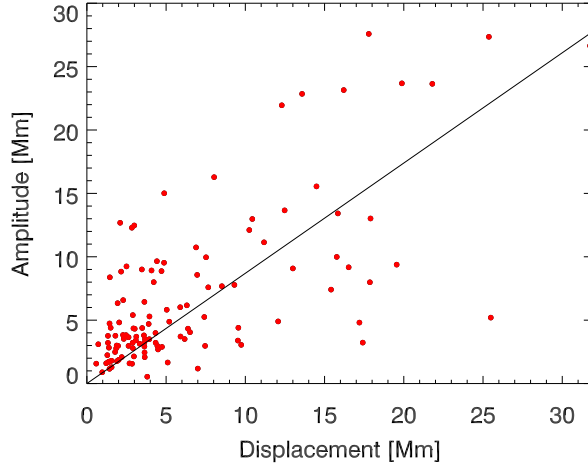


Figure 2.4: The initial oscillation amplitude of 120 kink oscillations of coronal loops, plotted against the initial displacement of the loop position. A linear fit of the data passing through the origin is shown by the solid black line, with a gradient of 0.87 ± 0.01 .

2.3 Results

From the 58 events analysed the periods of 120 individual kink oscillations were determined, and for 118 of these the corresponding loop length was estimated. From the oscillatory signals 52 exponential damping times were obtained. In addition to these measurements other details of the oscillations were recorded, and are listed in Table 2.2. This included whether damping was observed, and if so whether it is best described by a purely exponential, or a combination of non-exponential and exponential damping profiles. The number of oscillation cycles was also recorded, however in many cases this was limited by the oscillatory signal becoming unclear, rather than the damping reducing the amplitude to an undetectable level. These non-exponential sections of the damping envelope could be explained by the proposed Gaussian damping regime, discussed in Section 1.4.1.

2.3.1 Oscillation parameter histograms

Analysis of the amplitudes of the initial displacement and subsequent oscillation may allow inferences to be made about the excitation mechanism, as well as giving details of the typical spatial scales involved. The measured initial loop displacements ranged from 0.6 to 31.8 Mm. In Fig. 2.3 a histogram of the measured initial loop displacements is shown, with a bin size of 2 Mm. The distribution peaks strongly at 1–3 Mm, and 59% of the measurements are covered by the range 1–5 Mm. The distribution after this range is more uniform, but the number of cases decreases towards the upper limit.

The initial oscillation amplitudes ranged from 0.5 to 27.6 Mm. In Fig. 2.3 a histogram of the measured initial oscillation amplitudes is shown, with a bin size of 2 Mm. The distribution peaks at 4–5 Mm, with 57% of the measurements lying in the range 1–5 Mm. The distribution again flattens and decreases towards the upper limit of the measurements.

In Fig. 2.4 the initial oscillation amplitude is plotted against the initial loop displacement. A rough correlation between these two parameters is observed. A linear fit of the data cloud which passes through the origin gives a gradient of 0.86 ± 0.01 .

The measured oscillation periods ranged from 1.5 to 28 min. In Fig. 2.5 a histogram of the measured oscillation periods is shown. The distribution peaks at 4–7 mins, and drops quickly to the maximum detected period, 28 min (not shown in the histogram). No periods below 1.5 min were recorded, and there is a decrease in occurrence approaching the lower periods. In Fig. 2.5 a histogram of the measured loop lengths is shown. The most common length is in the range 220–260 Mm, but there is a roughly even distribution between 140 and 460 Mm which decreases

above and below this range, with minimum and maximum values of 77 and 596 Mm, respectively.

2.3.2 Dependence of the period on loop length

In Fig. 2.6 the period is plotted against the loop length, and the period clearly increases with the length of the coronal loop. The period errors correspond to the scaled covariance from the period fitting. An unweighted linear fit was made, due to the errors alone not determining or reflecting the distribution of the data, due to the variation of the density contrast and Alfvén speed and between different loops and active regions.

The black line correspond to an unweighted linear fit of the data. The best fitting linear function is $P[\text{min}] = (0.025 \pm 0.001)L[\text{Mm}]$, where L is the loop length and P is the period, giving a kink speed of $C_k = (1300 \pm 50) \text{ km s}^{-1}$ from the gradient and the equation $P = 2L/C_k$. The gradient can be varied to give upper and lower bounds to the data cloud, giving a kink speed range of $C_k = (800\text{--}3300) \text{ km s}^{-1}$. Calculation of the kink speed for each individual data point gives the distribution shown in the inset histogram. This has a most common value of $900\text{--}1100 \text{ km s}^{-1}$, a peak value of $1340 \pm 60 \text{ km s}^{-1}$ and a Gaussian width of $620 \pm 60 \text{ km s}^{-1}$, the later two values were obtained by fitting the observed distribution with a Gaussian model.

2.3.3 Relationship between the damping time and period

In Fig. 2.6 the damping time is plotted against the period, and a correlation between the two parameters is obtained. The damping time errors correspond to the scaled covariance from the exponential damping fits. The statistics are limited to the cases where the damping time could be measured (see Table 2.2), so the figure is less populated than Fig. 2.6. A weighted linear fit was made, corresponding to the solid black line. The best fitting linear function is $\tau[\text{min}] = (1.53 \pm 0.03)P[\text{min}]$, where τ is the damping time and P is the period. These results offer no more clarity than in the previous attempts to analyse this dependence.

In Fig. 2.6 the red circles correspond to damping profiles which were determined to be exponential by eye, and the blue squares correspond to damping profiles best described by a combination of a non-exponential and exponential profile. For the latter case, which corresponds to 21 of the measurements, the damping time is determined from the exponential part of the profile. This corresponds to the values “E ” and “E,NE ” in the column “Damping Profile ” in Table 2.2. No difference between the two cases is observed. There are 9 additional cases where the profile appears to be purely non-exponential, and no damping time was measured, noted in Table 2.2 by “NE ”.

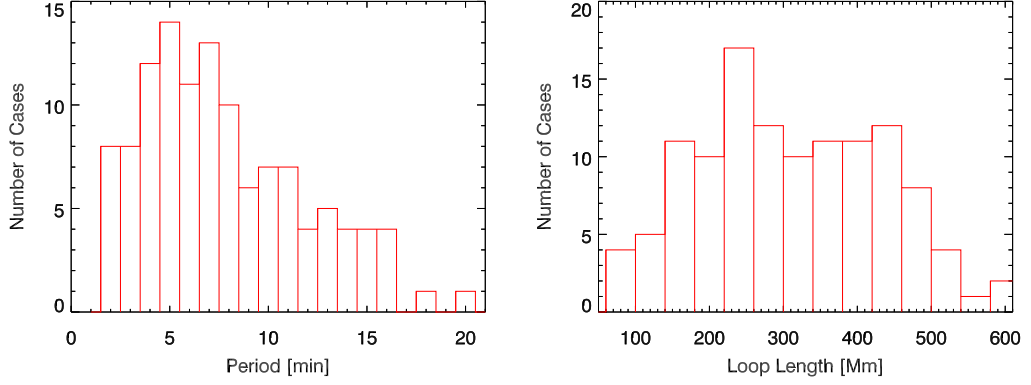


Figure 2.5: Left: The distribution of the measured periods of 120 individual kink oscillations of coronal loops. The bin size is 1 min. Right: The distribution of the measured loop lengths for 118 individual coronal loops, which undergo kink oscillations. The bin size is 20 Mm.

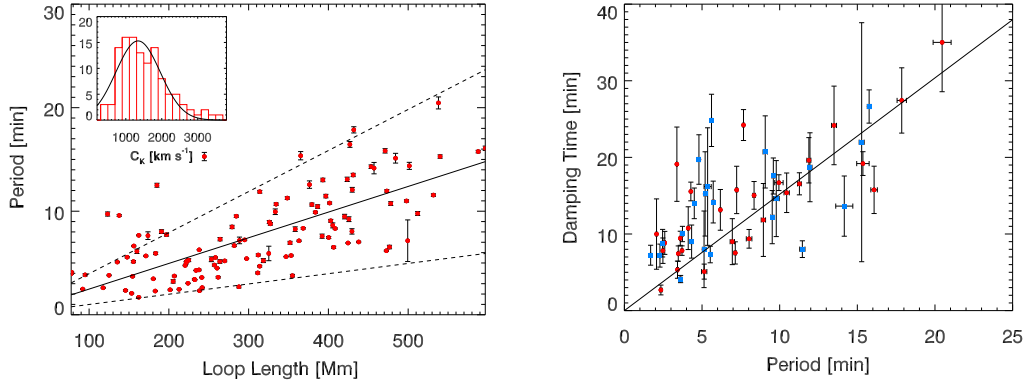


Figure 2.6: Left: period plotted against loop length for 118 kink oscillations of coronal loops. The solid black line correspond to an unweighted linear fit of the data. The best fitting linear function gives a kink speed of $C_k = (1300 \pm 50) \text{ km s}^{-1}$ from its gradient. The dashed lines correspond to kink speeds of 800 and 3300 km s^{-1} for the upper and lower lines respectively. Right: damping time plotted against period for 54 kink oscillations of coronal loops. The solid black line correspond to a weighted linear fit of the data. The best fitting linear function is $\tau[\text{min}] = (1.53 \pm 0.03)P[\text{min}]$. The red circles correspond to damping envelopes best described by an exponential profile, and the blue squares correspond to those best described by a combination of a non-exponential and exponential profiles.

2.4 Amplitude dependence of kink oscillation damping

In this section the empirical dependence of the kink oscillation quality factor, the ratio of damping time to oscillation period, on the oscillation amplitude is investigated. Decaying kink oscillation events detected previously with TRACE, SDO/AIA and STEREO/EUVI in the extreme ultraviolet (EUV) 171Å band were included, as well as the original data used and described in this chapter. Despite significant progress in the development of the non-linear theory of kink oscillations, there is still no a clear picture of the quantitative effect of the finite amplitude on the behaviour and damping of these oscillations. Further progress in understanding the role of the non-linearity and the exploitation of its seismological potential requires observational guidance. This work aims to establish empirically the relationship between the damping time and amplitude of kink oscillations. In Section 2.4.1 the data used and the method of analysis are described. In Section 2.4.2 the results are described. The findings are discussed and summarised in Section 2.5.4.

2.4.1 Observations

Parameters of the kink oscillations used in this study, from the work presented above, are shown in Table 2.2. This data is supplemented by other previously published events detected with TRACE and STEREO/EUVI. The damping time, period, and apparent (projected) amplitude of the oscillations were retrieved where possible (see Section 2.2 for details). Some published detections had to be omitted as the amplitude of the oscillation was not reported and could not be reliably estimated from the provided figures. These additional data are summarised in Table 2.1.

2.4.2 Results

Fig. 2.7 shows the distribution of the observed apparent amplitudes of kink oscillations. This figure is a modification of Fig. 2.3 of Section 2.3, adding the results obtained for the events shown in Table 2.1. There appears to be no significant difference between these two figures, other than fewer statistics, as only about half of the events discussed in the previous section are used in this work. Also, in the current figure, the highest amplitude tail is absent, as in that part of the distribution the oscillations do not have enough cycles to measure damping.

In the left panel of Fig. 2.8 the quality factor of the kink oscillations, defined as the ratio of the damping time to the period, is plotted against the apparent initial amplitude of the oscillation. A negative dependence between the two parameters is evident, with Spearman and Pearson correlation coefficients of -0.44 and -0.42, and p-values of 6×10^{-5} and 5×10^{-5} , respectively. It is clear that larger amplitudes correspond to systematically smaller quality factors. The dependence has a trian-

Table 2.1: Damping times, periods, and apparent amplitudes of kink oscillations of coronal loops.

Ref (#)	Damping time (s)	Period (s)	Amplitude (Mm)
1	870	261	0.8
1	300	265	2
1	500	316	6
1	400	277	4
1	849	272	5
1	600	435	0.7
1	200	143	0.5
1	800	423	0.7
1	200	185	9
1	400	396	1.8
2	714	234	7.9
3	920	249	0.34
3	1260	448	0.43
3	1830	392	0.49
3	1330	382	0.42
3	1030	358	0.56
3	980	326	0.22
3	1320	357	0.24
4	2129	436	0.4
4	1200	243	0.4
5	521	895	7.3
5	473	452	3.7
6	1000	630	3.7
7	3660	2418	5
8	500	377	9.5

The data listed were previously detected using TRACE and STEREO/EUVI. The first column indicates the publication the results are taken from:

- 1: [Aschwanden et al. \[2002\]](#), 2: [Wang & Solanki \[2004\]](#),
3: [Verwichte et al. \[2004\]](#), 4: [Van Doorselaere et al. \[2007\]](#),
5: [De Moortel & Brady \[2007\]](#), 6: [Verwichte et al. \[2009\]](#),
7: [Verwichte et al. \[2010\]](#), 8: [Mrozek \[2011\]](#).

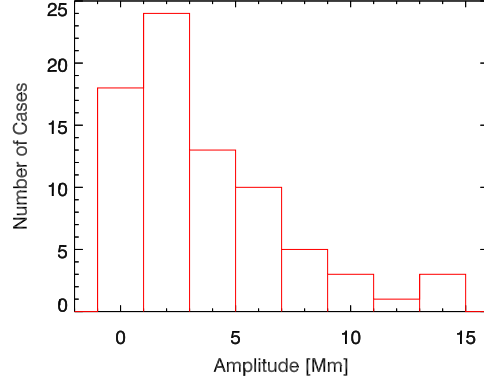


Figure 2.7: Distribution of the measured apparent initial amplitude of kink oscillations of coronal loops, detected with SDO/AIA, TRACE, and STEREO/EUVI. The bin size is 2 Mm.

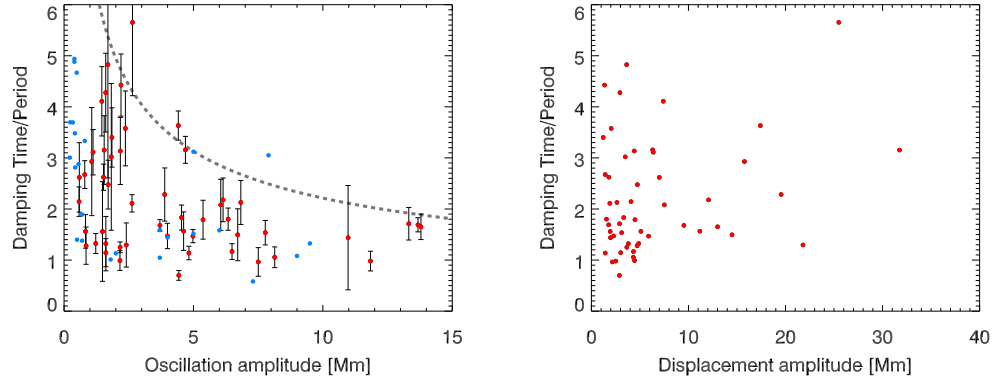


Figure 2.8: Left: the quality factor of kink oscillations of coronal loops determined as the ratio of damping time to the oscillation period, plotted against the apparent oscillation amplitude. The red points are taken from Table 2.2. The blue points correspond to those listed in Table 2.1. The grey line shows the scaling of the quality factor with the maximum apparent amplitude. Right: the quality factor plotted against the apparent amplitude of the initial displacement that excited the oscillation. The data is taken from Table 2.2.

gular shape on the quality factor – apparent amplitude plane. For lower apparent amplitudes, up to 3–4 Mm, the quality factor ranges from 1–5, while for higher amplitudes the range of the measured quality factors decreases to 1–2. Unfortunately, different methods of data analysis applied in the different studies summarised in Table 2.1 make it difficult to estimate the error bars of those measurements (blue points in Fig. 2.8).

The upper boundary of the data cloud in Fig. 2.8 can be approximated by the expression

$$q \approx 7 \times A[\text{Mm}]^{-1/2}, \quad (2.1)$$

where q is the quality factor and A is the kink oscillation amplitude. In the lack of a large number of observations this best-fitting curve was made by eye, and should only be considered a first attempt to quantify this scaling. A fit to the main body of the data was not considered to be significant as this is affected by the suppression of the amplitudes by the unknown LOS angle, which is discussed further below.

In the right panel of Fig. 2.8 the quality factor of the oscillations is plotted against the apparent amplitude of the initial displacement that excited the oscillation. In contrast to the left panel, no correlation is seen despite the weak correlation between the amplitude and displacement from earlier in the chapter. This indicates that the amplitude of the oscillation itself, rather than amplitude of the initial displacement, affects the quality factor and, therefore, the damping of the oscillations.

2.5 Discussion and conclusions

A comprehensive statistical analysis of large amplitude decaying kink oscillations of coronal loops excited by flaring events, observed with SDO/AIA at 171 Å has been presented in this chapter. Additionally the amplitude dependence of the quality factor of the oscillations was explored. The results are now discussed and summarised.

2.5.1 Oscillation parameter histograms

Details of the initial loop displacement and the subsequent oscillation have been analysed. Fig. 2.3 indicates that lower amplitude initial displacements are more common, and Fig. 2.3 shows that relatively low initial oscillation amplitudes are also more common. A comparison between the two histograms mentioned leads to the conclusion that the initial displacement prescribes the initial amplitude of oscillation in the majority of cases. However, there are cases where a large initial displacement leads to a new equilibrium position for the loop, where it oscillates with an amplitude much smaller than the initial displacement, as recently discussed by [Russell et al. \[2015\]](#). Cases where a small initial displacement results in a larger amplitude oscillation are also seen. A simple explanation is that the passage of the

LCE has left the external plasma and magnetic field more rarefied, and the perturbed loop passes through its initial equilibrium with an amplitude greater than the initial displacement. A linear correlation between these two parameters is seen in Fig. 2.4, with spreading due to measurement errors, but also reflecting the different regimes discussed above.

The above results are subject to a LOS effect. The histograms in Fig. 2.3 will include an effect in the distribution due to how the observed kink oscillations are distributed over the LOS angles. If all the initial displacements and oscillation amplitudes were equal, distributions would still be obtained due to the different LOS angles varying the measured values. It can be seen from Fig. 2.1 that loop positions are mostly off-limb, near the equator, so North-South oscillation polarisations were better detected. Further work is required to remove the effect of the varying LOS angles from the measurements and obtain the true displacements and oscillation amplitudes.

Some inferences can be made from the period distribution shown in Fig. 2.5. The drop off in the occurrence of higher periods is likely to reflect a physical drop-off, as larger length loops may be less likely to be formed and are also more difficult to detect. The decrease in the distribution for lower periods may include an observational bias, as oscillations of shorter loops are more difficult to observe, but may also reflect the excitation mechanism. If, as proposed by [Zimovets & Nakariakov \[2015\]](#), excitation due to LCE perturbations is the dominant mechanism, this should preferentially excite loops above a certain height, which have correspondingly longer lengths. The distributions of the periods and loop lengths differ, and this is likely to be due to the loop length estimations becoming more inaccurate for longer loops, as well as variation of the additional parameters which prescribe the period of oscillation.

If general statistics of the loop lengths were available it could be used to normalise the loop length distribution in Fig. 2.5. This would allow it to be determined whether kink oscillations occur in all loops with the same probability or if loops of certain lengths are more likely to undergo a kink oscillation. LOS effects should also be included in such a study, and the varying ellipticity of the loops themselves, as well as the inclination angle of the loop plane from vertical.

2.5.2 Dependence of the period on loop length

The period scales with the loop length as expected, and the best fitting kink speed of $C_k = (1300 \pm 50) \text{ km s}^{-1}$ is in agreement with previous results [[Ofman & Aschwanden, 2002](#); [Verwichte et al., 2013b](#)]. The range of kink speeds from the main data cloud ($C_k = (800\text{--}3300) \text{ km s}^{-1}$) should correspond to the spread of loop density contrasts and Alfvén speeds. There are some points in Fig. 2.6 corresponding to short loops

with larger periods than expected from the main body of the data, giving a lower kink speed value. These data points may correspond to loops and active regions with significantly lower Alfvén speeds, or greater density contrasts. More statistics and analysis of the active region parameters are required to determine if these points have a physical explanation, or are due to measurement errors.

Comparisons can be made with the results of a similar study which focused on the decayless regime of kink oscillations [Anfinogentov et al., 2015a], as discussed in Section 1.4. They obtained a similar scaling of period with loop length, but with a lower gradient, and therefore, a higher best fitting kink speed of $C_k=(1850\pm70)$ km s⁻¹. The period distribution they present is similar to the distribution obtained here, but peaks at a lower value, and their loop length distribution is significantly less uniform. These differences may be due to a selection effect from their study, as the data spanned 1 month, whereas the data presented here spans 4 years. It may also reflect the different driving mechanisms, in particular the excitation mechanism for the decayless regime remains unknown. The discrepancy between the statistics of decaying and decayless kink oscillations should be further investigated when a larger set of events becomes available.

2.5.3 Relationship between the damping time and period

The results on the linear scaling of the damping time with the oscillation period are qualitatively consistent with the previously obtained observational results [e.g. Aschwanden et al., 2003; Verwichte et al., 2013b], as the data can be fit with a linear relationship between the two parameters. The spread of the data makes it unreasonable to make inferences about the damping mechanism from the observed dependence however, as the different mechanisms in Section 1.4.1 should lead to different relationships being observed. In particular it is not possible to discriminate between a linear or power law dependence, and such an approach requires consideration of the influence of the varying cross sectional loop structuring and other parameters.

Distinguishing between the damping times from oscillations which showed a purely exponential profile and a combination of a non-exponential and exponential (only fitting the exponential section), did not reveal any systematic difference. This indicates that the presence of a non-exponential stage does not affect the exponential stage of the damping. However, the detected damping profiles indicate that in some cases the exponential fitting of the kink oscillation damping is not sufficient to reproduce the whole damping profile. The amplitude of some oscillations remains approximately constant for a significant period of time, but it has not been determined whether this corresponds to a slowly decaying Gaussian damping profile, or a periodic driver sustaining a constant amplitude oscillation.

The detected clearly non-exponential sections of the damping envelopes may be better approximated by a Gaussian profile. If this is confirmed to be the case then this is evidence for the Gaussian damping regime discussed by [Pascoe et al. \[2012\]](#). This will be the subject of further study, as the detection of Gaussian damping envelopes would allow new seismology to be performed, and comparisons with the theoretical predictions to be made. Recently, the data from Table 2.2 was used in a study by [Montes-Solís & Arregui \[2017\]](#), where Bayesian inference was used to try and distinguish between different damping mechanisms based on the damping time to period ratios.

2.5.4 Amplitude dependence of the damping

The roughly triangular shape of the data cloud on the quality factor – apparent amplitude plane has a simple interpretation. The apparent amplitude is proportional to the actual amplitude reduced by the angle between the LOS and the direction of the oscillatory displacement. Thus, if several kink oscillations of the same displacement amplitude are observed, but are randomly distributed with respect to the LOS angle, the apparent amplitudes would range from zero (or the detection threshold determined e.g. by the pixel size, or the loop intensity contrast with the background), to the actual amplitude, for the oscillations displacing the loop in the plane of sky. In other words, for a given value of the quality factor, the apparent amplitudes of kink oscillations measured with randomly distributed LOS angles are distributed in a horizontal stripe in the quality factor – apparent amplitude plane, from zero to the actual amplitude. Fig. 2.8 shows that for higher quality factors the highest apparent amplitudes are systematically lower. Thus, the triangular shape of the data cloud clearly demonstrates the decrease in the quality factor with the amplitude. The quality factor dependence on the oscillation amplitude is approximated by the power-law dependence with the exponent of $-1/2$, however this is a by eye estimate, and a more rigorous estimation of the scaling law requires more accurate measurements and increased statistics. The physical mechanism responsible for this dependence needs to be revealed.

The same reasoning is applicable to the dependence of the quality factor on the apparent initial displacement amplitude. This dependence is more scattered than the quality factor plotted against the oscillation amplitude, and there is no clear dependence between the two parameters. The data from previous studies is not included as measurements of the initial displacement were not as readily available. The initial displacement and oscillation amplitude of kink oscillations are different parameters, as the loop can oscillate around a new equilibrium after the initial displacement [[Zimovets & Nakariakov, 2015](#)]. The difference between the initial displacement and the observed amplitude could also be attributed to

the excitation of leaky modes and higher harmonics, which was numerically found by [Terradas et al. \[2007\]](#) who considered the excitation of kink oscillations by a magnetic pressure pulse.

Thus, the main finding is the demonstration of the dependence of the kink oscillation quality factor on the oscillation amplitude. This result indicates that the damping mechanism depends upon the amplitude and hence is non-linear. The dependence seems to be smooth, with a gradual decrease in the quality factor with the amplitude, and does not have a clear break that would indicate the presence of a threshold typical for shear-flow instabilities, such as KHI, as discussed in Section 1.4.4. However, the lack of break may be attributed to insufficient statistics, and the use of a larger set of oscillatory events could change this conclusion. Recently a qualitative similarity was noted between the results presented here and the results of numerical simulations of non-linear kink oscillations presented in [Magyar & Van Doorselaere \[2016a\]](#).

2.5.5 Conclusion

The main findings are summarised as follows;

- The initial loop displacement prescribes the initial oscillation amplitude in general.
- The period scales linearly with the loop length, as expected, and a kink speed of $C_k=(1300\pm50)$ km s⁻¹ is obtained, with the majority of the data points lying in the range (800–3300) km s⁻¹, following a Gaussian distribution.
- A linear scaling of the damping time with period is observed, and non-exponential damping profiles have been detected.
- The quality factor of the oscillations was shown to be amplitude dependent.

In conclusion, a statistically significant number of individual kink oscillations has been analysed, and histograms of the measured parameters have allowed insightful inferences to be made. Details of the distribution of amplitudes, periods and loop lengths may be useful when considering the observational capabilities of future instruments. In addition the scaling between different parameters has been studied, and the damping behaviour has been characterised, both of which, after further work, may allow seismological inferences and measurements to be made.

Table 2.2: A list of 120 coronal loop kink oscillations detected with AIA/SDO and their measured parameters. The event ID corresponds to the events catalogued in [Zimovets & Nakariakov \[2015\]](#), and the loop ID distinguishes the different loops in each event (this does not correspond to those in the cited paper). The position of the slit used to produce each time-distance map is given in arcsec, along with the date and oscillation start time in UT. The period and error obtained from fitting the loop oscillation are given, as well as the estimated loop length. The column “Disp Amp” lists the estimated initial loop displacement, and “Osc Amp” is the estimated initial amplitude of the oscillation. The number of cycles that were observed is listed in “N Cyc”. Finally, the exponential damping time and error from fitting the damping profile, and the form of the damping profile (exponential (E), non-exponential(NE), or a combination of both), are listed in the final two columns.

Event ID	Loop ID	Slit Position [x1,y1,x2,y2] (arcsec)	Date	Time UT	Period (min)	Length (Mm)	Disp Amp (Mm)	Osc Amp (Mm)	N Cyc	Damping Time (min)	Damping Profile
1	1	-940,-321,-964,-308	02/08/2010	04:22:49	3.42±0.06	232	5.1	1.7	3	5.34±1.12	E
1	2	-962,-313,-997,-322	02/08/2010	04:22:13	4.11±0.05	78	7.0	1.2	3	10.76±2.79	E
2	1	672,-259,711,-223	16/10/2010	19:13:07	6.64±0.06	156	2.0	4.8	3.5		
3	1	-977,-383,-988,-368	03/11/2010	12:13:48	2.46±0.03	213	1.4	4.7	8	8.8±1.8	E,NE
3	2	-970,-416,-1001,-393	03/11/2010	12:14:35	3.62±0.08	262	4.4	9.7	3	4.12±0.47	E,NE
3	3	-978,-466,-1027,-411	03/11/2010	12:14:23	4.04±0.1	311	4.1	8.9	2		
4	1	912,405,889,433	09/02/2011	01:30:02	2.29±0.03	183	2.9	4.4	4.5	7.18±1.5	E,NE
4	2	969,231,974,278	09/02/2011	01:31:54	3.47±0.03	181	1.4	1.2	3	7.44±1	E
5	1	1089,375,1050,423	10/02/2011	04:43:38	7.03±0.06	438	4.5	3.0	3		NE
6	1	1089,349,1057,398	10/02/2011	06:44:22	8.05±0.26	430	3.8	0.5	2		
7	1	983,330,970,342	10/02/2011	06:57:46	1.69±0.02	162	2.9	3.2	6	7.23±1.3	E,NE
8	1	1007,280,1021,305	10/02/2011	12:35:01	3.74±0.07	207	1.2	1.6	3	10±1	E,NE
9	1	983,348,947,414	10/02/2011	13:43:37	5.14±0.17	264	3.0	4.3	3	5.09±0.98	E

9	2	942,431,934,461	10/02/2011	13:46:31	8.95±0.14	326	3.6	3.2	2.5	11.83±4.76	E
10	1	1106,168,1133,214	11/02/2011	08:07:07	11.46±0.17	397	4.7	8.9	2.5	8.02±1.09	E,NE
10	2	1039,313,1041,334	11/02/2011	08:08:17	8.48±0.16	279	5.9	6.0	2		
11	1	-41,-162,-43,-146	13/02/2011	17:34:28	3.96±0.07	78	3.5	4.4	3		
11	2	-49,-132,-51,-108	13/02/2011	17:34:50	3.85±0.11	95	3.7	2.1	3		
11	3	-64,-334,-69,-316	13/02/2011	17:37:13	2.6±0.05	118	3.1	3.7	6	8.84±1.5	E
11	4	-41,-334,-54,-322	13/02/2011	17:33:52	3.81±0.04	125	2.9	5.4	5		
11	5	-24,-359,-44,-336	13/02/2011	17:33:42	5.09±0.06	135	1.9	6.3	2		
11	6	-98,-430,-89,-394	13/02/2011	17:38:33	6.13±0.21	160	11.2	11.1	2		
12	1	-282,-37,-309,-47	13/02/2011	20:19:17	5.56±0.07	148	1.9	1.8	2		
15	1	202,313,175,371	27/05/2011	10:47:58	7.64±0.37	174	6.3	6.2	1.5		
16	1	1014,235,991,257	11/08/2011	10:17:19	2.62±0.04	242	3.3	3.1	3		
16	2	988,229,1026,229	11/08/2011	10:10:22	2.35±0.07	146	17.4	3.2	2	2.69±0.64	E
16	3	1031,205,1067,241	11/08/2011	10:10:54	5.23±0.19	318	25.5	5.2	2.5		
17	1	231,215,216,263	06/09/2001	22:20:15	2.07±0.04	153	9.5	3.4	3.5	9.99±4.59	E
18	1	-931,431,-960,472	22/09/2011	10:35:08	7.18±0.32	289	15.8	10.0	2.5		
18	2	-911,457,-884,476	22/09/2011	10:26:59	9.52±0.11	284	1.4	1.7	3.5	12.2±3.47	E
18	3	-1093,290,-1060,320	22/09/2011	10:30:32	13.02±0.17	393	4.9	9.5	4		NE
19	1	-954,158,-998,134	23/09/2011	23:51:45	9.73±0.2	123	4.7	2.9	2		
19	2	-938,-31,-992,-12	23/09/2011	23:51:57	11.27±0.12	348	7.5	10.0	2	16.55±1.44	E
20	1	-676,-12,-682,62	14/11/2011	07:21:12	5.36±0.23	253	2.6	3.7	3	16.19±7.67	E,NE
20	2	-616,-171,-665,-161	14/11/2011	00:05:04	13.43±0.67		4.3	4.0	2		
21	1	920,693,907,725	16/11/2011	14:08:19	7.15±2.01	499	1.8	3.8	2		

22	1	995,340,1004,332	16/11/2011	14:56:05	2.7±0.11	288	1.6	1.8	3		
23	1	827,662,813,699	17/11/2011	22:28:37	15.36±0.4	365	6.4	4.3	3	19.19±1.55	E
23	2	920,744,856,729	17/11/2011	22:32:49	28.19±0.51		12.1	4.9	2.5		
24	1	-881,-588,-910,-549	18/11/2011	07:34:59	17.86±0.3	432	14.5	15.6	3	27.43±4.26	E
24	2	-848,-608,-901,-572	18/11/2011	07:29:42	16.45±0.28	427	21.8	23.6	3		
24	3	-814,-673,-894,-645	18/11/2011	07:36:02	20.46±0.58	538	31.8	26.6	2	35.01±6.44	E
25	1	316,-221,321,-195	22/12/2011	01:59:34	5.13±0.11	156	2.0	3.0	3	8±5	E,NE
25	2	272,-141,332,-92	22/12/2011	01:59:39	7.3±0.16	264	1.8	2.5	2.5		
26	1	1098,13,1126,51	16/01/2012	00:08:28	11.95±0.13	473	2.5	9.2	4.5	18.71±4.5	E,NE
26	2	1028,-68,1025,-33	16/01/2012	00:11:27	12.51±0.19	185	2.3	6.6	4		NE
27	1	1042,93,1072,146	09/04/2012	01:19:52	15.28±0.4	244	4.3	3.2	3		
29	1	-633,339,-628,380	08/05/2012	13:05:46	3.71±0.05	154	7.4	5.3	6	7.83±0.62	E
31	1	964,289,945,325	26/05/2012	20:36:47	7.67±0.04	162	19.6	9.4	6	24.22±2.02	E
31	2	944,259,944,284	26/05/2012	20:36:27	9.59±0.09	138	13.0	9.1	5	17.57±2.35	E,NE
31	3	1116,286,1112,330	26/05/2012	20:39:53	11.56±0.12	532	4.5	2.7	2.5		
32	1	-973,-366,-988,-342	30/05/2012	08:58:57	4.28±0.02	234	2.2	8.8	8	15.55±1.22	E
32	2	-972,-388,-989,-370	30/05/2012	08:56:52	3.38±0.02	233	4.0	5.3	5	19.11±4.85	E
33	1	807,-608,840,-591	06/07/2012	23:06:45	4.69±0.08	314	7.0	8.6	2.5		
33	2	867,-101,874,-45	06/07/2012	23:05:07	6.52±0.1	407	8.5	7.7	3		E
34	1	-1053,-142,-1076,-129	07/08/2012	00:59:34	9.95±0.27	333	15.4	7.4	2.5	16.7±1.03	E
35	1	-1024,-148,-1037,-110	07/08/2012	01:34:47	8.78±0.13	327	1.9	3.0	3		
35	2	-1033,-185,-1070,-185	07/08/2012	01:33:52	5.77±0.1	312	1.4	2.8	2.5		
36	1	-1018,-152,-1039,-112	07/08/2012	03:03:46	6.68±0.1	282	1.3	3.8	4		

37	1	-1110,66,-1103,87	15/10/2012	21:52:17	8.27±0.22	358	2.3	3.8	2.5		
38	1	-1046,-180,-1046,-159	19/10/2012	19:01:00	3.04±0.03	224	2.7	1.6	4		
38	2	-1061,-201,-1065,-174	19/10/2012	19:01:44	5.2±0.08	270	3.0	2.1	3	15.23±5.5	E,NE
38	3	-1121,-189,-1142,-175	19/10/2012	19:03:00	13.08±0.21	424	5.2	4.9	2		
38	4	-1139,-194,-1162,-185	19/10/2012	19:01:08	10.74±0.18	478	5.0	5.8	2		
39	1	-1093,-124,-1140,-107	19/10/2012	21:04:19	10.79±0.1	402	6.5	4.1	4.5		NE
39	2	-1088,-185,-1095,-157	19/10/2012	21:01:34	10.68±0.12	334	2.0	1.9	5		NE
39	3	-1095,-204,-1120,-172	19/10/2012	21:03:44	12.57±0.36	376	2.3	3.5	3.5		
39	4	-1127,-168,-1161,-179	19/10/2012	21:00:40	14.3±0.17	454	3.7	3.5	4		NE
40	1	-1025,-63,-1037,-47	20/10/2012	18:07:36	5.68±0.06	171	1.4	1.7	4		
40	2	-1077,-121,-1065,-96	20/10/2012	18:09:33	5.61±0.03	347	9.6	4.4	7	24.83±3.41	E,NE
40	3	-1073,-136,-1058,-120	20/10/2012	18:11:36	5.92±0.7	325	2.6	3.0	4		
40	4	-1045,-114,-1020,-110	20/10/2012	18:10:08	5.53±0.04	258	3.6	2.5	6	7.32±1.08	E,NE
40	5	-1056,-122,-1043,-115	20/10/2012	18:12:55	5.42±0.02	297	3.9	4.7	6		
40	6	-1095,-123,-1079,-101	20/10/2012	18:09:59	6.93±0.04	425	6.2	3.5	11		NE
40	7	-1107,-153,-1094,-121	20/10/2012	18:11:11	5.72±0.06	353	3.1	3.4	12	14.17±2.73	E,NE
40	8	-1036,-217,-1066,-194	20/10/2012	18:08:39	4.33±0.08	238	10.3	12.1	4.5	9.01±2.16	E,NE
40	9	-1109,-438,-1117,-399	20/10/2012	18:11:45	6.18±0.05	473	12.5	13.7	3.5	13.15±2.66	E
40	10	-962,-430,-982,-453	20/10/2012	18:12:21	6.27±0.03	238	2.2	2.1	10		NE
40	11	-978,-404,-999,-418	20/10/2012	18:11:29	4.76±0.04	220	1.6	1.3	4		
43	1	933,615,894,615	07/01/2013	06:37:38	7.14±0.07	363	8.0	16.3	5	7.53±1.45	E
43	2	874,598,890,613	07/01/2013	06:37:50	3.6±0.03	241	9.7	3.1	5	9.44±0.92	E
43	3	828,659,816,708	07/01/2013	06:39:19	8.35±0.08	368	2.1	12.7	3.5	15.04±1.81	E

43	4	829,606,826,620	07/01/2013	06:37:01	5.16±0.03	222	3.9	3.5	4		
43	5	801,608,812,631	07/01/2013	06:37:11	4.5±0.02	260	1.3	2.2	5.5	14±2	E,NE
44	1	829,644,820,687	07/01/2013	08:48:37	7.23±0.06	295	2.8	12.3	5	15.75±3.09	E
44	2	979,637,940,676	07/01/2013	08:48:17	9.78±0.19	512	15.8	13.4	3	14.62±4.96	E,NE
44	3	886,644,936,622	07/01/2013	08:47:19	6.95±0.14	352	17.2	4.8	4	9±3	
44	4	869,575,879,587	07/01/2013	08:48:53	2.41±0.05	202	2.9	2.8	4		
45	1	-396,367,-409,379	17/02/2013	15:45:42	2.48±0.04	92	0.7	3.1	3.5	7.82±1.66	E
46	1	-1024,-281,-1038,-268	24/05/2013	18:55:12	12.07±0.23	430	1.5	4.4	2.5		
46	2	-1102,-389,-1080,-363	24/05/2013	18:53:58	10.99±0.11	498	2.4	3.7	5		NE
46	3	-1032,-332,-1054,-327	24/05/2013	18:54:34	9.9±0.1	384	2.5	3.8	6		NE
47	1	207,-251,223,-243	27/05/2013	01:53:28	5.27±0.14	225	0.6	1.6	3		
47	2	237,-197,270,-188	27/05/2013	02:02:59	5.02±0.12	222	2.9	1.6	3		
48	1	-1076,77,-1044,111	18/07/2013	17:59:56	15.28±0.16	540	12.3	22.0	3.5	21.98±15.6	E,NE
48	2	-1134,36,-1069,99	18/07/2013	17:59:01	15.76±0.12	588	25.4	27.4	5	26.64±2.17	E,NE
48	3	-1153,41,-1102,112	18/07/2013	17:58:34	16.08±0.21	597	19.9	23.7	4	15.76±3.09	E
48	4	-1084,-59,-1069,-33	18/07/2013	17:56:10	9.23±0.23	426	7.7	7.6	4		
48	5	-1139,-15,-1102,42	18/07/2013	17:57:31	15.83±0.21	471	17.9	13.0	3.5		
49	1	-1041,93,-1117,118	11/10/2013	07:12:01	15.12±0.47	484	13.6	22.9	2		
49	2	-1030,-126,-1058,-106	11/10/2013	07:15:17	7.73±0.14	197	3.6	6.4	3		
49	4	-1044,409,-1082,429	11/10/2013	07:13:30	10.45±0.17	386	17.9	8.0	3	15.38±2.58	E
49	5	-1020,-76,-1071,-51	11/10/2013	07:15:51	8.03±0.18	191	10.4	13.0	3	9.37±1.22	E
52	1	-710,65,-721,113	04/01/2014	15:32:47	5.93±0.12	183	3.0	12.5	3		
53	1	1101,-296,1136,-291	06/01/2014	07:42:35	9.48±0.22	420	1.5	8.4	1.5		

54	1	1115,220,1143,254	10/02/2014	21:00:57	8.33±0.07	408	1.3	3.2	3		
54	2	1118,55,1134,82	10/02/2014	21:01:06	7.46±0.1	400	4.2	8.0	3		
54	3	1062,110,1078,106	10/02/2014	21:02:02	2.32±0.05	238	1.0	0.9	3		
54	4	1108,29,1138,43	10/02/2014	20:58:27	3.77±0.13	355	7.5	3.0	2		
54	5	1076,-6,1091,1	10/02/2014	20:59:10	4.8±0.1	257	3.6	2.9	4.5	19.72±3.23	E,NE
55	1	1123,231,1143,244	10/02/2014	22:48:05	8.63±0.24	405	5.9	3.7	2.5		
55	2	1167,190,1203,192	10/02/2014	22:44:59	6.54±0.17	477	1.9	2.8	3		
56	1	1124,-8,1186,1	11/02/2014	13:28:08	9.07±0.14	403	9.3	7.8	4	20.71±4.71	E,NE
56	2	1068,-39,1130,-6	11/02/2014	13:28:13	11.88±0.13	314	17.8	27.6	5	19.62±2.96	E
56	3	1027,82,1043,54	11/02/2014	13:26:19	3.22±0.16	205	16.5	9.2	2.5		
56	4	1062,397,1122,348	11/02/2014	13:27:33	14.38±0.34	501	16.2	23.2	2		
56	5	1026,332,1004,354	11/02/2014	13:28:38	13.5±0.16	431	6.9	10.7	4.5	24.17±5.13	E
56	6	998,318,979,345	11/02/2014	13:28:49	7.59±0.2	392	3.6	3.8	2.5		
56	7	1068,427,1023,456	11/02/2014	13:31:32	14.16±0.55	457	4.9	15.0	3	13.64±3.93	E,NE
56	8	1015,384,990,419	11/02/2014	13:30:19	10.64±0.15	379	3.5	9.0	4		

Chapter 3

Coronal seismology with kink oscillations in the era of SDO/AIA

3.1 Introduction

In this Chapter the results of several studies are presented which utilise the examples of decaying kink oscillations detected and analysed in Chapter 2. This includes further analysis of the damping profiles, in Section 3.2, and then the application of the seismological inversion given in Section 1.4.3. This was initially performed with least squares fitting, in Section 3.3, and then extended with the use of Bayesian inference in Section 3.4. Finally, the results of the seismological inversion, for one loop, were compared to the results obtained by inferring the transverse density profile of the loop from the transverse intensity profile. This method of inferring the transverse density profile of coronal loops is extended to analyse a large sample of coronal loops in the next chapter.

3.2 Damping profiles of coronal loops

As presented in the previous chapter, strongly damped standing kink oscillations are frequently observed in coronal loops. The damping can be understood in terms of resonant absorption, via which the wave energy is converted from bulk transverse oscillations to localised, unresolved azimuthal Alfvén modes. The observed damping time should be dependent on the loops density structure, and theory predicts two possible damping profiles, as discussed in Sections 1.4.1 and 1.4.3, with the potential presence of both profiles and a switch time between them. This motivates more detailed analysis of the damping profiles observed in the catalogue of oscillations

presented in the previous chapter. Encouragingly, many of the observations were noted to appear non-exponential in nature, which will now be quantified.

3.2.1 Observations

Kink oscillation observations were selected from Table 2.2. A large number of events from the catalogue are unsuitable for this study. Detailed investigating of the damping requires the loop to be accurately tracked for several cycles once the oscillation begins, with a period of oscillation that remains relatively stable.

Time-distance maps for suitable events were created with the same SDO/AIA EUV 171Å data analysed in the previous chapter by taking linear slits with a 5 pixel width perpendicular to the oscillating loop and stacking the intensities along the slit, averaged over the width to increase the signal-to-noise ratio, in time. As a more careful analysis is required than in the previous study, one TD map selected by eye is no longer used. A series of 100 slits were created for each loop, perpendicular to an elliptical or linear fit of the loop axis, depending on loop orientation. An example of a linear fit is seen in the bottom left panel of Fig. 3.1, and the other three panels show elliptical fits. The displacement of the loop axis by the global standing kink mode is greatest at the loop apex and decreases to zero at the loop footpoints. Oscillations are therefore generally best measured near the loop apex, though the particular details of the event such as line of sight effects can make a measurement at the loop legs more suitable. The slit which maximised the clarity of the TD map and the apparent amplitude of the oscillation was then chosen by eye for further analysis. The active regions of four of the analysed loops, with the fits of the loops axis plotted and the slits chosen for the analysis overplotted are shown in Fig. 3.1.

Fig. 3.2 shows the TD maps for the selected oscillation events. From the TD maps, the location of the loop axis (symbols with error bars) is identified by fitting the intensity profiles of the vertical axis with a Gaussian profile. The fit is carried out within a window around the loop of interest to avoid contamination from other loops or bright features. The error for the loop centre position is determined separately for each data point, according to the error reported by the Gaussian fitting routine used. The damping behaviour of the kink oscillation is investigated by fitting exponential and Gaussian envelopes to the time-series of the loop position as described in the following section.

3.2.2 Damping profile analysis

Analysis is performed to determine which damping profile best describes the observed decay of the chosen kink oscillations. Two limiting cases were predicted by recent studies of resonant absorption, i.e a purely exponential damping profile and

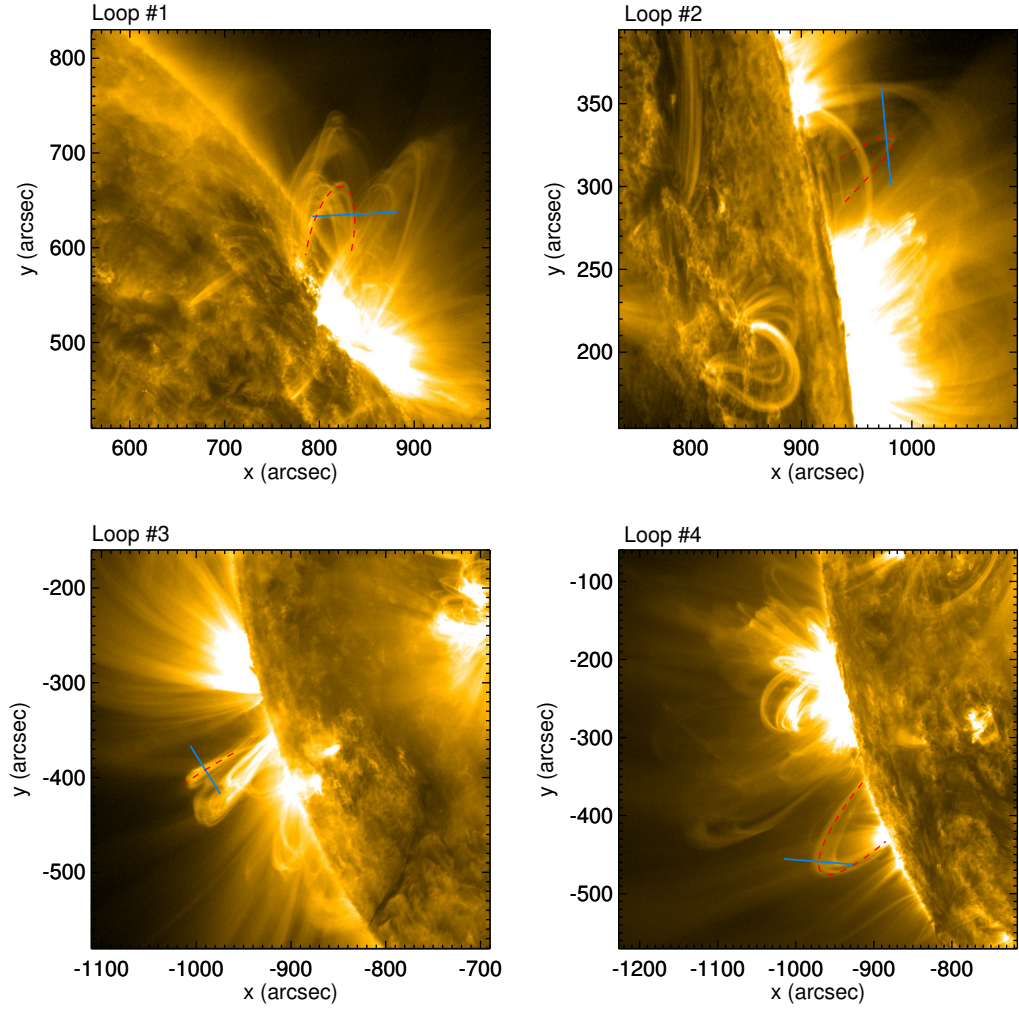


Figure 3.1: Four examples of the analysed coronal loops. The fit to the loop axis is given by the red dashed line and the blue line shows the position of the chosen slit. From left to right, top to bottom the loops are 43_4, 31_1, 32_1 and 40_10 (see Table. 2.2). The labels at the top of the plots number the loops for discussion in later sections of this chapter.

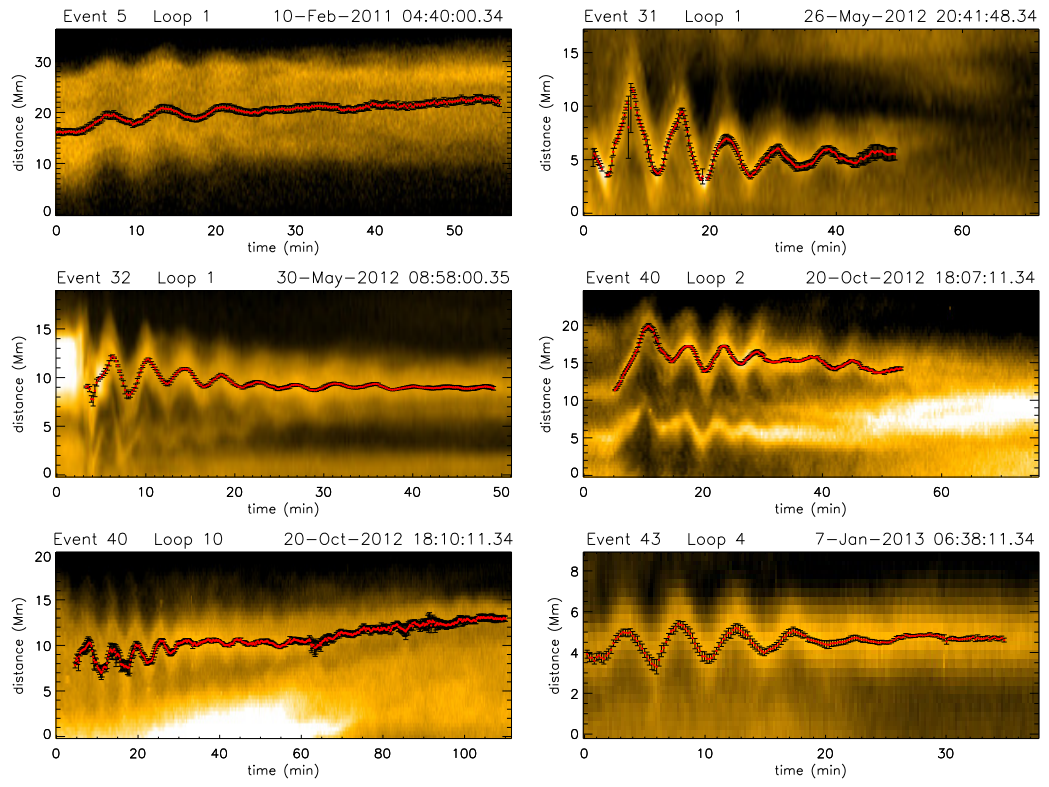


Figure 3.2: Time-distance maps for the 6 chosen kink oscillations for damping profile analysis. The slits used to produce four of them are shown in Fig. 3.1.

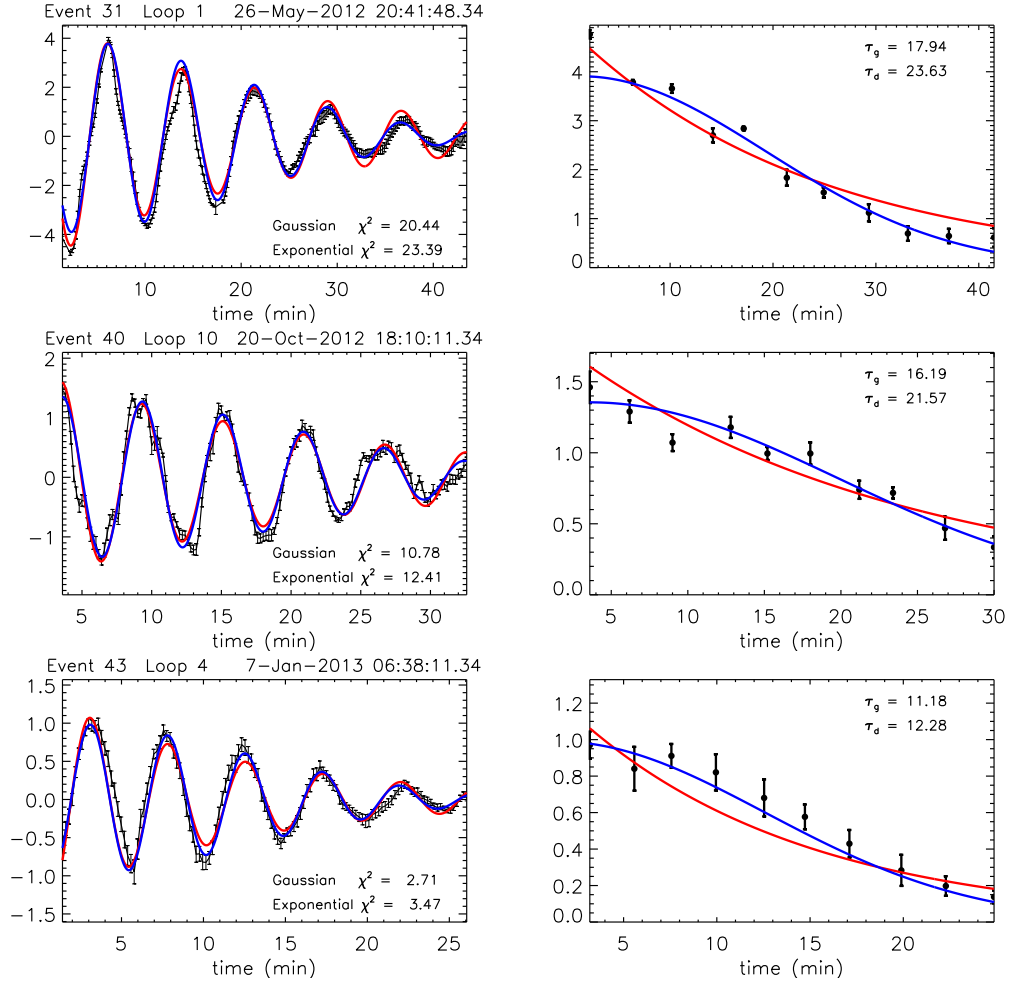


Figure 3.3: Kink oscillation observations where the damping profile is better fit by a Gaussian damping envelope than an exponential one. Left: the fitted position of the loop axis as a function of time, with the sinusoidal fits overplotted with Gaussian (blue lines) and exponential (red lines) damping envelopes. The χ^2 values are given for the two fits. Right: the absolute values of the extrema of the oscillations, with the same fitted damping envelopes overplotted and the Gaussian and exponential damping times given.

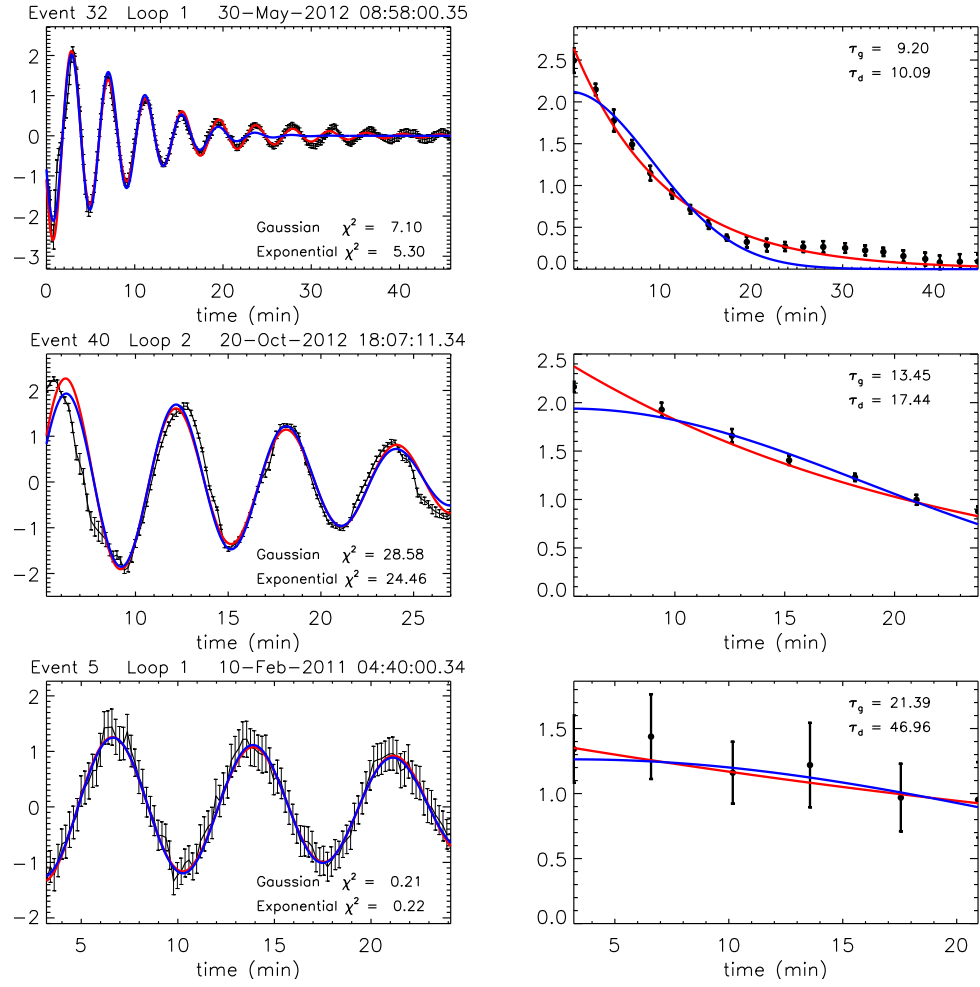


Figure 3.4: As for Fig. 3.3 but for two cases where exponential damping profiles were found to be favorable (top two panels) and one inconclusive case (bottom panel).

a purely Gaussian damping profile, ignoring the possibility of a transition between the two.

The data points for each kink oscillation were analysed by fitting the de-trended oscillations with damped sinusoidal oscillations of the form

$$A \sin(\omega t - \phi) \exp(-t^2/2\tau_g^2), \quad (3.1)$$

for the Gaussian damping profile, and

$$A \sin(\omega t - \phi) \exp(-t/\tau_d), \quad (3.2)$$

for the exponential damping profile. The parameters A , ω , ϕ , and τ were determined by a Levenberg-Marquardt least-squares fit with the data points weighted according to their errors, as described in Section. 1.7.2. Here the background trend is found by spline interpolation of the oscillation extrema, rather than including a polynomial term in the fitting function, as it was found to better deal with the observed background trends which vary with time. The accuracy of the two damping profiles is quantitatively compared by calculating the χ^2 values of the two fits. The fitted values of the damping times τ_g and τ_d are given in the figures.

Figure 3.3 shows examples of oscillations for which a Gaussian envelope is found to have a lower χ^2 than an exponential envelope. The Gaussian profiles are seen to describe the evolution of the oscillation more accurately, seen the right panels of Fig. 3.3. This is the clearest for the first few cycles of the oscillation, which is where the Gaussian and exponential profiles differ the greatest. For comparison with these examples, Fig. 3.4 shows oscillations for which an exponential damping envelope was found to give a better fit than a Gaussian envelope, and an inconclusive case.

3.2.3 Discussion and conclusion

The Gaussian and exponential damping envelopes considered are both consistent with damping due to resonant absorption, however distinguishing between them for a given oscillation can provide seismological information about the transverse density structure of the oscillating loop. It is demonstrated that in the majority of the selected cases the Gaussian profile is as good as or better than an exponential profile, which until now has typically been used to analyse observations.

Kink oscillations with a high signal quality were selected, which effectively means cases with weak damping were selected. As presented in Section 1.4.3, resonant absorption of the kink mode is weak if the density contrast and/or the inhomogeneous layer width are small. It should be noted some bias of the results due the oscillations chosen is possible.

The use of exponential and Gaussian damping profiles in this study was motivated by recent theoretical studies of kink oscillation damping via resonant absorption. However, other mechanisms are capable of producing a non-exponential damping profile, such as the non-linear effects discussed in Section 1.4.4 which may cause the physical characteristics of the loop to evolve during the oscillations. A search for signatures of these effects should be performed, especially when considering the potential scaling of the damping with amplitude presented in the previous chapter.

3.3 Coronal seismology based on resonant absorption

In this section follow up work to the damping profiles study discussed above is summarised. The seismological inversion shown in Section 1.4.3 for the generalised damping profile (Gaussian with a switch to exponential after a certain time) was applied to three of the loops, 43_4(loop 1), 31_1(loop2) and 32_1(loop3). The loops are shown in Fig. 3.1. The fitting of the damping profile is updated to include the switch between the Gaussian and exponential regimes, as the aim is to determine the time at which this switch occurs, t_s , as it provides seismological information which makes the seismological inversion well posed. These fits are shown in Fig. 3.5 by the green curves. For comparison fits with purely Gaussian (blue) and exponential (red) damping profiles are plotted. In the left panels the fitted switch time (t_s) is represented by the dashed line.

In Fig. 3.6 the seismologically determined values of ϵ (the width of the inhomogeneous layer) and ρ_0/ρ_e (the density contrast) and their uncertainties are plotted as the red points. In addition the inversion curves and their uncertainties are plotted, which would be obtained if only exponential damping is considered. The corresponding density profiles, and the resulting EUV LOS intensity are plotted in the right hand panels, discussed below. The full set of seismologically estimated values are given in Table 3.1. One drawback of this approach is that the absolute value of the density needs to be estimated for the Alfvén speed and therefore the magnetic field to be obtained. However the density contrast no longer needs to be estimated, which reduces the number of free parameters in the inversion performed based on the fitted parameters.

In Fig. 3.7 the seismologically determined density profiles are forward modelled to the corresponding intensity for comparison to the observed intensity profile. This is done by constructing the 2D density cross-section of the loop based on the obtained density profile parameters, assuming it is perfectly circular. The density squared is then integrated in one spatial direction to obtain an estimate for the LOS intensity profile. The intensity from the predicted density profile is added to the

fitted background trend and overplotted on the actual data points. Considering the isothermal and cylindrically symmetric approximations made there is relatively good agreement between the two intensity profiles, which is encouraging in the context of the seismology performed.

Table 3.1: Seismologically determined loop parameters.

Loop no.	ρ_0/ρ_e	ϵ	R (Mm)	l (Mm)	C_k (Mm/s)	C_{A0} (Mm/s)	C_{Ae} (Mm/s)	B_0 (G)
Loop #1	1.69 ± 0.56	1.17 ± 0.39	1.54 ± 0.13	1.80 ± 0.62	1.56 ± 0.22	1.40 ± 0.30	1.82 ± 0.49	9.38 ± 2.56
Loop #2	1.87 ± 0.17	0.81 ± 0.07	2.59 ± 0.64	2.10 ± 0.56	0.71 ± 0.14	0.62 ± 0.12	0.85 ± 0.17	4.37 ± 0.88
Loop #3	5.25 ± 0.58	0.28 ± 0.04	3.34 ± 0.34	0.94 ± 0.15	1.87 ± 0.25	1.44 ± 0.21	3.30 ± 0.51	17.06 ± 2.63

3.4 Coronal Seismology using Bayesian inference

The seismological study presented in the last section was updated to employ the Bayesian inference and model comparison approaches discussed in Sections 1.7.3 and 1.7.4. This allowed additional parameters to be included in the fitted model, and their relevance in interpreting the data to be tested. This approach is also used in the next section as well as the next chapter.

The seismological analysis was updated to include additional physical effects. In particular the analysis was modified to describe a time-dependent period of oscillation, additional longitudinal harmonics of the kink mode, and the decayless regime of kink oscillations, which as described in the introduction, can be detected in many coronal loops. The procedure for describing the background trend is also updated. The method is based on spline interpolation and is better at describing the dynamical background behaviour exhibited in these observations. The new method is built directly into the model function, as opposed to the detrending made prior to the fitting in Section 3.3. Bayesian analysis and MCMC sampling are used to investigate the dependence of results on model parameters and perform quantitative model comparison.

In Fig. 3.8 the oscillation for loop 1 is shown, with the different panels showing different aspects of the analysis. It is described in detail in the figure caption. In the top left panel the data and most credible model and its confidence interval are plotted. It can be seen that the model describes the observational data well. The wavelet plot in the top right panel and the detrended time series in the middle left show that the contribution of the additional longitudinal harmonics (up to the third) predicted by the model is not significant for this particular loop, however in the corresponding paper [Pascoe et al., 2017a] cases with more significant amplitude in the higher harmonics are presented. The major result of this work is presented in the middle right panel. These two density structure parameters are uniquely determined for the first time seismologically. The red error bars represent the 95% credible intervals determined from the histograms below.

The Bayes factor used in this work compares how well a particular model describes the data considering the whole explored parameter space, whereas a goodness of fit test, for example χ^2 , compares only the best fits. This was a limitation of the work presented in Section 3.2. Morton & Moorooogen [2016] apply an alternative approach to loop oscillation model comparison using the Kolmogorov–Smirnov test, for some of the same oscillation events.

For loop 1, the favoured model was one including the additional longitudinal harmonics but without dispersion (i.e the period ratios are fixed to integer values). This gave estimates of $\epsilon = 1.15^{+0.72}_{-0.35}$ and $\rho_0/\rho_e = 1.71^{+0.22}_{-0.19}$, in agreement with the values obtained in the previous section (see Table 3.1). For loop 2 the same model

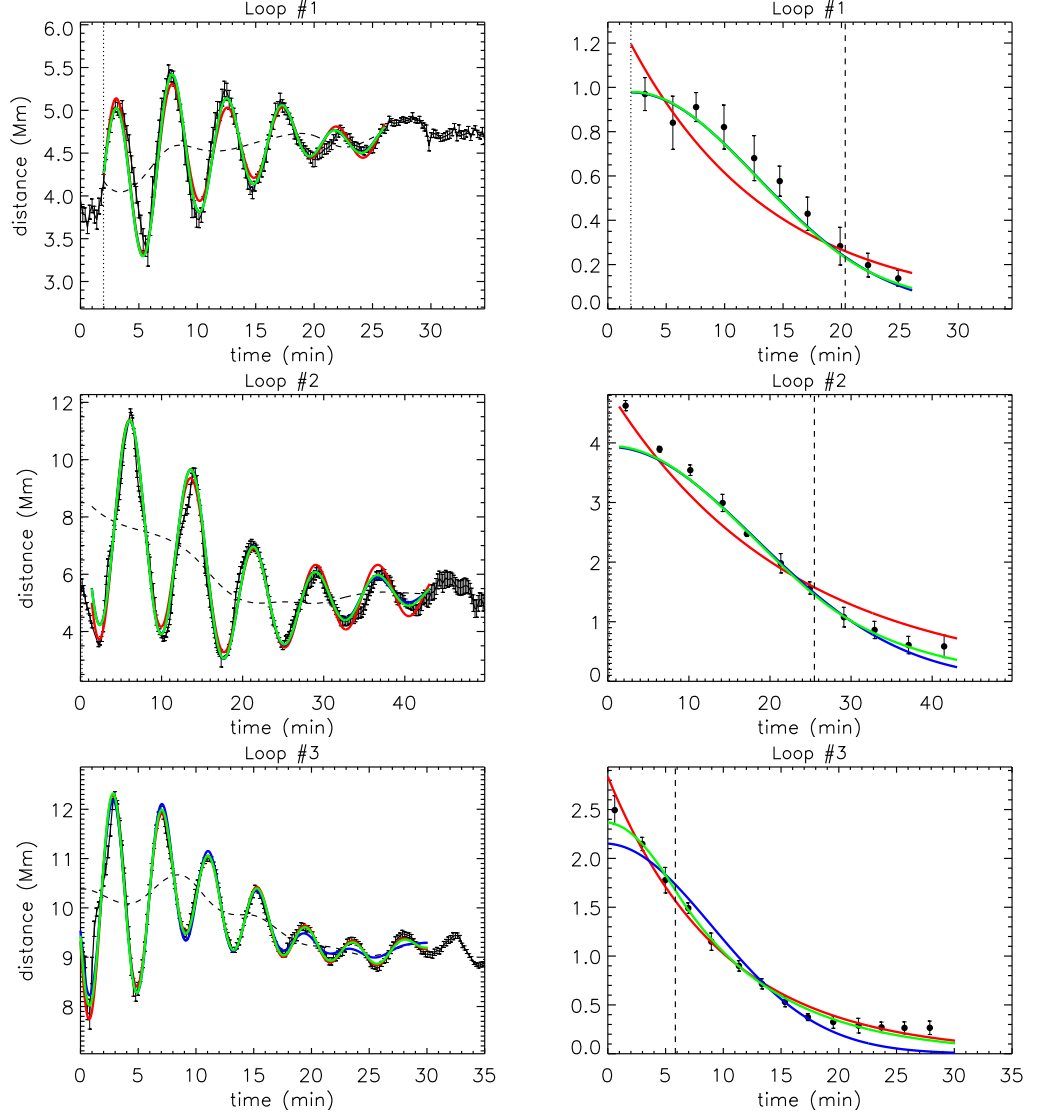


Figure 3.5: Left: least-squares fits of the time series of the fitted loop centre position. In blue is the fit with a purely Gaussian envelope, in red with a purely exponential envelope and in green the generalised damping profile which includes both regimes. The dashed line corresponds to the fitted background trend and the dashed-dotted line marks the start of the oscillation. Right: the extrema of the oscillations detrended using the fitted background trend. The colour scheme for the fits is the same as for the left panel. The dashed lines denotes the fitted value of t_s , the time of the switch between the Gaussian and exponential damping profiles.

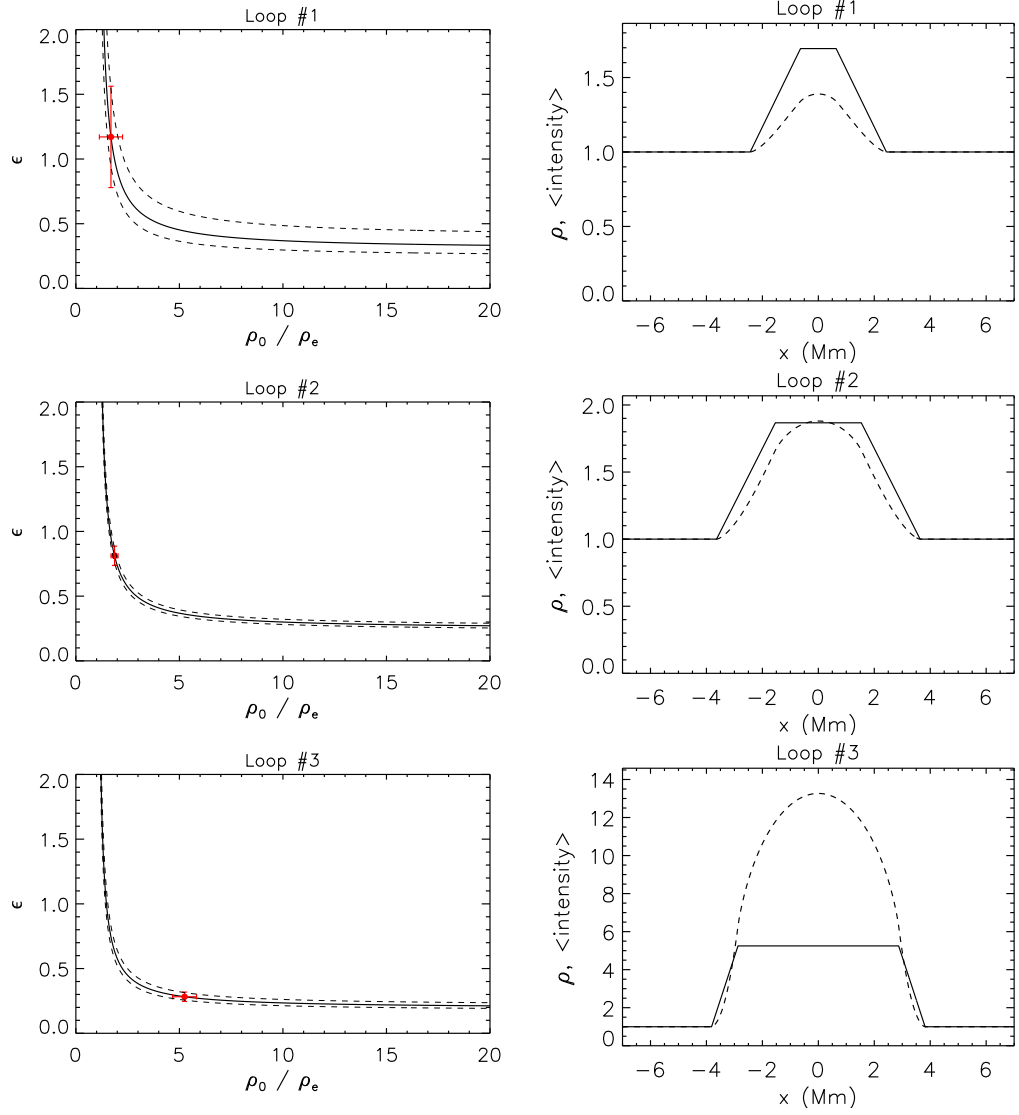


Figure 3.6: Left: seismologically determined values of ϵ and ρ_0/ρ_e and their uncertainties (red points). The solid line corresponds to the inversion curve obtained by using the exponential damping time alone, and the dashed lines correspond to the error bars. Right: density profiles for the transverse density structure obtained seismologically. The corresponding LOS intensity for that density profile is shown by the dashed curves.

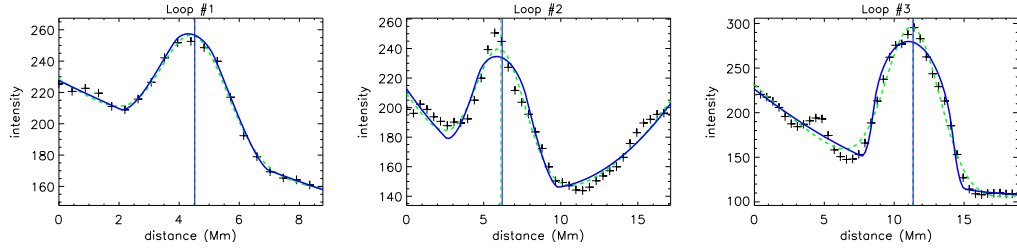


Figure 3.7: The seismologically determined transverse structure of the coronal loops forward modelled to the corresponding EUV emission (blue). The observed transverse intensity profile is given by the crosses. The green dashed curves correspond to a Gaussian fit to the intensity profile.

was favoured, giving $\epsilon = 0.70^{+0.21}_{-0.15}$ and $\rho_0/\rho_e = 1.93^{+0.24}_{-0.18}$. For loop 3 the model with a decayless component and the effect of stratification on the period ratios was favoured. From this values of $\epsilon = 0.42^{+0.18}_{-0.16}$ and $\rho_0/\rho_e = 3.49^{+6.61}_{-0.90}$ were obtained, which are significantly different from those found in the previous section. These differences in the obtained transverse density structure of the three loops analysed could be due to differences in their respective formation process within the active regions, or differences in their evolution over time prior to being observed.

The improvements to the physical model combined with the use of Bayesian inference and MCMC produces improved estimates of model parameters and their uncertainties. By allowing the period of oscillation to vary in time the time series used for analysis in Section 3.3 can be extended. The consideration of additional longitudinal harmonics aimed to account for the non-harmonic shapes of some of the oscillations. It can also provide additional seismological information from the ratios these periods, as described in Section 1.4.3. Here the effects of density stratification and loop expansion are also considered, which were not included in the previous analysis. The results of the model comparison show a lack of evidence for interpreting these period ratios in terms of either of these effects however. The exception is for Loop #3 (not shown here), for which there was very strong evidence for the stratified model, or any other model which describes $P_1/nP_n < 1$.

3.5 Coronal loop density profile inference

In the work briefly summarised in the above two sections, the transverse density structuring of coronal loops was calculated for the first time using the general damping profile for kink oscillations, with both least-squares fitting and Bayesian inference. The seismological method used assumes the density profile of the coronal loop has a linear transition between the interior and exterior density. How well this density profile accounts for the observed intensity profile of the loop will now be considered, and how the transverse intensity profile may be used in conjunction

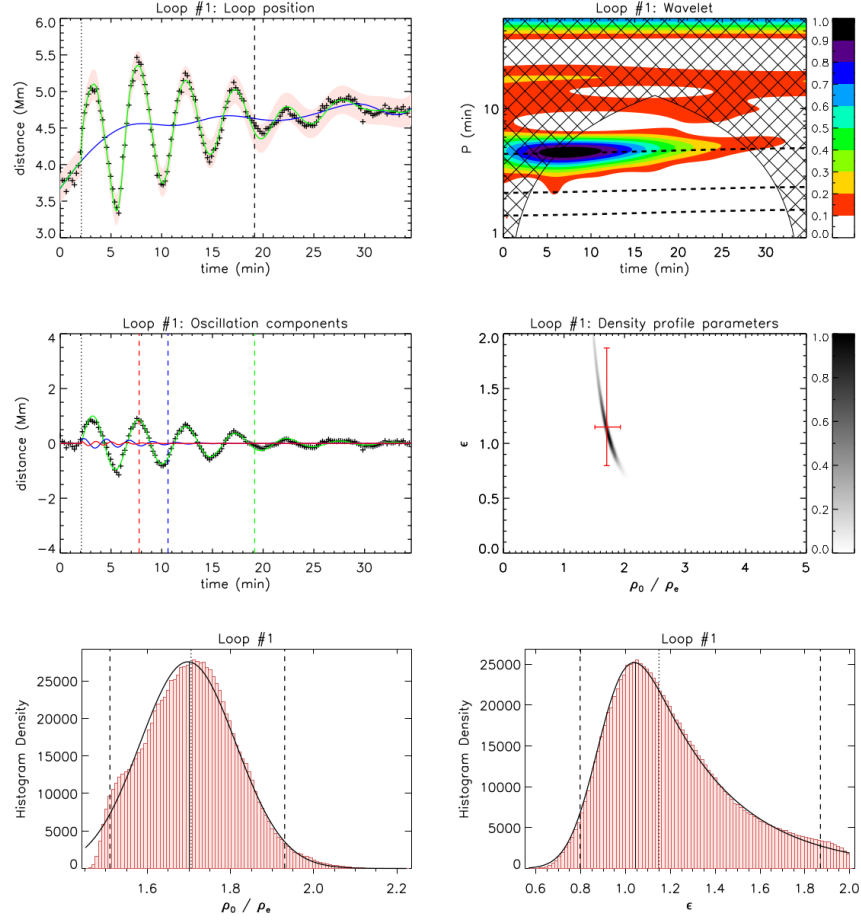


Figure 3.8: Analysis for Loop #1 using the oscillation model without dispersion. Top left: the fitted loop position time series (points) and the most credible model as determined by the Bayesian inference (green line), which includes the background trend determined by spline fitting (blue line). The red shaded region shows the 99% credible intervals for the loop position predicted by the model, including fitted noise σ_Y . The dotted and dashed lines show the start of the oscillation, and the switch time of the first harmonic respectively. Top right: wavelet spectrum of the loop position time series with colours representing the normalised spectral amplitude. The three dashed lines show the periods of oscillation in the model, determined by the Bayesian inference. Middle left: detrended loop position (symbols) with the first (green), second (blue), and third (red) longitudinal harmonics. Damping profile switch times for these harmonics are plotted as the dashed lines in the same colour. Middle right: the posterior 2D histogram of the transverse density profile parameters, determined from the oscillation damping envelope. The red bars are based on the median values and the 95% credible intervals, shown in the histograms below. Bottom panels: the posterior histograms for the two density profile parameters, the solid curves are fits using the exponentially modified Gaussian function. The dashed lines are the 95% credible intervals, used to produce the error bars in the 2D histogram above. The dotted lines are the median values.

with the seismological techniques as well as test them.

The relationship between the density profile of a coronal loop and its appearance in EUV images such as those produced by SDO/AIA is complicated and has motivated numerous studies [e.g. [De Moortel & Bradshaw, 2008](#); [Owen et al., 2009](#); [Taroyan & Bradshaw, 2014](#); [Yuan & Van Doorselaere, 2016](#)]. Some of the inherent difficulties were discussed in Section 1.7.1. The emission by plasma at a particular EUV wavelength depends on the density and temperature of the plasma and may include contributions from multiple spectral lines. Additionally, since coronal plasma is optically thin, multiple structures along the LOS of the observations will appear superimposed. The final observed signal also depends on properties of the imaging instrument. A detailed general introduction to the transverse density profile of coronal loops is given in the next chapter, in Section 4.1.

3.5.1 Density profile inference

In this section the process for obtaining the transverse density profile parameters from the observed transverse intensity profile is detailed, in contrast to the seismology using the damping of the oscillations in the previous sections. Isothermal and optically transparent approximations are made, therefore the intensity of EUV emission is proportional to the square of the plasma density integrated along the line of sight. The loop is also assumed to be stationary during the exposure of each frame. These assumptions were applied in Section 3.3 to compare the seismologically determined density profile to the observed intensity profile. Four different models for the transverse density profile are considered. The generalised Epstein profile, the step function, the linear transition region profile, and a Gaussian profile. Bayesian analysis, as described in Section 1.7.3 and 1.7.4 is used for comparison of the different density profile models.

In general, coronal loops are described as overdense, i.e they have an internal density ρ_0 , which is greater than the external density ρ_e . The minor radius is R . The step function profile (Model S), is the simplest model of the coronal loop density profile. The original analytical study of magnetohydrodynamic waves in a cylindrical loop was performed with this transverse profile [Edwin & Roberts \[1983\]](#). For a loop with a cylindrically symmetric cross-section and radial coordinate r , the transverse density profile for model S is given by

$$\rho(r) = \begin{cases} A, & |r| \leq R \\ 0, & |r| > R \end{cases}, \quad (3.3)$$

where $A = \rho_0 - \rho_e$ is the loop density enhancement.

The generalised symmetric Epstein profile (Model *E*) is defined as

$$\rho(r) = A \operatorname{sech}^2 \left(\frac{|r|}{R} \right)^p, \quad (3.4)$$

which describes a smooth profile with a steepness determined by the parameter p .

The linear transition layer profile (Model *L*) is given by

$$\rho(r) = \begin{cases} A, & |r| \leq r_1 \\ A \left(1 - \frac{r-r_1}{r_2-r_1} \right), & r_1 < |r| \leq r_2, \\ 0, & |r| > r_2 \end{cases} \quad (3.5)$$

where $r_1 = R(1 - \epsilon/2)$, $r_2 = R(1 + \epsilon/2)$, and $\epsilon = l/R$ is the transition layer width l normalised to R and defined to be in the range $\epsilon \in [0, 2]$. The use of the linear transition layer profile in seismology is motivated by the availability of the full analytical solution for the general damping envelope [Hood et al., 2013], and used in the previous sections.

A Gaussian density profile (Model *G*) [e.g. Aschwanden et al., 2007] is also considered, given by

$$\rho(r) = A \exp \left(-\frac{r^2}{2R^2} \right). \quad (3.6)$$

Examples of the four model profiles are given in the right panel of Fig. 3.9, with the magnitude of all parameters (A , R , p , ϵ) taken to be unity. The effect of the instrumental point spread function (PSF) is included for the AIA channel used, which effectively applies a Gaussian blur to the data, and the response function can be ignored due to the isothermal approximation.

Loop 3 was chosen for this analysis as it has the largest radius, $R \approx 4$ Mm, of the coronal loops for which seismology was performed in the work briefly presented in the last two sections. The selected loops transverse intensity profile consists of 44 data points, and the 2D density profile is calculated at ten times that resolution as convergence tests indicated consistent results for multiplication factors of ≥ 7 . The model intensity profile is then interpolated onto the original transverse coordinates and compared with the observational data D using the Bayesian inference and MCMC methods. Calculating the Bayes factor B_{ij} allows quantitative comparison of the four density profile models, as described in Section 1.7.3 using the given evidence thresholds.

3.5.2 Results

The seismologically determined density profile parameters for the loop of interest calculated in the work summarised in Section 3.4 are $\rho_0/\rho_e = 2.96_{-0.66}^{+1.00}$ and $\epsilon = 0.49_{-0.12}^{+0.23}$, where the parameter ranges correspond to the 95% credible intervals.

Each intensity profile is analysed using the four models. The loop contrast as well as the apparent loop radius improve towards the loop top, therefore the analysed slits are also close to the loop top. Fig. 3.10 and Table 3.2 summarise the results for one particular slit (slit 10). The left panel of Fig. 3.10 shows the observational intensity profile (symbols) and the profile for Model L (blue line). The shaded region is the 95% confidence interval for the model. The right panel shows the loop density profiles (using median values of sampled parameters) for each of the four models and indicates that models E and L produce very similar results.

The top two panels of Fig. 3.11 show the dependence of ϵ and R with height for Model L . The loop is found to expand with height, and ϵ remains approximately consistent with the seismological estimate (dotted lines). The value of ϵ inferred from the intensity profile is less well constrained than the seismological estimate. The right panel shows the Bayes factors calculated for model comparison. For lower slits (with smaller R) there is no statistical evidence to prefer Model L or E over Model S , indicating the effects of LOS integration over a circular cross-section and the PSF are sufficient to account for the smoothness of the loop intensity profile. However, the evidence in favour of the two profiles with transition layers greatly increases over the step function for higher slits surpassing the requirements for “strong” ($K_{ij} > 6$) and “very strong” ($K_{ij} > 10$) evidence. This can be understood as the loop expansion resulting in an effective higher resolution to resolve the inhomogeneous layer as the slits move up the loop axis. For this data, there is no statistical evidence to distinguish between Models L and E ($|K_{EL}| \lesssim 2$), consistent with these models producing very similar results. Models L , E , and S all have very strong evidence over Model G . For this loop a density model with a transition region (L or E) provides a better account of the intensity profile than a profile without a transition region (S). On the other hand, the transition region is sufficiently localised that there is greater statistical evidence for Model S than the fully inhomogeneous case of Model G .

3.5.3 Discussion and conclusion

The two transverse density profiles with finite transition layers are found to be preferable to the step function profile, which supports the interpretation of kink mode damping being due to mode coupling. The estimate of the transition layer width using forward modelling is consistent with the seismological estimate.

For wide loops, that is those observed with sufficiently high spatial resolution, this method can provide an independent estimate of density profile parameters for comparison with seismological estimates. In the ill-posed case of only one of the Gaussian or exponential damping regimes being observed, it may provide additional information to allow a seismological inversion to be performed. Alternatively, it may

Table 3.2: Inferred parameters for the density profile models M_i for slit 10.

M_i	A	x_0 (Mm)	R (Mm)	ϵ, p	K_{iS}	K_{iG}
L	$0.72^{+0.04}_{-0.04}$	$11.5^{+0.1}_{-0.1}$	$4.51^{+0.12}_{-0.13}$	$0.59^{+0.14}_{-0.15}$	20.6	46.3
E	$0.72^{+0.04}_{-0.04}$	$11.5^{+0.1}_{-0.1}$	$4.68^{+0.13}_{-0.13}$	$3.85^{+1.69}_{-0.94}$	19.6	45.3
S	$0.66^{+0.04}_{-0.04}$	$11.5^{+0.1}_{-0.1}$	$4.47^{+0.15}_{-0.15}$	—	—	25.6
G	$1.06^{+0.14}_{-0.11}$	$11.7^{+0.3}_{-0.3}$	$3.68^{+0.59}_{-0.45}$	—	−25.6	—

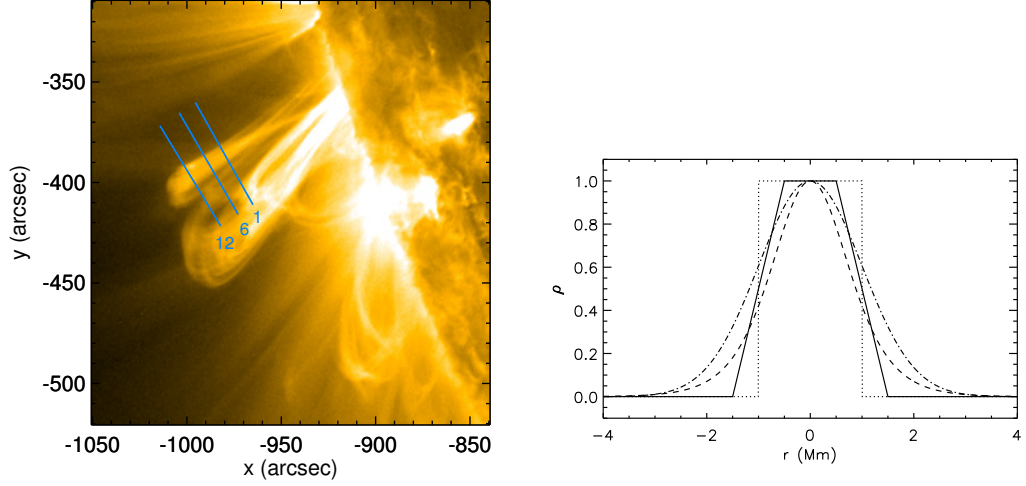


Figure 3.9: Left: SDO/AIA 171Å image of the analysed loop, observed at 08:58:00 UT on 30 May 2012. The blue lines indicate the locations of the slits used to generate transverse intensity profiles. Right: arbitrary transverse density profiles for the four models. These are; Model S (dotted), Model L (solid), Model G (dashed) and Model E (dashed-dotted).

be used to obtain structuring information for loops that do not oscillate, or to reveal any time-dependent variations in the cross-sectional profile which may be associated with non-linear effects, potential evidence for which was presented in Section 2.4. In the next chapter this method is applied to a large sample of coronal loops, aiming to establish what transverse density profile parameters are typically obtained and which density profile model is the most applicable.

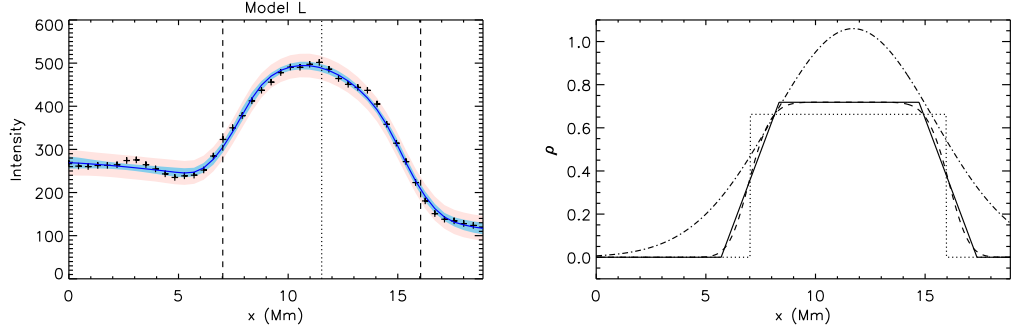


Figure 3.10: Left: SDO/AIA 171Å EUV intensity (points) across the loop described by Model L (blue line) which includes a background trend described by a second order polynomial. The shaded regions represent the 99% confidence intervals for the intensity predicted by the model, with (red) and without (blue) modelled noise. The vertical dotted and dashed lines denote x_0 and $x_0 \pm R$, respectively. Right: the inferred loop density profiles for Models L (solid), E (dashed), S (dotted), and G (dash-dot).

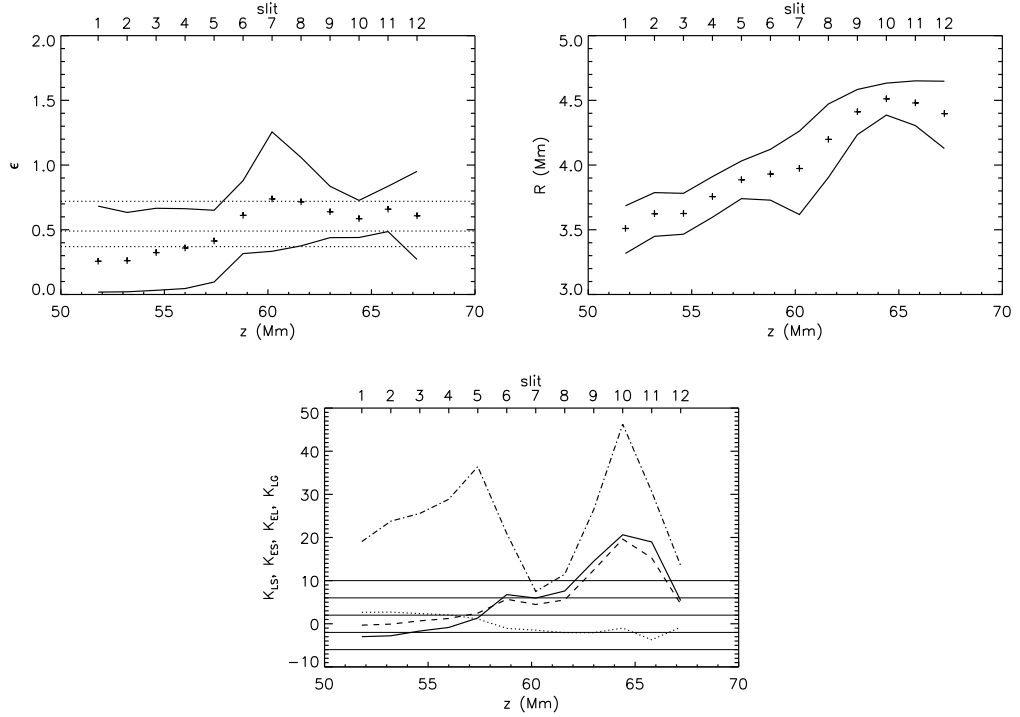


Figure 3.11: Top: normalised layer width ϵ (left) and loop radius R (right) estimated by forward modelling, as a function of length along the loop. The symbols show the median values while the solid curves denote the 95% credible interval. The horizontal dotted lines correspond to the seismologically estimated values. Bottom: the Bayes factors K_{LS} (solid), K_{ES} (dashed), K_{EL} (dotted), and K_{LG} (dash-dot) as a function of length along the loop.

Chapter 4

The transverse density structure of coronal waveguides

4.1 Introduction

In this chapter a statistical study of inferred transverse density profiles of coronal loops is performed using EUV imaging data from SDO/AIA. 233 coronal loops are analysed, observed during 2015 and 2016. Three models for the density profile are considered; the step function (Model *S*), the linear transition region profile (Model *L*), and a Gaussian profile (Model *G*). Bayesian inference is used to compare the three corresponding forward modelled intensity profiles for each loop.

The solar corona is highly structured, due to the magnetic field that penetrates it from the lower atmosphere. The coronal plasma appears to fill in the magnetic flux tubes in certain locations, normally within active regions, forming the curved coronal loops and threads observed by EUV imagers. The precise nature of coronal loop formation, and their transverse and longitudinal structure is still debated, see Section 1.1.4. The transverse density structure of coronal loops is currently of high importance, as outlined in Section 1.4.1 and 1.4.3, and this discussion is extended below.

There have been multiple studies of the transverse structure of coronal loops with each generation of EUV imagers [e.g. [Bray & Loughhead, 1985](#); [Aschwanden & Nightingale, 2005](#); [Aschwanden & Boerner, 2011](#); [Peter et al., 2013](#)]. The majority of such studies note that the transverse intensity profile of the loops resembles a Gaussian peak, which is used to estimate the loop position, width and intensity contrast. To infer the density structure from these intensity profiles the relationship between the density profile of a coronal loop and its appearance in EUV images needs to be considered, some relevant discussion was given in Section 1.7.1. The emission in a particular spectral range in the EUV band depends on the plasma

density and temperature. Additionally, coronal plasma is optically thin and so multiple structures along the observational Line Of Sight (LOS) will be superimposed in the observations. Finally, the characteristics of the instrument should also be taken into account. Coronal loops are generally considered to consist of a core of uniform density with an inhomogeneous layer surrounding it where the density transitions from the internal to external value. Using TRACE data (see Section 1.6), [Aschwanden et al. \[2003\]](#) measured the thickness of the non-uniform layer for multiple loops based on a density profile with a sinusoidal transition layer and a uniform core, this density profile was capable of reproducing the observed intensity profile. [Aschwanden et al. \[2007\]](#) performed a large scale study of the transverse structure of loops, using intensity profiles based on step function and constantly varying density profiles.

The transverse structure of coronal loops can be determined from, and is integral to, the study of the oscillations they exhibit. Kink, or transverse, oscillations of coronal loops are one of the most intensively studied examples of MHD waves. These waves were introduced in detail in Section 1.4. Large scale statistical studies of kink oscillations have recently been performed (see [Zimovets & Nakariakov \[2015\]](#) and Chapter 2). This work led to the confirmation of the presence of non-exponential damping envelopes of some of the oscillations studied, which were further analysed in 3.2. This can be attributed to the damping profile proposed in [Pascoe et al. \[2012, 2013a\]](#), which has subsequently been used to perform seismology, including the use of Bayesian model comparison, presented in Sections 3.3 and 3.4. In Section 3.5 the result of this seismology was compared to density profiles estimated from the EUV intensity for one coronal loop.

The transverse density structure can also play an important role in understanding and detecting non-linear effects. In the studies mentioned in Section 1.4.4 the transverse structure is perturbed by the non-linear effects, which is of theoretical and observational significance. In Section 2.4 the study of kink oscillations of coronal loops showed a negative correlation between the quality factor of the oscillations and the amplitude, suggesting the presence of non-linear effects causing real or apparent additional damping. A similar dependence was found in a numerical study by [Magyar & Van Doorselaere \[2016a\]](#), in which non-linear mechanisms such as KHI were found to modify the damping of the kink mode significantly at large amplitudes.

The specific shape of the transverse non-uniformity is also responsible for the geometrical dispersion of the fast magnetoacoustic waves guided by the loop, which determines the specific shape of the quasi-periodic rapidly propagating wave trains, as explored in Section 1.5. These wave trains have recently been detected in the corona with the EUV imagers and the full realisation of their seismological

potential requires the knowledge of the transverse profile of the waveguiding plasma non-uniformity. Observational and numerical results relating to these waves will be discussed in the Chapter 5.

In understanding the mechanisms and effects discussed above, as well as the seismology which is based on them, it is important to understand the transverse and longitudinal loop structure, combining knowledge of the formation and structure of coronal loops and the oscillations they exhibit. In this chapter a sufficiently simplified forward modelling procedure is considered, allowing which transverse density profile has the most evidence for individual loops to be tested, based on the observed intensity profile using Bayesian inference. In addition, the most probable structuring parameters are obtained for each density model. This chapter is organised as follows; in Section 4.2 the observations and data are described, in Section 4.3 the forward modelling and model comparison methods are outlined, in Section 4.4 the results are presented, and the discussion and conclusions are given in Sections 4.5 and 4.6.

4.2 Observations

For this study any time dependent evolution of the loops is neglected. Therefore single AIA images at 171, 193 and 211 Å are used. One set of images was downloaded for each week between January 2015 and September 2016. Each image was plotted, and loops or threads which appeared monolithic and had a well contrasted segment were identified. This may be an individual thread (or strand), which is part of a larger loop bundle, as long as the width of the thread is sufficient for the cross-sectional structure to be resolved, which was determined subjectively by eye. Two points were selected by eye either side of the loop at a position which minimised background contamination from other structures and maximised the intensity contrast. The intensity was extracted along a line connecting these two points, and was averaged over a width of 5 pixels. The uncertainty and noise on these intensity profiles are considered to be unknown and were inferred during the analysis described below. This process resulted in 233 loops for further analysis.

The sample of loops is not unbiased as loops or threads with a sufficient width to be well resolved and which had no visible sub-structure were selected. Higher, or longer, coronal loops are under sampled, due to the increased noise and reduced intensity contrast making them unsuitable for analysis.

It was found that the correlation between the loops intensity profile at 171 Å and the other two wavelengths was low in general, implying that the structures studied are not generally multi-thermal over the temperatures sampled by the chosen AIA bands (which does not exclude them being multi-thermal within a nar-

rower temperature range, or threads with different peak temperatures that are not co-spatial). In general, it did not appear that the intensity profiles at 193 and 211 corresponded to the hotter outer layer counterpart of a cooler core seen in 171, which is often assumed to be the case in forward modelling [e.g. Magyar & Van Doorsse-laere, 2016b; Antolin et al., 2016]. For this reason the analysis is not extended to the other wavelengths, and this should be the subject of further study.

4.3 Method

4.3.1 Constructed intensity profiles

In this study three models for the transverse (cross-sectional) density profile of the coronal loops are considered; the step function profile, the transition layer profile, and the Gaussian profile, as described and motivated in Section 3.5, and given by equations 3.3 – 3.6. The generalised Epstein profile is not used as the two limits of this profile are well represented by the transition layer profile and the Gaussian profiles. In Section 3.5 it was found that the advantage of the Epstein profile, over the layer profile, as reflected in the Bayes factor, was negligible. Examples of the three model density profiles are given in the right hand panels of Fig. 4.1 for three of the analysed loops. The use of the isothermal approximation allows the intensity profile to be calculated as the square of the density integrated along the LOS (i.e over a cylindrical cross-section). The loop intensity profile is calculated numerically by constructing a 2D density profile for the radial profiles given in 3.3 – 3.6 with $r = \sqrt{(x - x_0)^2 + (y - y_0)^2}$, where x is the coordinate transverse to the loop, with the loop centre at x_0 , and y is the coordinate along the LOS.

In addition to the contribution from the loop the density profile also includes a background component which is described by a second order polynomial. This is included to model the emission from the background plasma and other structures along the LOS. The instrumental PSF is then simulated using a Gaussian kernel with $\sigma = 1.019$ pixels, corresponding to the 171Å SDO/AIA channel [Grigis et al., 2013]. The 2D density profile is constructed with 10 times the resolution of the observed intensity profile. The final model intensity profiles (L , G and S) are then interpolated onto the observational coordinates (after the above procedure has been applied) and compared with the observed intensity profile using the method outlined below.

4.3.2 Bayesian inference

The same model comparison procedure based on Bayesian inference and Markov chain Monte Carlo (MCMC) sampling is used, described in Section 1.7.3 and applied to a coronal loop intensity profile in Section 3.5.

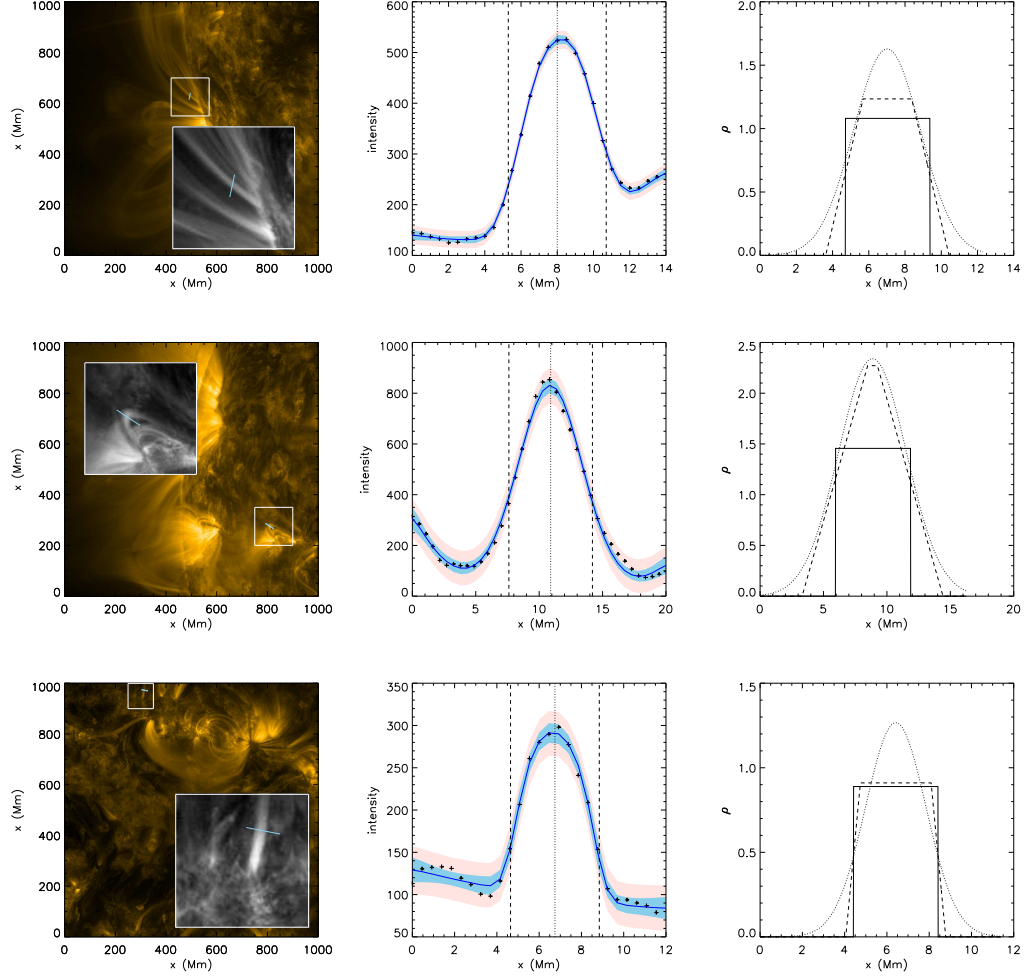


Figure 4.1: Examples of loops for which Models *L* (top), *G* (middle), and *S* (bottom) were found to best describe the data. Left: SDO/AIA 171 Å image of an analysed loop. The blue line indicates the location of the slits used to generate the transverse intensity profiles. The white box and inset show a magnified region around the loop. Middle: 171 Å EUV intensity profile (symbols) across the selected loop. Model *L*, *G* or *S* (blue line) is plotted, with the model values being the median values from the corresponding probability distributions. The shaded areas represent the 99% confidence region for the intensity predicted by the model, with (red) and without (blue) modelled noise. The vertical dotted and dashed lines denote x_0 and $x_0 \pm R$, respectively. Right: The inferred density profiles for Models *S* (solid), *L* (dashed) and *G* (dotted).

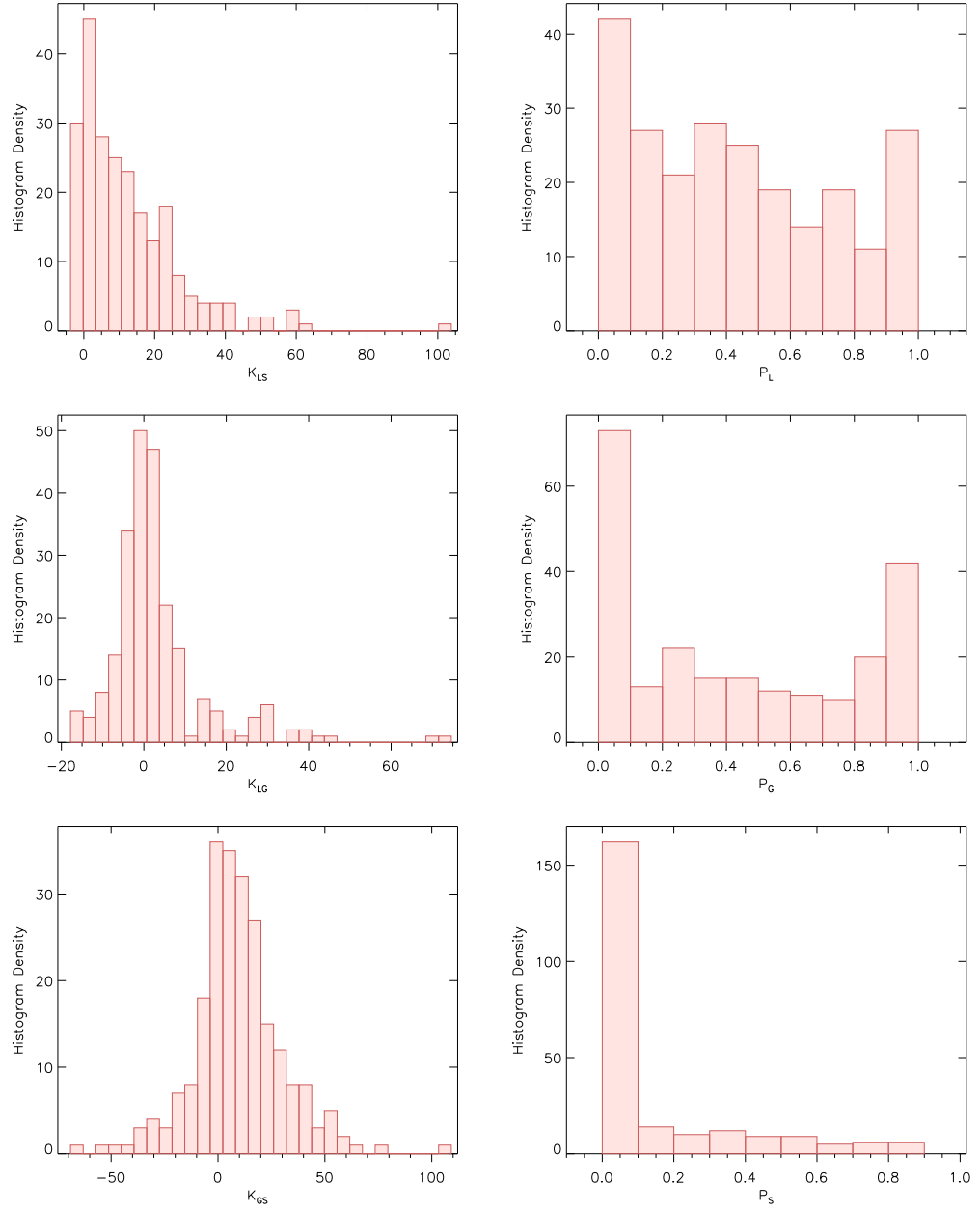


Figure 4.2: First column: histograms of the Bayes factor (K_{ij}) comparisons of Models L , G and S . Second column: histograms of the model probabilities (P_i) calculated from the evidence values for each model.

For this procedure priors need to be selected for each of the parameters. An initial least squares fit is performed on the intensity profiles using the forward modelled intensity profile from density profile L . This allows guess parameters to be obtained, allowing suitable limits on the priors to be obtained for the x position, radius and intensity contrast of the loop and the background polynomial. For the layer profile $0 \leq \epsilon \leq 2$ is prescribed according to the definition of the density profile. The prior probability distributions of all the above parameters are taken to be constant within the prescribed bounds.

Any two models M_i and M_j may be quantitatively compared using the Bayes factor, defined in Equation 1.55 as

$$B_{ij} = \frac{P(D|M_i)}{P(D|M_j)}, \quad (4.1)$$

where the evidences, $P(D|M)$ are calculated as described in Section 1.7.3. Evidence thresholds are defined with respect to the natural logarithm of this factor;

$$K_{ij} = 2 \ln B_{ij}, \quad (4.2)$$

where values of K_{ij} greater than 2, 6 and 10 correspond to “positive”, “strong”, and “very strong” evidence for model M_i over model M_j , respectively. Negative values indicate evidence for model M_j subject to the same thresholds. All permutations of the Bayes factor for Models S , L and G are considered.

For the purpose of prescribing which model is favoured for each intensity profile, and to what degree, the probability of a given model is defined using normalisation of the evidence values

$$P_i = \frac{E_i}{E_S + E_L + E_G}, \quad (4.3)$$

where P_i and E_i are the probability and evidence for a given model and E_S , E_L , and E_G are the evidence values for Models S , L and G as given by Equation 1.56.

To plot intensity profiles for the models, and plot the distributions of the parameters of interest, estimates and uncertainties for the model values are obtained by taking the median and 95th percentile of the posterior probability distributions for a given parameter.

4.4 Results

4.4.1 Model Comparisons

233 coronal loops were analysed using the method described in Section 4.3, obtaining Bayes factors, K_{ij} , and the probability of each model, P_i , for each loop. Three

examples are shown in Fig. 4.1. The top row shows a loop for which Model L was favoured. The corresponding Bayes factors and model probabilities are $K_{LS}=32.3$, $K_{LG}=26.6$, $K_{GS}=5.7$ and $P_L=1.00$, $P_G=0.00$, $P_S=0.00$. On the left the slit position is plotted in blue, with a close up of the loop inset. The middle panel is the intensity profile (symbols), and Model L (blue line), defined using the medians of the returned probability distributions for each parameter. The shaded regions correspond to the 99 % confidence levels for the intensity profile with and without the modelled noise (red and blue respectively). On the right the returned density profiles for Models S (solid), L (dashed) and G (dotted) are plotted.

The middle row shows a loop for which Model G was favoured. The corresponding Bayes factors and model probabilities are $K_{LS}=46.5$, $K_{LG}=-13.5$, $K_{GS}=60.0$ and $P_L=0.01$, $P_G=0.99$, $P_S=0.00$. The bottom row shows a loop for which Model S was favoured. The corresponding Bayes factors and model probabilities are $K_{LS}=-2.29$, $K_{LG}=16.5$, $K_{GS}=-18.4$ and $P_L=0.24$, $P_G=0.00$, $P_S=0.76$. It should be noted that this loop has the smallest minor radius, R , and therefore the lowest spatial information.

In the left column of Fig. 4.2 histograms of the Bayes factors K_{LS} , K_{GS} and K_{LG} are plotted. The values of K_{LS} are seen to be largely positive, indicating that Model L is almost always a better model for the density profile of the coronal loops analysed than Model S , subject to the assumptions made. The values of K_{GS} are more evenly distributed about zero, indicating that the use of Model G over Model S is not always justified, however there is strong evidence for it in many cases. Finally, the values of K_{LG} are also distributed about zero, with a slight bias to positive values, indicating many loops show strong evidence for either of the profiles over the other.

These results are better quantified by considering the evidence thresholds stated in Section 4.3. These are summarised in Table 4.1 for K_{LS} , K_{LG} and K_{GS} . Each permutation of the Bayes factor is included, with the main result being that in 47 % of cases there is very strong evidence for Model L over Model S and in 45 % of cases very strong evidence for Model G over S .

Thresholds can be used to determine which of the three models is favoured for each loop, and how strongly. In Table 4.2 percentages of loops falling into each evidence threshold for each model are listed. For a loop to be counted for a given model i and threshold, its Bayes factor for the comparison to the other two models, B_{ij} and B_{ik} must be greater than the threshold. In this case there is a competition between models, so only 5 % of loops have very strong evidence for Model L or G over both other respective models. The probabilities calculated for each model for each loop, P_i , can be summed to show how the evidence is distributed between the three models. These values are 101.5, 99.4 and 32.1 for Model L , G and S

Table 4.1: Percentages of coronal loop intensity profiles falling into three evidence thresholds for each permutation of the Bayes factor for Models L , G and S .

	$K_{ij} > 2$	$K_{ij} > 6$	$K_{ij} > 10$
K_{LS}	75 %	58 %	47 %
K_{SL}	4 %	0 %	0 %
K_{GS}	65 %	53 %	45 %
K_{SG}	25 %	25 %	12 %
K_{LG}	42 %	24 %	15 %
K_{GL}	32 %	12 %	5 %

Table 4.2: Rows 1–4: percentages of coronal loop intensity profiles falling into three evidence thresholds for each density model. For a loop to be counted for a given model and threshold it’s Bayes factor from comparison to both other models, K_{ij} and K_{ik} , must be greater than that threshold. Row 5: summed probability values (P_i) for each density model, showing how the evidence is distributed between the three models for the 233 analysed loops.

	L	G	S
>0	44 %	43 %	13 %
>2	25 %	32 %	4 %
>6	8 %	12 %	0 %
>10	5 %	5 %	0 %
$\sum P_i$	101.5	99.4	32.1

respectively, given in Table 4.2. This again shows the similarly strong evidence for Models L and G .

The right column of Fig. 4.2 shows histograms of P_L , P_G and P_S . The distributions of P_L and P_G show a significant number of cases where the respective probabilities are greater than 0.5, indicating that the corresponding density profile is the favoured model. The distribution of P_S shows that the step function density profile was unable to produce the observed intensity profile for the vast majority of cases.

4.4.2 Parameter dependencies

The left panel of Fig. 4.3 shows histograms of ϵ for Model L for the different thresholds of K_{LS} and K_{LG} given in Table 4.2 (red to orange), and with no threshold (grey). These values correspond to the median values from the probability distributions of the parameter. It can be clearly seen that adding the threshold removes the cases where Model G was favoured (corresponding to a higher ϵ for Model L), shifting the distribution to lower values. The cases where Model S was favoured are also removed for the higher thresholds, removing the lower values of ϵ . In the

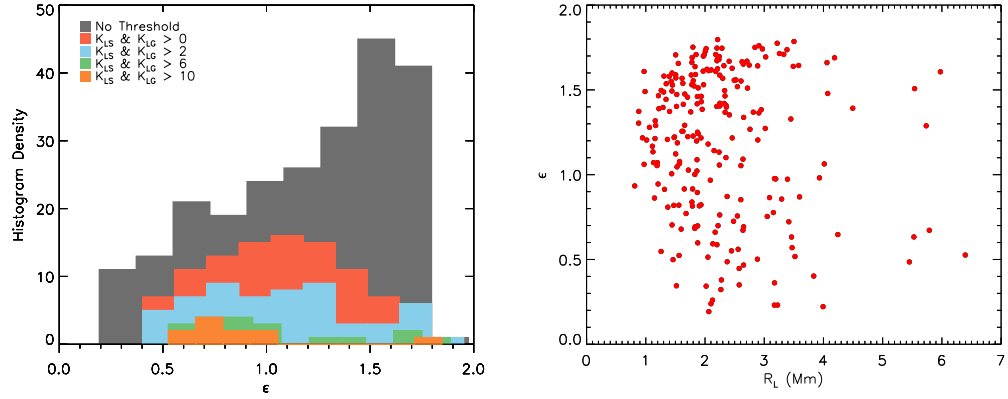


Figure 4.3: Left: histograms of the normalised layer width ϵ for the combined thresholds of K_{LS} and K_{LG} given in Tab. 4.1. Right: the normalised layer width, ϵ , plotted against the loop minor radius for Model L , R_L .

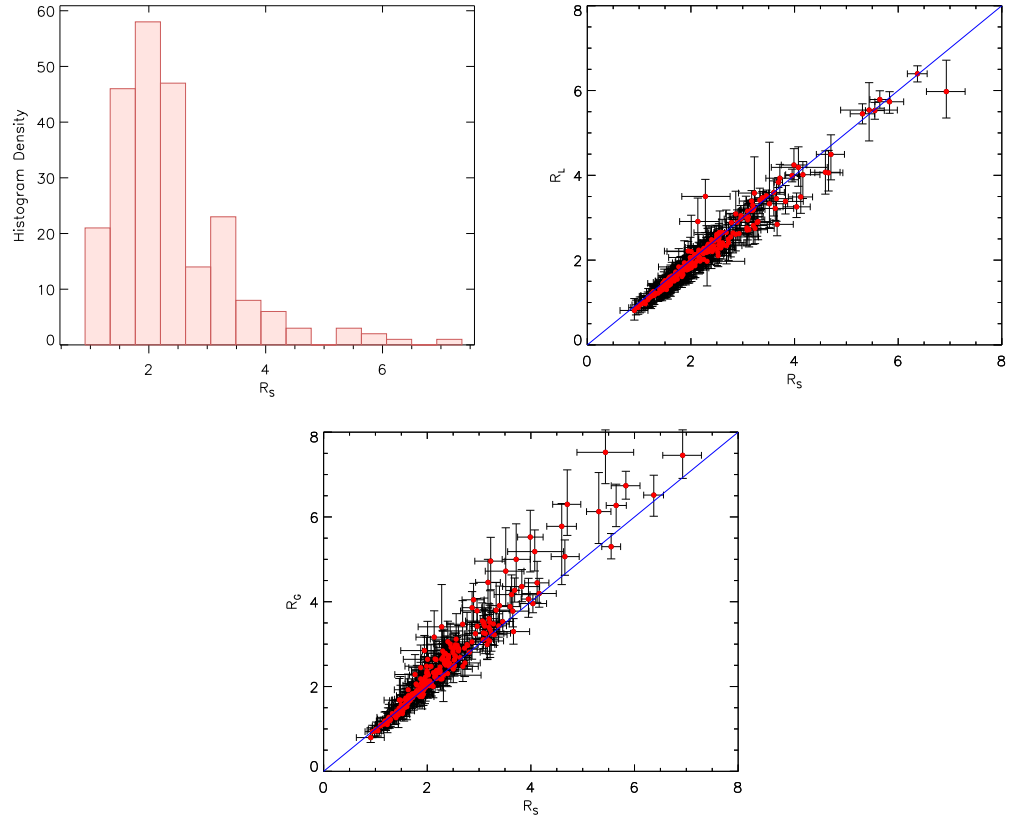


Figure 4.4: Comparison of the loop minor radius determined by the three models. Top left: distribution of the median radii from Model S , R_S . Top right: the loop radii from Model L , R_L , plotted against R_S . Bottom: The loop radii from Model G , R_G , plotted against R_S . The blue lines correspond to $R_L = R_S$ and $R_G = R_S$ respectively. The error bars correspond to the 95th percentile.

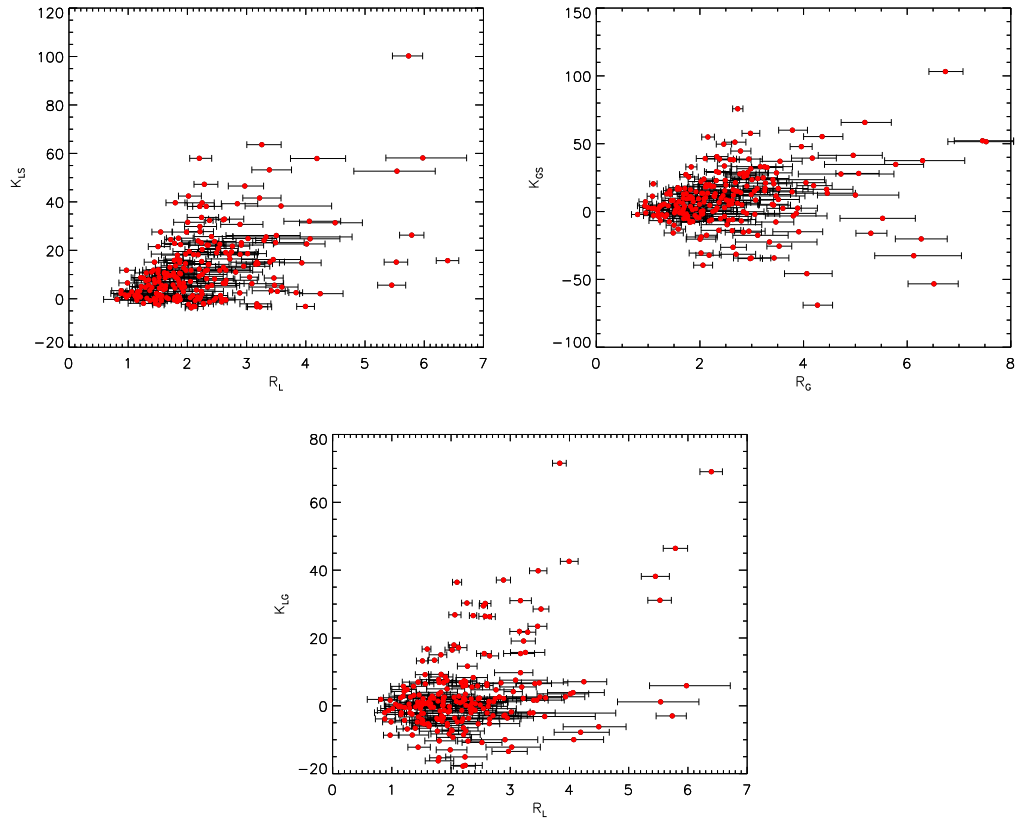


Figure 4.5: Top left: Bayes factor K_{LS} plotted against loop radius R_L . Top right: Bayes factor K_{GS} plotted against loop radius R_G . Bottom: Bayes factor K_{LG} plotted against loop radius R_L .

right panel of Fig. 4.3 ϵ is plotted against the radius for the layer model, R_L , and shows no correlation. The values of R_L also correspond to the median values of the probability distribution.

The top left panel of Fig. 4.4 shows the distribution of the radii for Model S , R_S . This shows that the sampled loops have radii peaking at 2 Mm with a number of cases with higher radii. The top right panel plots R_L against R_S , where the blue line corresponds to $R_L=R_S$ and the bottom panel plots R_G against R_S , where the blue line corresponds to $R_G=R_S$. This shows that despite the evidence values for the different models varying the radii for the different models remain within error. It can be seen that Model G slightly overestimates the radius compared to S and L .

In Fig. 4.5 K_{LS} , K_{GS} and K_{LG} are plotted against R_L , R_G and R_L respectively, showing that the spread of Bayes factors increases with loop radius due to the increased spatial information. It can also be noted that K_{LS} is largely positive, whereas K_{GS} is more evenly split between positive and negative values, but with higher values of both. K_{LG} is also more evenly split between positive and negative values, but with the highest evidence values for Model L (positive K_{LG}).

4.5 Discussion

The results show that in the majority of cases there is evidence for a density profile with an inhomogeneous layer, and in the majority of loops selected there is enough spatial information to constrain the size of the inhomogeneous layer, or note a continually varying profile being preferred. The existence of this inhomogeneous layer between the high density core and lower density background is a necessary condition for resonant absorption to occur. It is therefore crucial to the interpretation of transverse loop oscillations in terms of kink oscillations damped by the coupling to Alfvén waves inside the inhomogeneous layer, and hence the validity of any seismological calculations based on this interpretation, such as those discussed in Section 1.4.3 or presented in Chapter 3.

The three cases in Fig. 4.1 highlight how the different density profiles considered behave for different loops. For the case where Model L is favoured Model S sets the radius to occur halfway through the inhomogeneous layer and has a correspondingly reduced density contrast. Model G overestimates the width and height of the density profile to match the gradient in the layer of Model L . For the case where Model G is favoured Model L reproduces the profile well by minimising the size of the homogeneous core. For the case where Model S was favoured Model L matches the profile by minimising the size of the inhomogeneous layer. Model L tends to Model S in the limit $\epsilon \rightarrow 0$, and so for these cases the additional parameter, *i.e.* ϵ , is redundant and so model S is naturally preferred in terms of the Bayesian

evidence.

From the results it can be seen that despite Model G being favoured strongly in some cases Model L is the most general as it can reproduce both Model S and G satisfactorily, while providing additional information where there is evidence for an inhomogeneous layer and homogeneous core. This is encouraging for seismology being performed with Model L (as performed in Chapter 3), which is the only density profile for which the full analytical solutions are known for damping via resonant absorption [Hood et al., 2013]. However, the many cases in which there is evidence for very large transition layers (or Gaussian density profiles), the thin boundary approximation used would no longer hold. For finite inhomogeneous layers, the damping rate (for the exponential damping regime) is modified by up to 25 % in comparison with the thin boundary approximation [Van Doorselaere et al., 2004]. This may also have implications for the damping and dissipation of the Alfvén waves generated via the resonant absorption of kink fast magnetoacoustic waves (see Section 1.4.1). The transverse Alfvén speed profile associated with the density profile may vary both the energy dissipation rate and its spatial distribution [see discussion in Pagano & De Moortel, 2017].

The tables and histograms of the Bayes factors K_{ij} and probabilities P_i show that there are a similar number of cases where Model L or G are favoured over the other two, with many extending into the “very strong” evidence threshold. From the bottom panel of Fig. 4.2, it can be seen that P_L is evenly distributed compared to P_G , which is more confined to low and high values, reflecting the higher generality of Model L as discussed above.

From the histogram of ϵ the distribution without a threshold (grey) shows that the loops analysed generally have large or continuous inhomogeneous layers (where Model G was favoured), in contrast to the typically small boundary layers considered in numerical modelling. For the first two thresholds the distribution then centres around $l = R$. In Magyar & Van Doorselaere [2016a] it was shown that for thick boundary layers ($\epsilon > 0.5$) there is little or no effect on the exponential damping time at higher amplitudes. However for smaller layers ($\epsilon < 0.5$) the amplitude can have a strong effect on the observed damping time. The results indicate that the loops have inhomogeneous layers which fall on both sides of this threshold, however thicker layers appear to be far more common.

It should be noted that the cases where Model S were favoured often corresponded to thinner loops or threads with lower minor radii. This reduction in the spatial information may cause Model S to be favoured irrespective of the actual density profile. In some cases the background intensity was not accurately fit by the second order polynomial, however this is the same for each profile and is reflected in the 99% confidence levels shown in the middle panels of Fig. 4.1. It was found

that using higher order polynomials for the background trend could lead to different models fitting different portions of the intensity profile, invalidating their comparison. The most common radius of the loops analysed was 2Mm, for the transverse density profile rather than the apparent radius in the intensity images. This value is affected by selection effects as wider coronal loops were preferentially selected.

The use of the isothermal approximation means that any temperature variation across the loop that is sufficient to vary the response function of the AIA channel analysed (plotted in Fig. 1.24) will be interpreted as a density variation. This may have contributed to the prevalence of thick or continuous inhomogeneous layers obtained. However, considering the low correlation between the profiles seen in 171 Å and the hotter channels, the structures analysed at 171 Å may have a sufficiently narrow temperature distribution, with separate loops or threads existing in the hotter channels at similar, but not co-spatial, locations.

An additional complication is the potential presence of unresolved substructure in the loops and threads analysed, and the resulting LOS effects. This was studied for oscillating loops in [De Moortel & Pascoe \[2012\]](#). In the case of static loop observations the density profiles obtained relate to the density profiles of the unresolved threads, and how the filling factor varies as a function of radius. In the top row of Fig. 4.1 it is evident that the analysed loop appears to split into multiple structures towards the loop apex. This may mean that the intensity profile analysed may include several overlapping threads, which affect the transverse structure inferred, however the number of loops analysed is sufficiently large to avoid this being the case for all intensity profiles. Despite these assumptions and complications, in [Pascoe et al. \[2017b\]](#) an agreement was found between the seismologically determined value of ϵ and the value inferred from the intensity profile. Additionally, numerical simulations of [Magyar & Van Doorsselaere \[2016b\]](#) suggested that highly multi-threaded, or braided loops could be unstable to transverse oscillations. Since decayless kink oscillations appear to be ubiquitous [[Anfinogentov et al., 2015b](#)], this indicates that even if resolved loop threads are formed with unresolved substructure, they may quickly evolve to a more monolithic structure.

4.6 Conclusions

The intensity cross-section of coronal loop threads observed at 171 Å by SDO/AIA has been analysed. In this channel typical non-flaring coronal loops are seen with the highest clarity and contrast. Assuming an isothermal and cylindrical cross-section the transverse density structure of the coronal loop plasma which lies within the temperature range corresponding to 171 Å SDO/AIA channel is analysed.

Accounting for the instrumental PSF and integration along the LOS, very

strong evidence was found for the existence of an inhomogeneous layer where the density varies smoothly between the rarefied background plasma and the dense centre of the loop. In many cases, the width of this layer was high enough to conclude that the loop does not have a core at all, and has a continuously varying density which may be better modelled by a Gaussian profile. This may have implications for the thin boundary approximation often used in the analytical description of oscillating loops. Model L is found to be the most general as it can represent loops with no boundary layer as well as loops with a continuously varying density profile.

Several assumptions have been made to obtain these results. The study of multiple wavelengths, and the inclusion of the instrumental response function and a non-isothermal model for the loop cross-section require further work. The potential presence of unresolved sub-structure, and how this would manifest itself in the results should also be considered further. The loop is assumed to be static during the exposure time of the instrument. If they oscillate with a period shorter than the exposure time, or move during the exposure, some apparent diffusion of its boundary would be observed.

From this analysis it is clear that using a linear boundary layer density profile, forward modelled to the resulting intensity profile, produces more information than the Gaussian intensity profiles typically used to fit and track coronal loops. Even with simple least squares fitting, when the spatial resolution is sufficient, this profile would provide information about the size of the inhomogeneous layer compared to the minor radius, and decouples the measured minor radius from the intensity contrast.

Further work could include extension of this style of analysis to other coronal structures, in particular coronal structures which host waves that undergo dispersive evolution. The observed shape of the waveform depends strongly on the parameters of the waveguide in this case, making any information about the transverse density profile of such a structure important. Such waves are investigated in Chapter 5.

Chapter 5

Observation and simulation of dispersive coronal QFP wave trains

5.1 Introduction

As discussed in Section 1.5, Quasi-periodic Fast Propagating (QFP) wave trains in the corona are well resolved, temporally and spatially, however details for their excitation, evolution and damping remain unknown. Therefore their seismological potential has yet to be exploited. As mentioned in the last chapter, if the series of wave fronts are formed via dispersive evolution then the final observed waveform depends on the properties of the coronal structure it propagates through. In this chapter analysis of a flaring event which excites a series of propagating EUV intensity perturbations is presented, and numerical modelling which relates to the scenario observed is described.

In Sections 5.2 to 5.6 radio emission observations from the Learmonth and Bruny Island radio spectrographs are analysed to determine the nature of a train of discrete, periodic radio ‘sparks’ (finite-bandwidth, short-duration isolated radio features) which precede a type II burst. EUV imaging from SDO/AIA is analysed at multiple wavelengths. A series of quasi-periodic rapidly-propagating enhancements are identified, which are interpreted as a QFP wave train, and these are linked to the detected radio features. An introduction to these waves was given in Section 1.5. Compelling evidence is presented that a series of quasi-periodic ‘sparks’ in the radio spectra are linked to disturbances seen in the low corona in the EUV band. This is the first observation which links quasi-periodic fast waves observed in the EUV band to quasi-periodic features in radio spectra.

In Section 5.7 2D numerical simulations of impulsively generated wave trains

in a coronal plasma slab are presented, and how the behaviour of the trapped and leaky components depend on the properties of the initial perturbation is investigated. This aims to establish how these waves are affected by initial perturbations which enter the non-linear regime, thereby establishing the feasibility of one of the mechanisms by which the observations presented could be explained.

5.2 Solar radio emission

With the availability of imaging instruments simultaneously covering multiple wavelengths, and spatially resolved and unresolved recording of solar radio emission it becomes possible to study the relationship between MHD waves and oscillations and various non-thermal phenomena which may result in emission in the radio band [see, e.g. [Sych et al., 2009](#)]. One of the most intensively studied examples of this are type II radio bursts.

Coronal type II radio bursts are usually seen as two locally parallel emission lanes on solar radio spectrograms with an instant frequency ratio of approximately two, drifting from high to low frequencies. It is generally accepted that this radio emission is a result of plasma wave excitation at fronts of MHD shock waves propagating upwards through the corona. The lower and higher frequency lanes are thought to be emission at the fundamental and second harmonic of local plasma frequency, respectively [e.g. [Zaitsev, 1966](#); [Mann et al., 1995a](#); [Pick & Vilmer, 2008](#)]. The frequency drift of the lanes can be used to calculate the speed of the emission location, which is typically in the range of observed Coronal Mass Ejection (CME) velocities. Despite this established association the details of the physical relationship between flares, CMEs and the subsequent type II bursts is still only poorly understood.

The frequency of the emission from the MHD shock wave is given by the plasma frequency,

$$F = 8.98 \times 10^{-3} \sqrt{n_e} \text{ MHz}, \quad (5.1)$$

with the electron density, n_e , in cm^{-3} . Empirical models for the scaling of the coronal density with height can be used to determine the height and speed of the emission location using the electron density obtained from the frequency. A commonly applied model is the Newkirk model [[Newkirk, 1961](#)],

$$n_e = n_{e0} \times 10^{4.32(R_\odot/R)} \text{ cm}^{-3}, \quad (5.2)$$

where $n_{e0} = 4.2 \times 10^4 \text{ cm}^{-3}$. With this information it is possible to use EUV imaging observations to attempt to observe the emission location directly and compare the

observed position to these estimates. Sometimes a splitting of the main emission lanes (fundamental and harmonic) of the type II bursts into two or more additional sub-lanes is observed. There is no consensus on the cause of this phenomenon, possibilities include simultaneous radio emission from the downstream and upstream regions of a shock [e.g. [Smerd et al., 1974](#); [Zimovets et al., 2012](#)], multiple expanding structures in the CME creating multiple shocks, the passage of a single shock through surrounding structures [e.g. [McLean, 1967](#); [Schmidt & Cairns, 2012](#)] or a combination of these [[Zimovets & Sadykov, 2015](#)].

Solar radio bursts can be modulated by variation in the density of the background plasma by MHD waves. For example, Type IV bursts, broadband emission associated with high-energy non-thermal electrons accelerated during flares, exhibit fine structure and periodicity [e.g. [Magdalenic et al., 2005](#)]. Analysis of light curves from radio and microwave wavelengths showed signatures of QFP wave trains [e.g. [Mészárosová et al., 2009b, 2011](#)]. Zebra patterns were found to show periodic wiggling, interpreted as the modulation of the double-plasma resonance location by magnetoacoustic sausage oscillations [[Yu et al., 2013](#)].

5.3 Instruments and data

EUV imaging was used from SDO/AIA. The EUV data sets were retrieved in the FITS format from the JSOC data centre¹, with spatial and temporal resolution of 0.6 arcsec per pixel and 12 s respectively, using the SSW function `vso_search.pro`. The images were prepared and corrected using the standard SSW routine `aia_prep.pro`, and normalised by the exposure time of the instrument, which varies during the flare emission. The cadence also varies by ± 1 s from 22:41:00 UT, so the data for subsequent frames was re-binned to a constant cadence when required. Data was downloaded between 22:00 UT and 23:30 UT on 03/11/2014, resulting in 450 frames of 4096×4096 pixels. Two smaller fields of view of 800×800 pixels (bottom left corner $x = 0$, $y = 2100$) and 500×500 pixels (bottom left corner $x = 200$, $y = 2250$) used in the processing and analysis are shown in panel a) of Fig. 5.1.

Radio spectrograms covering the range 25-180 MHz were obtained from Learmonth Solar Radio Observatory in Western Australia, part of the USAF Radio Solar Telescope Network (RSTN) [[Kennewell & Steward, 2003](#)]. The data is arranged in two bands, 25-75 MHz and 75-180 MHz, and is linearly spaced in both. Supplementary data covering the range 6 to 62 MHz from the Bruny Island Radio Spectrogram (BIRS) [[Erickson, 1997](#)], located on Bruny Island off the south-eastern coast of Tasmania, was analysed to confirm the presence of features detected in Learmonth spectra qualitatively.

¹<http://jsoc.stanford.edu/ajax/lookdata.html>

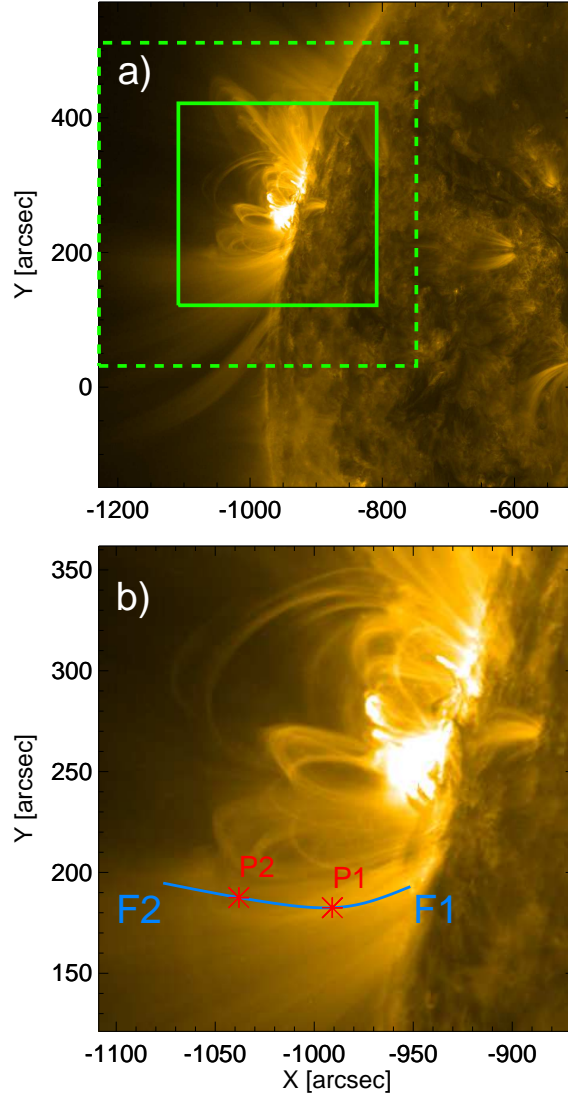


Figure 5.1: Panel a): SDO/AIA 171 Å image during the observed event at 22:00.00 UT centred on the active region of interest (AR 12205). The green boxes show the fields of view used for Fig. 5.2 (solid) and Fig. 5.7 (dashed). Panel b): the analysed region at 22:40:12 UT, F1 and F2 show the apparent extrema of the propagation path of the observed periodic intensity enhancements along a funnel structure, and the blue fit shows the slit used in the analysis. The red points P1 and P2 indicate the positions at which the time series plotted in Fig. 5.4 were extracted from.

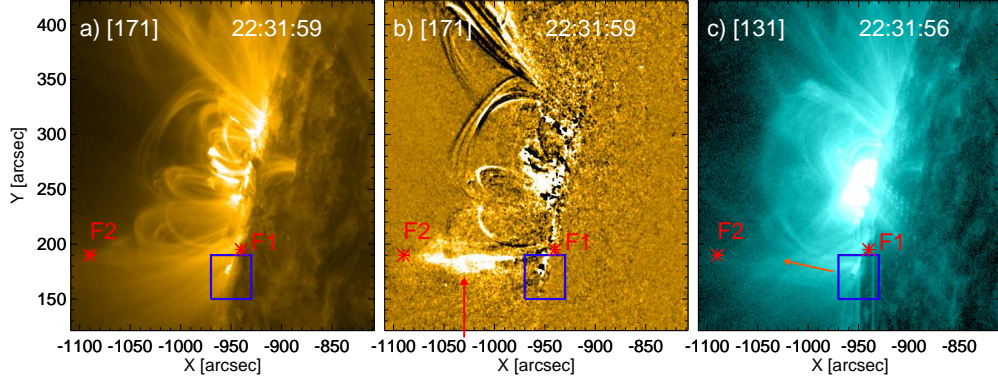


Figure 5.2: Three SDO/AIA images of the active region. In all panels a region of enhanced emission, associated with the ejection of the wave train, is highlighted by a blue box. The red points F1 and F2 indicate the observed start and end points of a guiding funnel structure. Panel a) shows the 171 Å image. Panel b) also shows a 171 Å image, with the previous frame subtracted. The red arrow indicates an enhancement propagating along the funnel. Panel c) shows a 131 Å image, the orange arrow indicates the direction of a propagating outflow.

Additional data for the flaring emission could not be obtained, as the Hinode instruments were targeting a different region of the disk, and ground based radio instruments such as the Nançay Radioheliograph, the Nobeyama Radioheliograph and the Siberian Solar Radio Telescope missed the event due to their respective instrumental night times. No spatial information was available in the radio band, and the RHESSI instruments recorded no data of interest during the event.

5.4 Observations and analysis

EUV and radio observations of a flaring event of GOES class M6.5 in the active region AR 12205 on the 3rd of November 2014 have been analysed. The active region is located on the eastern solar limb (see Fig. 5.1). The GOES X-ray lightcurves for the event, obtained using the SolarSoftWare (SSW) function `goes.pro`, show a characteristic flare, beginning at approximately 22:06:30 UT, and reaching its peak at 22:39:30 UT. A coronal mass ejection was associated with the flare, with an average projected propagation speed of $\sim 500 \text{ km s}^{-1}$ according to the Computer Aided CME Tracking (CACTus) catalogue² [Robbrecht et al., 2009]. A global EUV/EIT wave was also triggered.

²<http://sidc.oma.be/cactus/catalog.php>

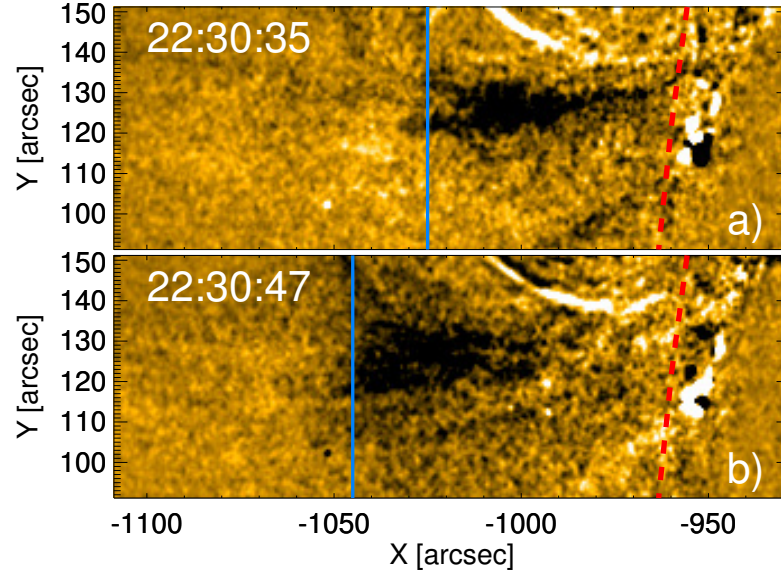


Figure 5.3: Two running difference images of the funnel structure at 171 \AA . There is a one frame (12 seconds) separation between the two images. The vertical blue lines approximate the position of the propagating wave front. The dashed red curve indicates the position of the solar limb.

5.4.1 EUV observations

A series of quasi-periodic intensity enhancements are seen within a guiding funnel structure in the 171 \AA band. One of the enhancements is indicated by the red arrow in panel b) of Fig. 5.2, between points F1 and F2. This series of enhancements will be referred to as a QFP wave train throughout the chapter. This guiding structure is part of a bundle of open and expanding flux tubes, or funnels, to the south of the active region. This structure is similar to those analysed in Liu et al. [2011] and Nisticò et al. [2014b], and modelled by Pascoe et al. [2013b], which were also found to guide QFP wave trains, as discussed in Section 1.5.

The projected speed of the wave train can be estimated from the observed distance the individual wave fronts move between frames. Using the positions indicated by the blue lines in Fig. 5.3 and the time between the observations, 12 seconds, a speed of 1200 km s^{-1} is obtained.

A slit was created by selecting a series of points along the centre of the propagation path of interest (between extrema F1 and F2) and fitting them with a spline function, plotted in panel b) of Fig. 5.1. A TD map was formed by interpolating over the pixels crossed by the fit, and averaging over an 11 pixel width, as discussed in Section 1.7.1. TD maps created from the normal intensity and running difference images, are shown in panels a) and b) of Fig. 5.4. The intensity profiles at two different distances are plotted on panel a), marked P1 and

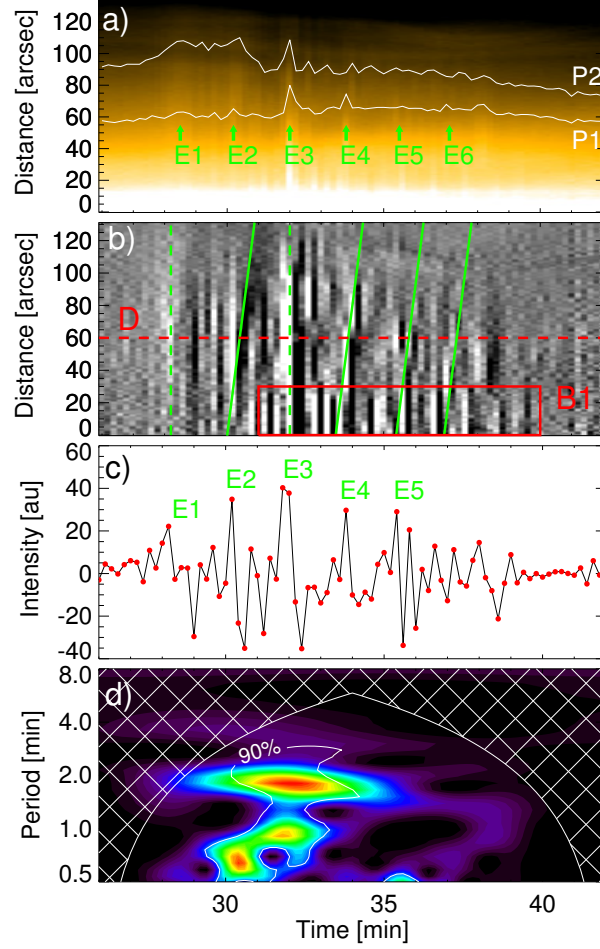


Figure 5.4: Panel a): Time-distance map formed from the slit along the path of intensity enhancements, between points F1 and F2, shown in Fig. 5.1. The intensity profiles labelled P1 and P2 show the intensity profile at different positions along the slit, and the green arrows indicate the position of main peaks, labelled E1-E6. Panel b): a TD map formed from a slit along the path of intensity enhancements in the running difference images. The diagonal green lines show the propagating intensity enhancements, and the dashed vertical lines indicate the enhancements where no propagation is seen. Box B1 highlights a series of enhancements of shorter spatial and temporal extent. Panel c): an intensity time series extracted from D in panel b), the intensity enhancements E1-E5 are labelled (E6 is missed as it is not prominent at the chosen distance along the slit). Panel d): Morlet wavelet spectra for the intensity time series, showing the distribution of the oscillation power with period as a function of time. The time axis of the four panels refers to the time elapsed since 22:00 UT.

P2.

The TD maps show a main intensity enhancement at 32 minutes (22:32 UT) and a series of additional enhancements before and after this peak, with an average temporal separation of $\delta t_{\text{EUV}} = 1.7 \pm 0.2$ min. These are labelled E1-E6 in panels a) and c) of Fig. 5.4. At low distances along the slit there is a series of more localised guided enhancements which are visible in both TD maps, these are not sufficiently resolved due to their apparent period of 24 seconds, twice the time resolution of the data. These features are highlighted in panel b) of Fig. 5.4 by box B1.

The gradient of a slope fitted to the main wave fronts can give a measurement of the propagation speed, however the scales involved are such that almost vertical fronts are obtained, not allowing an accurate estimate. However, some propagating features are seen, highlighted in Fig. 5.4 by the diagonal green lines, giving phase speeds of $\sim 1200 \text{ km s}^{-1}$, therefore the apparent phase speed is defined to be $\geq 1200 \text{ km s}^{-1}$, which is consistent with the estimate made from Fig. 5.3.

To observe the wave train fronts more clearly a time series was extracted from the running difference TD map at the distance marked by D in panel b) in Fig. 5.4. This is plotted in panel c), with E1-E5 indicating the peaks of interest (E6 is missed as it is not prominent at the chosen distance along the slit). The peaks are amplitude modulated. A Morlet wavelet spectra (see Section 1.7.2) of the intensity time series is shown in the bottom panel of Fig. 5.4. The solid white line corresponds to the 90 % significance level based on white noise. A powerful signal with a period of just below 2 minutes is present between 22:28 and 22:36 UT, reflecting the behaviour seen in the TD maps and time series, and agreeing with the period obtained. The 1 minute periodicity could be the second harmonic of the main 2 minute signal connected with non-linear effects, as it appears when the amplitude of the main signal is higher.

There is a region of enhanced emission seen at 171 \AA and 131 \AA , indicated in all three panels of Fig. 5.2 by the blue box. This lasts for the same duration as the series of enhancements and may be linked to the driving of the periodic wave train. In panel c) of Fig. 5.2 a propagating outflow is indicated, which has a different direction of propagation to the enhancements seen in 171 \AA , and is not periodic. This may be a jet of hot plasma related to the reconnection process indicated in Fig. 5.2 by the blue box. The direction of propagation does overlap with the path of the 171 \AA enhancements, and may contribute to the complexity of the data in Fig. 5.4.

5.4.2 Radio observations

The dynamic radio spectra show four discrete narrowband short-lived features (sparks) at frequencies, and therefore densities, similar to the type II burst. These features

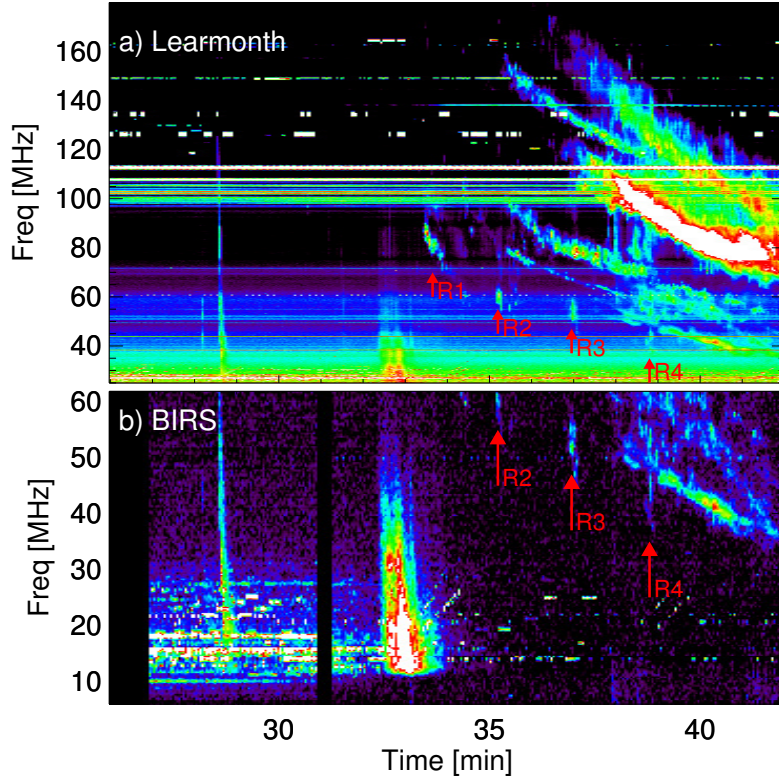


Figure 5.5: Learmonth, panel a), and BIRS, panel b), radio spectrograms in the ranges 25-170 MHz and 5-60 MHz respectively. Four regions of enhanced emission are indicated in panel a) by R1, R2, R3 and R4. R2-R4 are also indicated in panel b). The time axis refers to the time elapsed since 22:00 UT.

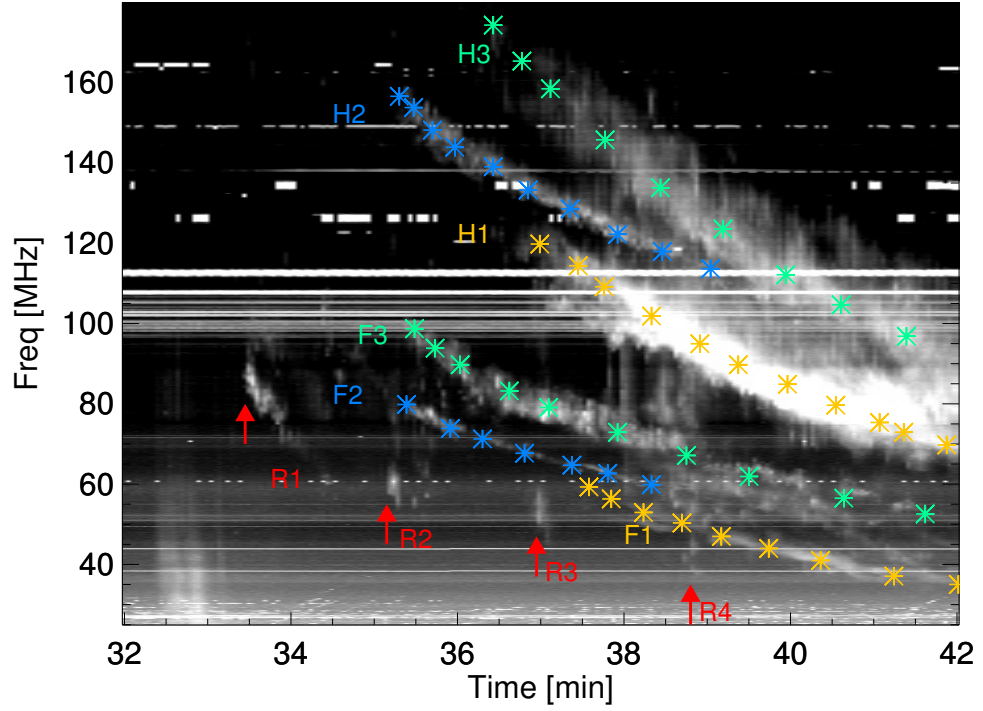


Figure 5.6: The Learmonth radio spectrograms. Three lanes of fundamental emission are indicated by F1, F2 and F3. Three lanes of harmonic emission are indicated by H1, H2 and H3. Four discrete regions of enhanced emission are indicated by R1, R2, R3 and R4. The time axis refers to the time elapsed since 22:00 UT.

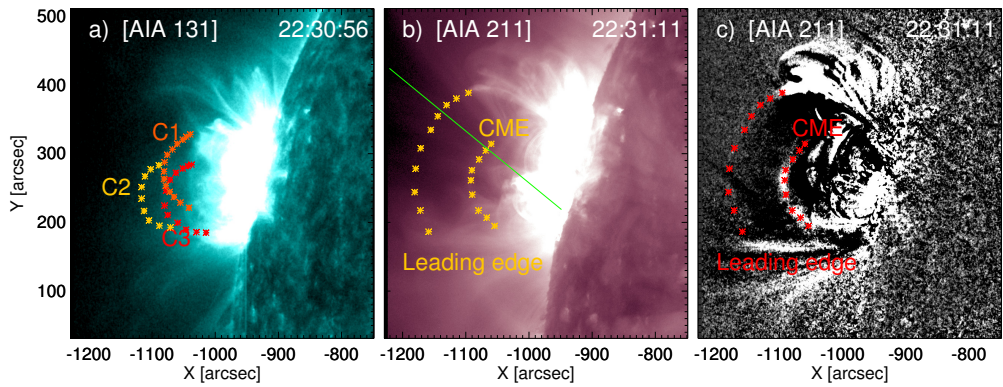


Figure 5.7: Panel a): a 131 Å image showing three separate components of the expanding CME labelled as C1, C2 and C3. Panel b) and c): 211 Å images with the CME and the leading edge which precedes it indicated in orange in panel b) and red in the difference image in panel c). The solid green line in panel b) indicates the position of the slit used to analyse the expanding feature ahead of the CME.

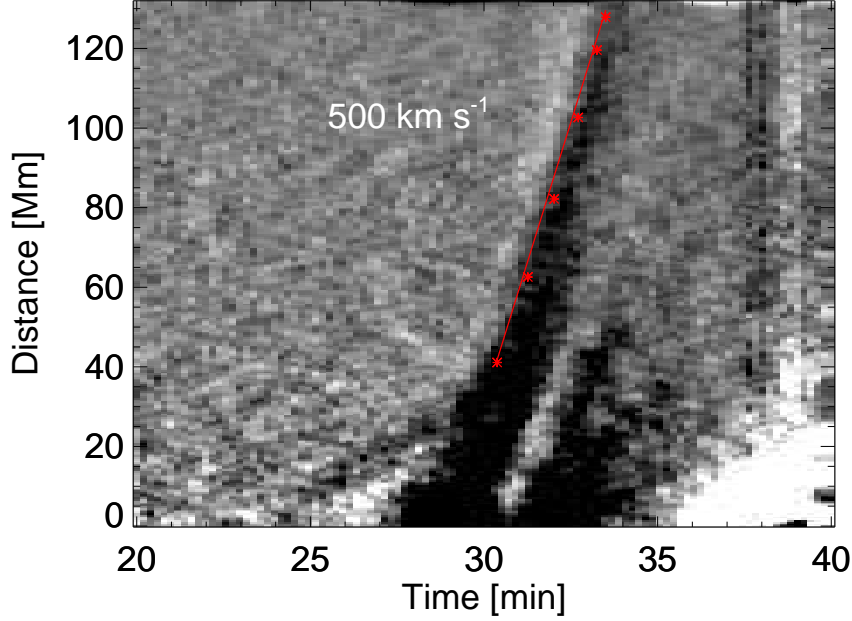


Figure 5.8: A TD map from the 211 \AA running difference images, formed from the slit marked in panel b) of Fig. 5.7. The red points and linear fit mark the propagating feature, corresponding to a speed of 500 km s^{-1} . The time axis refers to the time elapsed since 22:00 UT.

are labelled R1-R4 in Fig. 5.5. R1 shows some type-II-like drift, but in general, the properties of these features do not match any of the classical solar radio burst types and they will be referred to as radio sparks for convenience. R1 is missing from the BIRS spectrograph as it lies outside the observational band, therefore we use the Learmonth data for the following analysis.

The periodic sparks are centred on the following frequencies $F = [83, 59, 54, 42] \text{ MHz}$. Using the equation for the plasma frequency given in Section 5.2, and assuming that this emission is at the fundamental plasma frequency, these frequencies correspond to densities of $n_e = [8.47, 4.34, 3.56, 2.12] \times 10^7 \text{ cm}^{-3}$. Using the empirical formula for the height of these densities by rearranging the Newkirk formula given in Equation 5.2 yields heights above the base of the corona of $Z = [209, 288, 334, 418] \text{ Mm}$. The periodicity of the radio bursts is $P_r = 1.78 \pm 0.04 \text{ min}$ measured from the beginning of each spark.

A type II burst is also observed in this event as three separate strong lanes of emission, labelled as H1, H2 and H3 in Fig. 5.6. Using the plasma frequency and the Newkirk model as described above, the three lanes give speeds of $630, 380, 550 \text{ km s}^{-1}$, respectively. These are interpreted as the harmonic emission from the three weaker fundamental emission lanes, labelled as F1, F2 and F3. This indicates that the periodic sparks R1-R4 are not a typical type II emission lane as they do not have a stronger harmonic component. The time between the periodic sparks

and the relative change in height from the calculated density gives an estimate of the emission location speed of $v_{\text{em}} = 630 \text{ km s}^{-1}$.

5.4.3 Further analysis

The association between the periodic radio sparks and the CME is explored to make inferences about the location at which the radio sparks are produced. The height of the CME leading edge indicated in panel b) and c) of Fig. 5.7 is 247 Mm at the time of the first radio burst. A TD map, shown in Fig. 5.8, taken from the slit indicated in panel b) of Fig. 5.7 gives a speed of $\sim 500 \text{ km s}^{-1}$ for the CME leading edge. This slit position was chosen as it offers the best signal to noise ratio for detecting the propagation. Extrapolating this position forward to the times of the subsequent radio sparks, which are after it has left the observational FOV, gives heights of $Z = [247, 298, 349, 400] \text{ Mm}$, which are roughly consistent with the emission heights of the radio sparks derived above.

From the upper and lower frequencies of each radio spark it is possible to estimate the vertical extent of the emission region. From the frequencies the corresponding densities are obtained assuming the emission is at the electron plasma frequency, which are then used to calculate the upper and lower heights of the emission from the Newkirk formula. The resulting vertical lengths of the emission region for each spark are $L = [29, 24, 26, 32] \text{ Mm}$.

The complex nature of the expanding CME structure is highlighted in panel a) of Fig. 5.7. Three separate expanding structures were identified from the series of images and are labelled as C1, C2 and C3. This series of expanding structures, and the complex geometry of the active region, provide adequate mechanisms to produce the 3 fundamental and harmonic emission lanes highlighted in Fig. 5.6. This is supported by the speeds derived from the drifts in the radio spectrum, which are in the range of typical CME velocities in the corona.

Finally, if it is assumed that the wave train fronts cause the radio sparks when they reach the propagating feature ahead of the CME indicated as ‘leading edge’ in Fig. 5.7, then the temporal separation ($t_r - t_{\text{EUV}}$) and height of the emission, Z or Z_{CME} , can be used to estimate the average wave train propagation speed between the active region and the emission location. Matching the first EUV enhancement E1 with the first radio burst R1, and subsequently E_i with R_i , gives $v_{\text{EUV}} = [700, 970, 1120, 1390] \text{ km s}^{-1}$. Matching the strongest wave train enhancement E3 with R1, and subsequently E_{i+2} with R_i , gives $v_{\text{EUV}} > 4000 \text{ km s}^{-1}$, which is unrealistic for fast magnetoacoustic waves in the corona. The first set of speeds are approximately consistent with the speeds measured lower in the corona for the propagating wave train fronts.

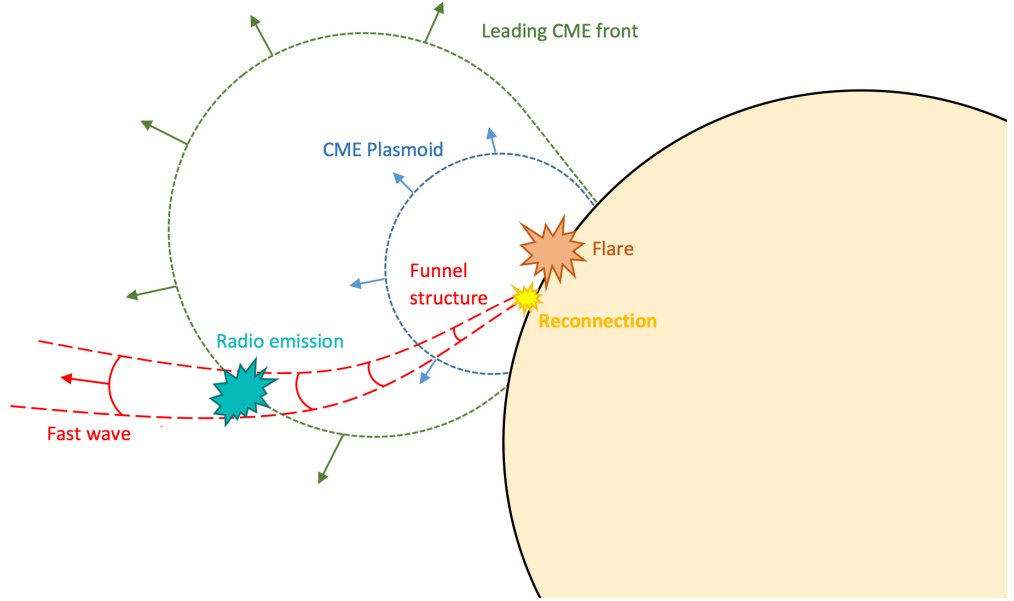


Figure 5.9: A schematic synopsis of the event. A flare occurs which is followed by a CME comprising of the leading edge or EUV wave (green) and the main CME plasmoid (blue). A funnel structure (red) within the active region is seen to host a series of rapidly propagating quasi-periodic waves. A brightening is observed at the base of this structure and is interpreted as a reconnection site. After a certain delay periodic radio sparks are observed, which occur at an estimated height consistent with the leading feature of the CME, and a periodicity consistent with the fast wave period.

5.5 Discussion of observational results

Quasi-periodic EUV intensity disturbances are found to propagate along a guiding funnel structure during a flaring event, beginning at 22:27:59 UT. The period is $P_{\text{EUV}} = 1.7 \pm 0.2$ min, which becomes more pronounced with distance along the wave guide. The CME plasmoid associated with the flaring event is seen to interact with the active region at 22:27:56 UT, resulting in a region of enhanced emission seen in all channels analysed near the base of the funnel structure. Thus, it can be assumed that the periodic wave train is induced by the CME interaction with background structures, possibly due to the resulting reconnection. A series of small radio bursts, or sparks, occurs during the CME expansion prior to the type II emission. These have a period of $P_r = 1.78 \pm 0.04$ min, making it a reasonable assumption that they are linked to the QFP wave train.

The EUV intensity disturbances can be interpreted as a series of guided fast magnetoacoustic waves (Quasi-periodic Fast Propagating (QFP) wave train), discussed in Section 1.5. These may be formed by the dispersive evolution of a

pulse excited in the guiding structure, or by a periodic quasi-harmonic driver. Some wave train fronts are clearly seen to propagate with projected speeds of 1200 km s^{-1} , which are consistent with previous QFP wave train observations. Some previous studies have interpreted the observed wave trains as the result of repetitive magnetic reconnection associated with the flare, or another mechanism which periodically excites broadband pulses of fast waves [Liu & Ofman, 2014]. Recent modelling results from Yang et al. [2015] have confirmed this as a viable mechanism for the production of a series of fast waves with phase speeds and characteristics which match observations.

Other possibilities for the nature of the enhancements exist, such as periodic jets. However jets are normally multi-thermal and are therefore seen in multiple channels [Nisticò et al., 2009]. In the observations no signature of the intensity enhancements was seen at other AIA wavelengths. Jets are also normally seen as narrow structures, which are more long lived than the observations, and do not have low periodicities of several minutes. It is possible that a superposition of fast waves and plasma ejections is present, which would explain the complex dynamics observed.

The triple band type II burst is clearly resolved in the radio spectrograms, and it is possible to match the strong harmonic emission lanes with their fundamental counterparts. The series of periodic radio sparks which precede these do not correspond to any of the observed lanes, leading to their interpretation as a separate phenomenon, which causes emission at the local plasma frequency without a second harmonic component. They approximately follow the same drifting trend as the fundamental components however, meaning their emission location may exhibit the same dynamic behaviour as the CME which produces the shocks. Drifting velocities of H1, H2 and H3 to be 630 , 380 and 550 km s^{-1} were found, therefore they are interpreted as emission associated with spatially separated shock waves driven by different parts of the expanding CME.

Since the QFP wave train observed in the low corona and the series of radio sparks have almost equal periods, the QFP wave train can be considered as the driver of the periodic radio sparks. The slight offset in the detected periods may support this, as the time delay between the radio sparks is expected to be longer than the wave train period, due to the increasing height of the emission location. An estimate of the transit velocity from the base of the guiding structure to the radio burst emission location can be made using the inferred distance and time delay between the observations. The most reasonable estimates came from matching wave train fronts E1 or E2 with R1, which gives transit velocities in the range $800 - 2000 \text{ km s}^{-1}$, which are roughly consistent with the velocities measured from the TD map in Fig. 5.4, and are in the range of the expected fast magnetoacoustic speed in

the corona. There is a large degree of uncertainty associated with these estimates, however it is clear that the time delay between the EUV and radio features is large enough to exclude energetic particles accelerated in the active region as the driver of emission at these heights, due to their characteristic high propagation velocities.

The proposed scenario is similar to the ‘cannibalism’ of CMEs, when one faster CME (ejected later) catches another slower CME (ejected earlier). In some of these cases it has been found that the related type II radio burst emission can be enhanced during this process of two CMEs merging [e.g [Gopalswamy et al., 2001](#); [Martínez Oliveros et al., 2012](#)].

The different spectral aspects of the radio sparks can be explained by the properties of the wave fronts, which may have different temporal and spatial extents, similar to the snapshots of the fast magnetoacoustic waves generated by geometrical dispersion in a plasma funnel in [Pascoe et al. \[2013b\]](#). The first spark exhibits a frequency drift, which can be explained by a broad wave front, such as the one indicated in Fig. 5.2. Additionally, from Fig. 5.4 panel a) it can be seen that E1 is temporally broader than the following peaks, which could give rise to the drift seen in R1. From the frequency range each spark covers the vertical extent of the emission region for each was calculated, giving $L = [29, 24, 26, 32]$ Mm for R1 - R4. These values support the interpretation that the emission is generated in a localised region corresponding to a feature of finite vertical width, such as the expanding front ahead of the CME.

The estimated heights at which the radio sparks (R1-R4) are generated roughly match the positions of the CME leading edge marked in Fig. 5.7. Additionally, the trend of the sparks in the radio spectra matches the drifting of the fundamental emission lanes, indicating a definite link to the kinematics of the CME. The CME leading edge may be a developing EUV wave before it has decoupled from the expanding CME.

Possible excitation scenarios to produce the periodic radio emission include: steepening of the QFP wave train fronts which shock in the medium of the expanding CME leading edge, emission due to the compression of the medium between the CME leading edge and the approaching fast waves, or alternative emission mechanisms such as the cyclotron-maser mechanism discussed in [Wu et al. \[2005\]](#). These scenarios would produce accelerated electrons, the bump-on-tail instability, and subsequent emission of radio waves with a frequency corresponding to the local electron plasma frequency.

Another possibility exists to explain the periodic radio emission without the inclusion of the CME features. Panel c) of Fig. 5.4 shows that the series of EUV enhancements vary in amplitude. Fast wave steepening depends on the waves amplitude, so different cycles of oscillation in the amplitude-modulated dispersively-

formed QFP wave train [e.g. Jelínek et al., 2012; Pascoe et al., 2013b; Mészárosová et al., 2014] will shock at different heights in the corona, which could produce the drifting of the sparks from high to low frequency as observed. However, this scenario does not explain why the appearance of the sparks in the radio spectrum matches the drift of the type II bursts.

5.6 Summary of observational results

A flaring event and the associated CME and periodic waves were analysed with SDO/AIA data, in addition to the corresponding radio features with Learmonth and BIRS data. A series of finite-bandwidth, short-duration isolated radio features drifting from high to low frequency are observed. The period of these radio sparks, $P_r = 1.78 \pm 0.04$ min, matches the period of the rapidly propagating wave train observed at 171 \AA , $P_{\text{EUV}} = 1.7 \pm 0.2$ min. The speed of the radio emission location, 630 km s^{-1} , estimated from the instant frequencies of the radio sparks, is of the same order as the speed of the CME and its leading edge, 500 km s^{-1} . The calculated height of the radio emission matches the observed (and then projected forward using the observed velocity) location of the leading edge of the CME. Using the time delay between the wave train fronts and radio sparks and the height of the emission, propagation speeds in the range of fast magnetoacoustic waves are obtained.

The observations may be interpreted with the following scenario. A series of fast waves are produced by the active region during a flare, during an energetic energy release. The waves propagate upwards along a funnel structure, and interact with the CME leading edge, or some associated disturbance that propagates slower than the fast wave train. This results in the acceleration of electrons, the bump-on-tail instability, and emission of radio waves with the frequency corresponding to the local electron plasma frequency, appearing as quasi-periodic sparks in the radio spectrograph (see Fig. 5.9). Theoretical modelling of the potential emission mechanisms is needed. A first attempt to model one of the possible scenarios is presented in the following section.

5.7 Modelling of non-linear dispersively formed QFP wave trains

Quasi-periodic Fast Propagating (QFP) wave trains are frequently observed in EUV images of the solar corona, or their existence is inferred from the quasi-periodic modulation of radio emission. The dispersive nature of fast magnetoacoustic waves in coronal structures provides a robust mechanism to explain the detected quasi-periodicity. 2D numerical simulations of impulsively generated wave trains in coronal

plasma slabs are performed. How the behaviour of the guided and leaky components depends on the properties of the initial perturbation is investigated. High amplitude perturbations should lead to non-linear wave steepening, generating a QFP wave train with a series of steepened fronts. This could explain the series of radio sparks which accompany the fast waves in the observational study presented at the beginning of this chapter.

Simulations are performed using LARE2D [Arber et al., 2001], a 2.5D MHD code which solves the non-linear MHD equations. A Lagrangian predictor-corrector time step is applied and the variables are then remapped back onto the original Eulerian grid, using van Leer gradient limiters. The code is well suited to the modelling of the dispersive evolution of perturbations in wave guides, and has been used for several related studies [Nakariakov et al., 2004; Pascoe et al., 2013b; Nisticò et al., 2014b].

5.7.1 Numerical setup

The numerical setup is similar to previous studies which have used the 2D slab geometry. The magnetic field is taken to be straight and uniform in the x -direction, with strength B_0 . A coronal loop, or other waveguiding structure, is modelled with a field-aligned density enhancement. The transverse density structure (y -direction) is given by the general symmetric Epstein profile

$$\rho = (\rho_0 - \rho_e) \operatorname{sech}^2 \left(\frac{y}{w} \right)^p + \rho_e, \quad (5.3)$$

where ρ_0 is the density at the density enhancement axis, ρ_e is the density outside the density enhancement, $p \geq 1$ determines the density profile steepness, and w is the waveguide half-width. The parameters used are $\rho_0/\rho_e = 4$ and $p = 8$. This choice of steepness parameter closely approximates the step function profile in terms of wave behaviour while remaining smooth and hence numerically well-resolved, and physically feasible, as shown in Chapter 4 for coronal loops. The setup is shown in Figure 5.10.

The density structure is set in equilibrium by defining the internal energy density ϵ as

$$\epsilon = \frac{p_{\text{gas}}}{\rho_0 (\gamma - 1)}, \quad (5.4)$$

to counter act the density enhancement, where p_{gas} is the (constant) gas pressure and $\gamma = 5/3$ is the ratio of specific heat capacities. The gas pressure value chosen gives a low plasma beta of $\beta = p_{\text{gas}}/p_{\text{mag}} = 0.05$, where $p_{\text{mag}} = B_0^2/2\mu_0$, which is a typical value for the solar corona. The initial perturbation is a localised compressive velocity perturbation of the sausage symmetry in the centre of the density enhancement

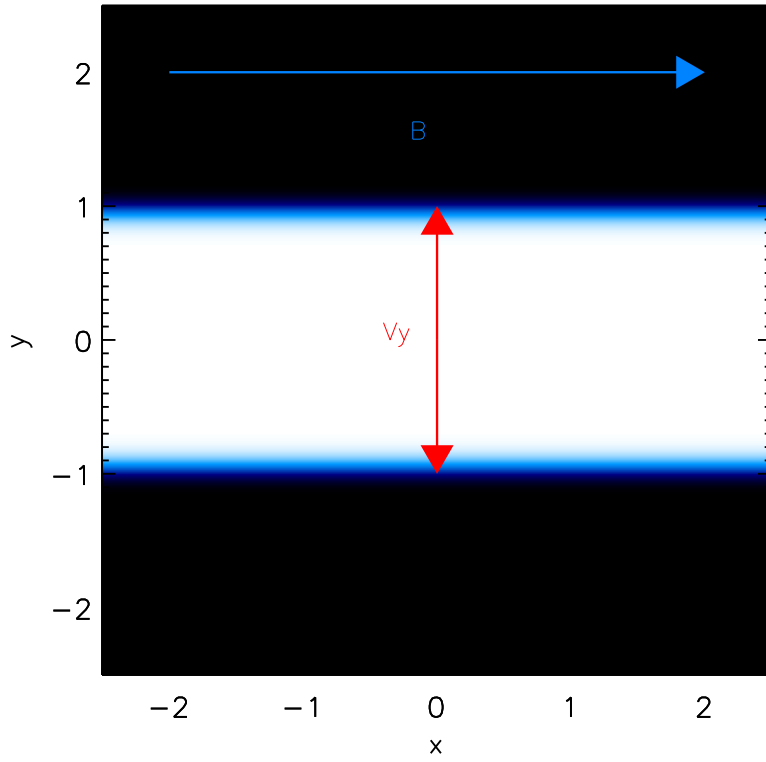


Figure 5.10: An overview of the numerical setup, showing the centre of the domain (the full domain is 300 length units in both directions). The density structure is shown, with white corresponding to the internal density of 4, and black to the external density of 1. The blue arrow denotes the direction of the uniform magnetic field. The red arrows denote the position and direction of the initial velocity perturbation.

($x_0 = y_0 = 0$), with the form

$$v_y = \frac{v_{y0}}{\Delta_x \Delta_y} y \exp \left[- \left(\frac{x - x_0}{\Delta_x} \right)^2 - \left(\frac{y - y_0}{\Delta_y} \right)^2 \right], \quad (5.5)$$

where v_{y0} is the initial amplitude, and the parameters Δ_x and Δ_y prescribe the width of the initial perturbation. The perpendicular spatial scale is set to be the density enhancement width $\Delta_y = w = 1$, and $\Delta_x = \Delta_y$, which efficiently excites the fundamental modes of the waveguide.

The 2.5D approximation implied by the use of LARE2D gives $\partial/\partial z = 0$. Due to the geometry and nature of the chosen perturbation, v_z and B_z remain zero hence the model is essentially 2D.

The resolution used in all simulations was 8000×8000 grid points, and convergence tests at a resolution of 16000×16000 grid points show no notable differences. Reflective boundary conditions are used, although the simulations end before any perturbations reach the boundaries. In normalised units the domain size is 300×300 , i.e. 300 half-widths of the waveguide. Length scales (X, Y), time scales (T), and speeds (V) in physical units are related to the dimensionless variables via $X = x w$, $T = t t_0$, and $V = v v_0$, where w , t_0 , and v_0 are the chosen normalisation constants and $v_0 = w/t_0$.

5.7.2 Numerical results

Numerical simulations were run with increasing values of the perturbation amplitude, A_0 in Equation (5.5). The amplitudes are given as the maximum value of the applied perturbation v_{y0} relative to the external Alfvén speed C_{Ae} . The density perturbation (i.e. with the density profile at $t = 0$ subtracted) at time $t = 60$ for the largest amplitude simulation $v_{y0}/C_{Ae} = 1.5$ is shown in Fig. 5.11. The region shown has been shifted to focus on one half of the domain as the simulation is symmetric about the x and y axis. The guided components form two fast wave trains propagating in the positive and negative x -directions, which have evolved to have an extended quasi-periodic nature due to dispersion. The perturbations nearest to the origin correspond to the slow mode, and propagate very slowly relative to the fast mode due to the low- β plasma. The leaky components are also fast waves, and leave the density enhancement and once outside propagate at the external fast speed, which is mainly determined by the external Alfvén speed $C_{Ae} = 1$. Both the guided and leaky components are highlighted in Fig. 5.11.

In Fig. 5.12 the top and bottom panels show snapshots of the full density, rather than the density perturbation. The top panel demonstrates that the amplitude is high enough that the guided sausage wave train noticeably perturbs the boundary of the density enhancement. The slow mode at $x \approx 20$ has formed a shock,

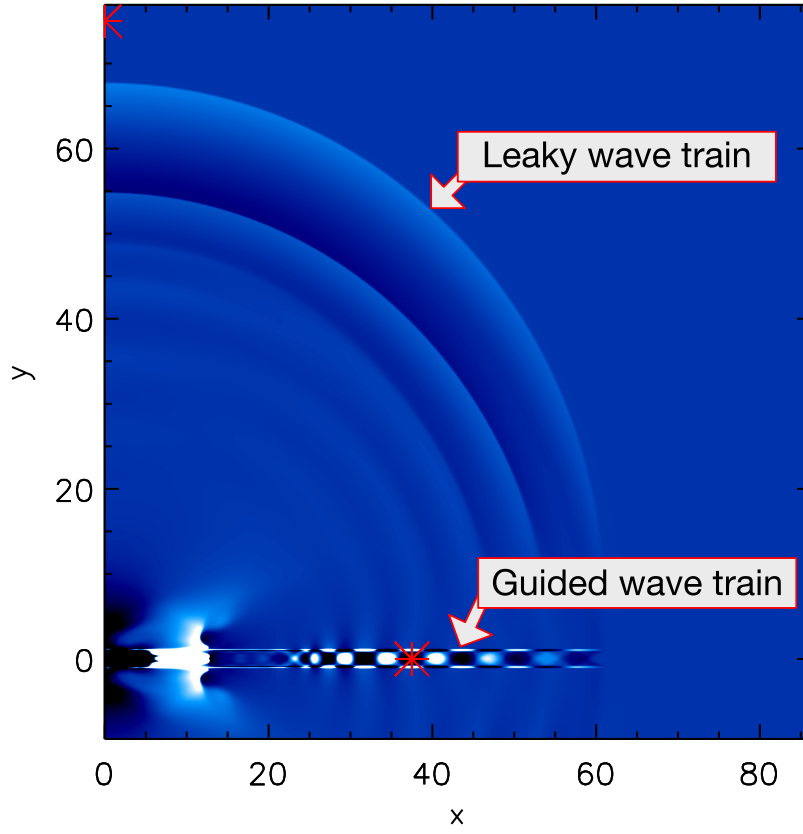


Figure 5.11: Snapshot of a region of the numerical domain for the largest amplitude initial perturbation ($v_{y0}/C_{Ae} = 1.5$) showing the density perturbation towards the end of the simulation run-time. The leaky and guided components are labelled. The red asterisks show the locations where the time series are taken for the guided and leaky wave trains.

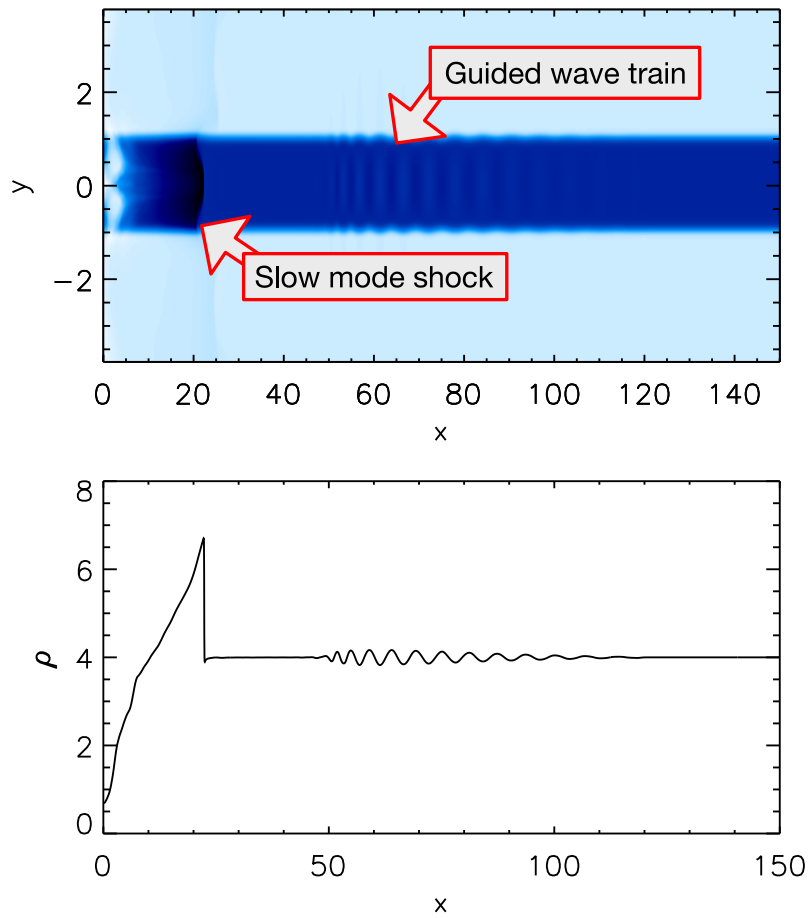


Figure 5.12: Top: the absolute density at time $t = 125$ in the region of the numerical domain around the density enhancement. Bottom: the one dimensional density profile at $y = 0$ in the top panel.

and the entropy mode can be seen at $x = 0$. The bottom panel shows the profile of the density taken at $y = 0$. Figure 5.13 shows the maximum amplitude of density perturbations due to the leaky component as a function of distance in the y direction. The wave train attenuates as it propagates due to the geometric expansion of the wave front. For the lower amplitude perturbations, the maximum amplitude of the perturbations follows the $1/\sqrt{y}$ behaviour expected for an expanding, circular wave front created by a localised perturbation, while higher amplitudes experience additional attenuation due to non-linear dissipation associated with the wave front steepening.

Compared to the guided wave trains, the leaky components travel at a greater speed, and have a longer wavelength and correspondingly longer period. They also have a lower quality factor (i.e number of cycles) since they are dispersionless once in the external uniform plasma, and hence do not evolve (except the geometric, cylindrical decrease in the amplitude and non-linear steepening, addressed above). Both leaky and guided fast wave trains could be responsible for the observations of QFP wave trains introduced in Section 1.5 and presented earlier in this chapter.

The density perturbation signals are measured at $(37.5, 0)$, corresponding to the guided wave trains, and at $(0, 75)$, corresponding to the leaky wave trains propagating perpendicular to the slab axis. The results for three different amplitudes of the initial perturbation are shown, $A_0 = 0.01, 0.5$, and 3.5 , or $v_{y0}/C_{Ae} = 0.004, 0.30$, and 1.50 . The density perturbation time series for the guided component is shown in Fig. 5.14, with the corresponding wavelet spectra in the lower panels. The same is shown for the leaky component in Fig. 5.15.

For the guided wave train, the amplitude of the perturbations increases with the amplitude of the driver, but the wave trains are otherwise very similar and there is no sign of non-linear steepening. There is the appearance of high-frequency oscillations at $t \gtrsim 95$ which increase with v_{y0} . This demonstrates that the geometrical dispersion is strong enough to prevent the steepening of the wavefronts inside the waveguide, even in cases when it is sufficiently large to cause the slow mode to steepen (see Figure 5.12).

The leaky wave trains excited by the different amplitude perturbations exhibit a similar number of oscillation cycles, as determined by the dispersive evolution experienced before the waves leave the density enhancement. After this no further geometrical dispersion occurs in the uniform external medium, however the wave trains evolve by non-linear steepening, at a rate determined by the wave train amplitude relative to the local propagation speed (approximately the external Alfvén speed). The steepening can clearly be seen in the second time series in Fig. 5.15 ($v_{y0} = 0.30$) and is even stronger in the third time series ($v_{y0} = 1.5$)

The attenuation of the external wave train due to expansion of the wave fronts

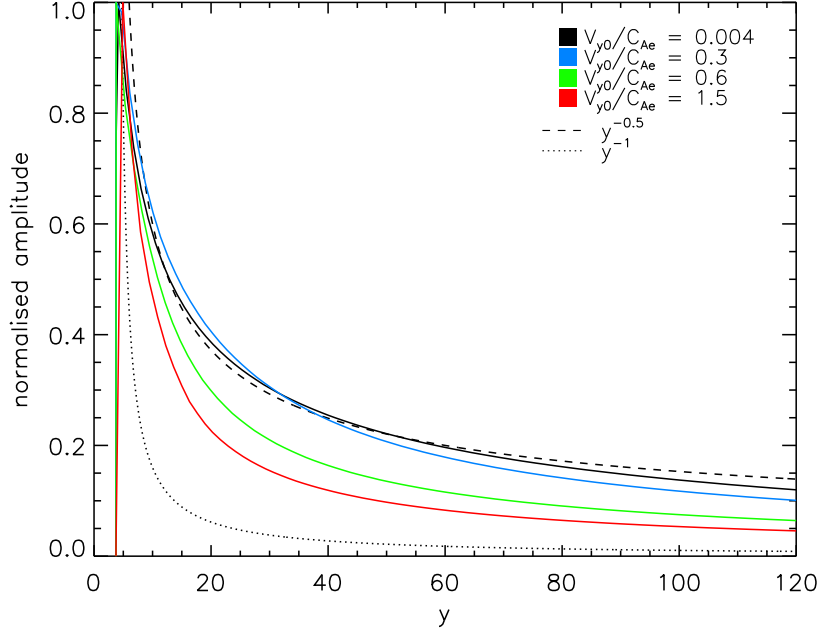


Figure 5.13: Dependence of the maximum amplitude of the leaky wave train measured at $x = 0$ on propagation distance y for different amplitudes of the initial perturbation.

in Fig. 5.15 is approximately $75^{-1/2} \approx 0.12$ and so the leaky wave train amplitude upon leaving the density enhancement is comparable to that of the guided wave trains. The amplitude of the external wave train upon leaving the density enhancement is determined not only by the initial perturbation but also the perpendicular density profile. The density contrast and steepness of the profile determine both the extent of the dispersive evolution and the fraction of wave energy which leaks away. It also depends on the relative spatial size of the initial perturbation with respect to the width of the waveguide.

5.7.3 Discussion and Summary of numerical results

It has been demonstrated that multiple steepened wave fronts can be formed by a single impulsive event with a sufficiently large amplitude. The geometrical dispersion provided by coronal structures is required to generate QFP wave trains, however the dispersion also efficiently suppresses non-linear steepening in the guided wave train. Therefore the leaky component produces the steepened wave fronts and is the candidate for shock formation and the acceleration of particles within the corona. This mechanism could therefore account for the observation of quasi-periodic type-II-like radio bursts after a flare or coronal mass ejection, and particularly those with a similar periodicity to a wave train observed in EUV such as the observations

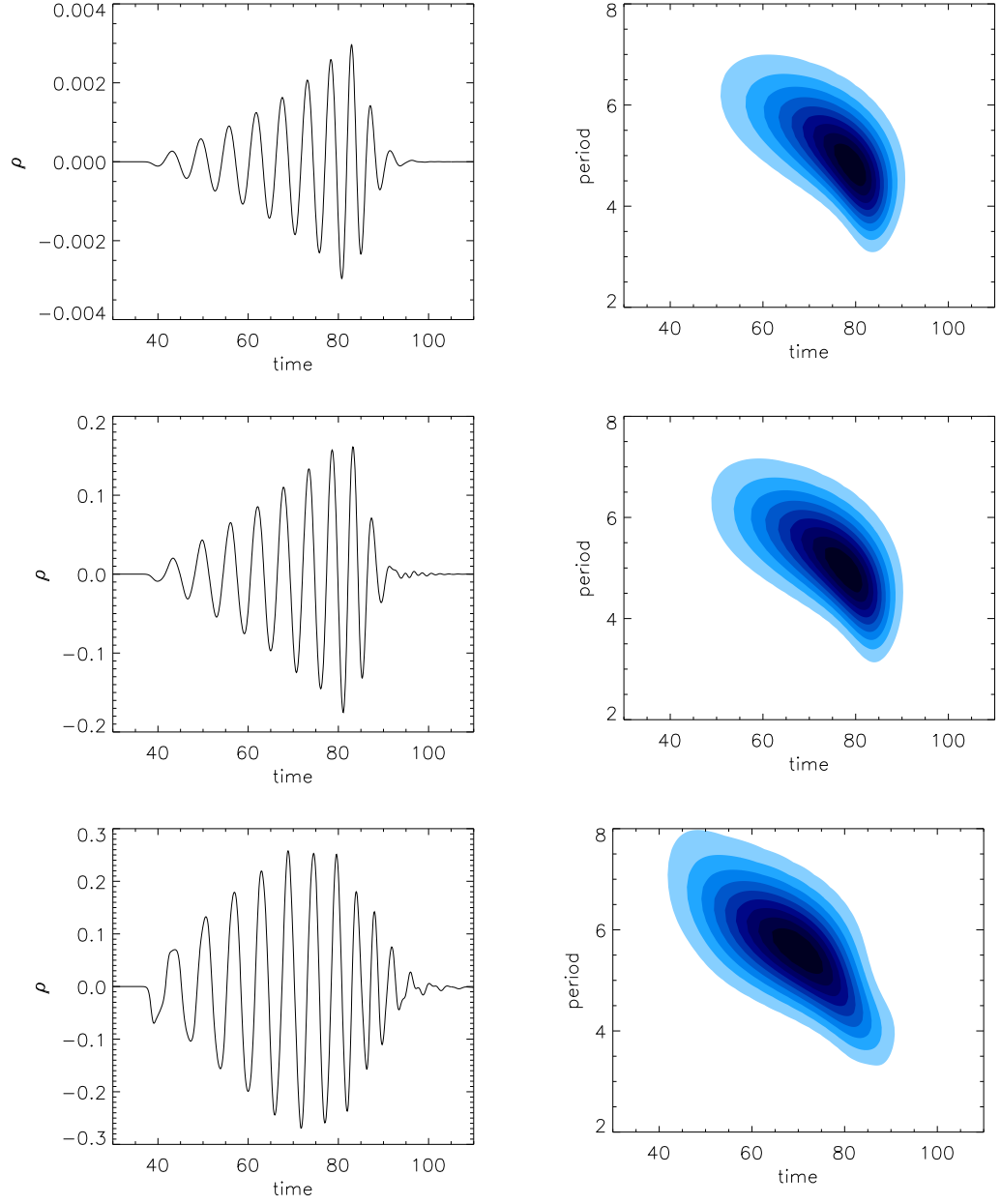


Figure 5.14: Guided wave train time series and wavelet analysis for different amplitude initial perturbations. The applied perturbation amplitude, v_{y0}/C_{Ae} , is 0:004 (top), 0:30 (middle), and 1:50 (bottom).

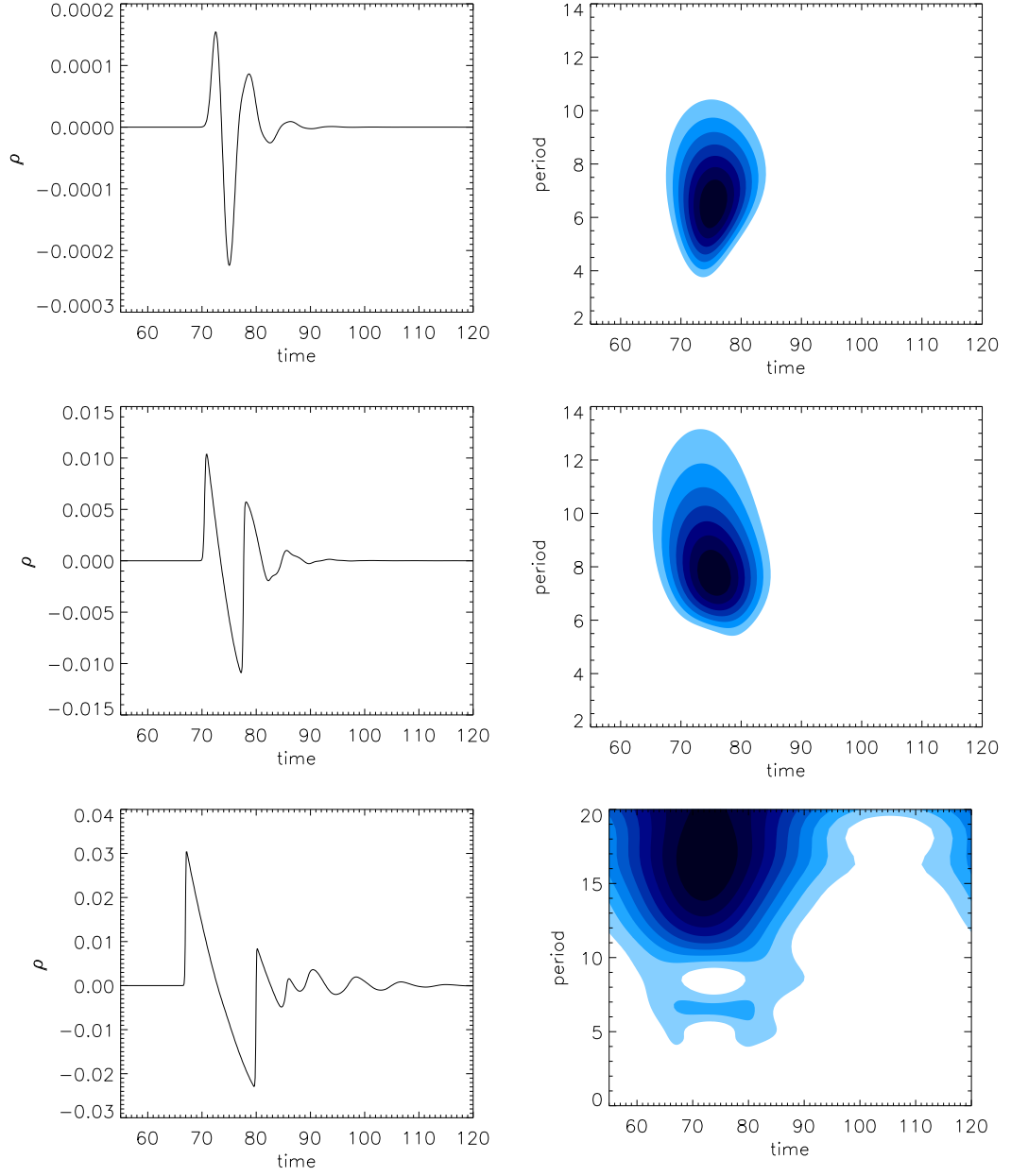


Figure 5.15: Leaky wave train time series and wavelet analysis for different amplitude initial perturbations. The applied perturbation amplitude, v_{y0}/C_{Ae} , is 0:004 (top), 0:30 (middle), and 1:50 (bottom).

presented above, and recently in [Kumar et al. \[2017\]](#). However, it is necessary to appreciate that the shocks will be generated by the leaky components of the impulsively generated wave trains, and to distinguish whether any imaged wave train also corresponds to the leaky or the guided components, or if both are observed as in [Nisticò et al. \[2014b\]](#). It should be noted that many of the detected QFP wave trains are formed within open, expanding coronal structures, as such the guided components may still shock as the effect of dispersion will reduce with distance propagated. This will be the subject of further study.

When considering how the simulation units relate to physical quantities the choice of normalisation should be consistent with the MHD approximations. No kinetic effects are included in the modelling. The focus is the behaviour of non-linear MHD waves in terms of their capability to produce steepened wave fronts which may generate radio bursts, but without directly modelling the associated particle acceleration processes required. A low value of β was chosen to give separation between the fast and slow waves, which should also be the case in most regions of the corona. A normalisation for the slab width w could be chosen to match the observations earlier in the chapter. The absolute values of the density and magnetic field could then be adjusted so the waves speeds also match those in the observations. However, since the model is effectively scale free and the steepening is not dependant on the absolute value of those parameters, the results have been presented in normalised units.

In comparison with standing kink oscillations of coronal loops, the seismological techniques based on QFP wave trains are far less advanced. Previous studies demonstrate how the particular shape of the (guided and leaky) wave trains, or its appearance in wavelet analysis, depends on the density profile of the guiding density structure [e.g. [Jelínek & Karlický, 2012](#); [Oliver et al., 2014](#)]. However, no simple inversion technique currently exists to determine the plasma, or structuring, parameters from the measured oscillation parameters. If the structure of the density enhancement was known a much narrower parametric study could be performed to determine the properties of the driver (e.g. A , Δ_x) required to reproduce the observed wave trains and/or the corresponding ‘radio sparks’. The technique applied to determine the transverse density structure of coronal loops in Section 3.5 and Chapter 4 may be applied to loops or other coronal structures in which QFP wave trains are seen to propagate.

For large amplitude compressive perturbations, the geometrical dispersion associated with the waveguide suppresses the non-linear steepening for the guided wave train. The wave train formed by the leaky components does not experience dispersion once it leaves the waveguide and so can steepen and form shocks. The mechanism considered could lead to the formation of multiple shock fronts by a sin-

gle, large amplitude, impulsive event and so can account for quasi-periodic features observed in radio spectra, such as those described earlier in the chapter.

Chapter 6

Summary

In this thesis, observations of MHD waves in coronal structures observed with SDO/AIA have been presented, in addition to a study of the structures themselves, and numerical simulations of some of the wave processes.

A statistical study of decaying kink oscillations was performed in Chapter 2. This was the first large scale, statistically significant, self-consistent study of decaying kink oscillations. A linear dependence was found between the period of oscillation and the length of the loop, confirming that the standing kink mode is being observed. The gradient from a linear fit of the data cloud gave a value for the average kink speed in the analysed loop of $C_k=(1300\pm50)$ km s⁻¹, with lower and upper bounds of $C_k=(800-3300)$ km s⁻¹. Plotting the exponential damping time of the oscillations against the period of oscillation gave a linear dependence between the two parameters, but without enough accuracy to make any further conclusions. However, it was noted that many of the oscillations were not well described by an exponential damping envelope, leading to the confirmation of the Gaussian damping regime used to perform seismology in the next chapter. Finally, plotting the quality factor (τ/P) of the oscillations against the oscillation amplitude revealed the signature of additional damping at high amplitudes. This may be attributed the non-linear effects which are more prevalent at high amplitudes, and produce additional damping, or cause significant disruption to the loop itself.

Coronal seismology with select cases from the statistical study was carried out in Chapter 3 using the general damping envelope described in Section 1.4.2. This consists of a Gaussian damping envelope which switches to an exponential envelope after a characteristic time. This is the first time this theoretically predicted damping envelope has been applied to observational data, and used to perform seismological inversions. The use of this general damping envelope was found to be justified quantitatively using least-squares fitting and Bayesian inference. Seismology was performed and compared using least squares fitting and Bayesian inference. The Bayesian inference allows more robust estimation of the uncertainties and allows

increasingly complex models to be compared quantitatively. Finally, comparing the transverse loop structure obtained to the results from a forward modelling approach gave good agreement. Several new observational studies have recently been performed, related to the work discussed in this chapter and the previous chapter [e.g. [Pascoe et al., 2016, 2017c](#); [Montes-Solís & Arregui, 2017](#); [Abedini, 2018](#)].

The transverse structure of coronal loops was the focus of Chapter 4. Three models for the transverse density profiles of the loops were quantitatively compared using a forward modelling procedure. This allowed the density profiles to be applied to observations of the transverse intensity profile for 233 coronal loops. The step function density profile represents homogeneous loops with no transition between interior and exterior density, the Gaussian profile represents fully inhomogeneous loops and the linear transition layer model can represent the prior two cases as well as a loop with a homogeneous core and a layer where the density transitions from the external to internal density. The existence of an inhomogeneous region in the transverse density structure is necessary for damping via resonant absorption to occur, and is the basis of the seismology in the previous chapter. It was found that there is clear evidence for inhomogeneous density profiles, with either the Gaussian or transition layer profiles being favoured in over 80% of cases. The linear transition layer profile was found to be the most general, despite the extra parameter meaning it is penalised in the Bayes factor comparisons. The typical value of ϵ , the width of the inhomogeneous layer normalised to the radius, was found to be > 1 , which is higher than is generally assumed in analytical or numerical modelling, and may impact the applicability of such models. However, the simplifications made in the forward modelling should be taken into account when considering these results. The high degree of inhomogeneity across the loops is important for effects such as KHI that depend on strong shear at the boundary of coronal structures, as well as the dissipation of energy in the loop from waves or other sources. Larger inhomogeneous layer widths correspond to less steep density, and therefore velocity, gradients across the magnetic field.

Finally, EUV observations of a spatially resolved Quasi-periodic Fast Propagating (QFP) wave train are combined with radio observations. These radio observations clearly show type III radio bursts associated with the flare and type II bursts associated with the CME expansion. A series of radio sparks (finite-bandwidth-short-duration radio features) were also observed which have the same period as the fast waves seen in the EUV band, and the same frequency drift as the type II emission. Several different scenarios were considered to explain the observations, after further analysis of the entire event. Possible excitation scenarios to produce the periodic radio emission include; steepening of the periodic wave train fronts which shock in the medium related to the expanding CME, or emission due to the

compression of the medium between the CME and the approaching fast wave train. Additionally, the waves may steepen and produce shocks without any interaction with any of the features of the CME, in this context 2D numerical simulations of impulsively generated wave trains in coronal density enhancements were performed. It was found that a series of quasi-periodic steepened fast waves can be produced, which could result in quasi-periodic radio emission in certain conditions. Recently, several new observational studies have been performed [Qu et al., 2017; Shen et al., 2018]. In particular, Kumar et al. [2017] linked fast waves observed in EUV imaging to quasi-periodic features in the radio spectra. More work should be done to explore this relationship between coronal waves and oscillations, and periodic features seen in radio emission. Additionally, further work should be done to combine modelling and observations of QFP wave trains to begin to exploit their seismological and diagnostic potential.

Bibliography

- Abedini, A. 2018, *Sol. Phys.*, 293, 22
- Ahmad, Q. R., Allen, R. C., Andersen, T. C., et al. 2001, *Physical Review Letters*, 87, 071301
- Allison, R. & Dunkley, J. 2014, *MNRAS*, 437, 3918
- Andries, J., Arregui, I., & Goossens, M. 2005, *ApJ*, 624, L57
- Anfinogentov, S., Nakariakov, V. M., & Nisticò, G. 2015a, *A&A*
- Anfinogentov, S. A., Nakariakov, V. M., & Nisticò, G. 2015b, *A&A*, 583, A136
- Antolin, P., De Moortel, I., Van Doorselaere, T., & Yokoyama, T. 2016, *ApJ*, 830, L22
- Antolin, P., Okamoto, T. J., De Pontieu, B., et al. 2015, *ApJ*, 809, 72
- Arber, T., Longbottom, A., Gerrard, C., & Milne, A. 2001, *Journal of Computational Physics*, 171, 151
- Arregui, I. 2018, *Advances in Space Research*, 61, 655
- Arregui, I. & Asensio Ramos, A. 2011, *ApJ*, 740, 44
- Arregui, I. & Asensio Ramos, A. 2014, *A&A*, 565, A78
- Arregui, I., Asensio Ramos, A., & Díaz, A. J. 2013a, *ApJ*, 765, L23
- Arregui, I., Asensio Ramos, A., & Pascoe, D. J. 2013b, *ApJ*, 769, L34
- Arregui, I., Soler, R., & Asensio Ramos, A. 2015, *ApJ*, 811, 104
- Aschwanden, M. J. 2005, *Physics of the Solar Corona* (2nd edition).
- Aschwanden, M. J. & Boerner, P. 2011, *ApJ*, 732, 81
- Aschwanden, M. J., de Pontieu, B., Schrijver, C. J., & Title, A. M. 2002, *Sol. Phys.*, 206, 99

- Aschwanden, M. J., Fletcher, L., Schrijver, C. J., & Alexander, D. 1999, *ApJ*, 520, 880
- Aschwanden, M. J. & Nightingale, R. W. 2005, *ApJ*, 633, 499
- Aschwanden, M. J., Nightingale, R. W., Andries, J., Goossens, M., & Van Doorsse-laere, T. 2003, *ApJ*, 598, 1375
- Aschwanden, M. J., Nightingale, R. W., & Boerner, P. 2007, *ApJ*, 656, 577
- Aschwanden, M. J. & Peter, H. 2017, *ArXiv e-prints* [[arXiv]1701.01177]
- Aschwanden, M. J. & Schrijver, C. J. 2011, *ApJ*, 736, 102
- Aschwanden, M. J., Wülser, J.-P., Nitta, N. V., & Lemen, J. R. 2008, *ApJ*, 679, 827
- Brady, C. S. & Arber, T. D. 2005, *A&A*, 438, 733
- Bray, R. J. & Loughhead, R. E. 1985, *A&A*, 142, 199
- Brooks, D. H., Reep, J. W., & Warren, H. P. 2016, *ApJ*, 826, L18
- Brooks, D. H., Warren, H. P., & Ugarte-Urra, I. 2012, *ApJ*, 755, L33
- Brooks, D. H., Warren, H. P., Ugarte-Urra, I., & Winebarger, A. R. 2013, *ApJ*, 772, L19
- Broomhall, A.-M., Chaplin, W. J., Elsworth, Y., Fletcher, S. T., & New, R. 2009, *ApJ*, 700, L162
- Browning, P. K. & Priest, E. R. 1984, *A&A*, 131, 283
- Chen, P. F. 2011, *Living Reviews in Solar Physics*, 8, 1
- Chen, P. F., Fang, C., & Shibata, K. 2005, *ApJ*, 622, 1202
- Chen, S.-X., Li, B., Xia, L.-D., Chen, Y.-J., & Yu, H. 2014, *Sol. Phys.*, 289, 1663
- Clack, C. T. M. & Ballai, I. 2009, *Physics of Plasmas*, 16, 072115
- Cooper, F. C., Nakariakov, V. M., & Williams, D. R. 2003, *A&A*, 409, 325
- De Moortel, I. 2009, *Space Sci. Rev.*, 149, 65
- De Moortel, I. & Bradshaw, S. J. 2008, *Sol. Phys.*, 252, 101
- De Moortel, I. & Brady, C. S. 2007, *ApJ*, 664, 1210
- De Moortel, I. & Nakariakov, V. M. 2012, *Philosophical Transactions of the Royal Society of London Series A*, 370, 3193

- De Moortel, I. & Pascoe, D. J. 2012, *ApJ*, 746, 31
- Deubner, F.-L. & Gough, D. 1984, *ARA&A*, 22, 593
- Edwin, P. M. & Roberts, B. 1983, *Sol. Phys.*, 88, 179
- Erickson, W. C. 1997, *PASA*, 14, 278
- Fletcher, L., Dennis, B. R., Hudson, H. S., et al. 2011, *Space Sci. Rev.*, 159, 19
- Gallagher, P. T. & Long, D. M. 2011, *Space Sci. Rev.*, 158, 365
- Gizon, L., Birch, A. C., & Spruit, H. C. 2010, *ARA&A*, 48, 289
- Goossens, M., Andries, J., & Aschwanden, M. J. 2002, *A&A*, 394, L39
- Goossens, M., Arregui, I., Ballester, J. L., & Wang, T. J. 2008, *A&A*, 484, 851
- Gopalswamy, N., Yashiro, S., Kaiser, M. L., Howard, R. A., & Bougeret, J.-L. 2001, *ApJ*, 548, L91
- Grigis, P., Yingna, S., & Weber, M. 2013, Tech. Rep., AIA team
- Guo, Y., Erdélyi, R., Srivastava, A. K., et al. 2015, *ApJ*, 799, 151
- Handy, B. N., Acton, L. W., Kankelborg, C. C., et al. 1999, *Sol. Phys.*, 187, 229
- Hannah, I. G. & Kontar, E. P. 2012, *A&A*, 539, A146
- Heyvaerts, J. & Priest, E. R. 1983, *A&A*, 117, 220
- Hood, A. W., Ruderman, M., Pascoe, D. J., et al. 2013, *A&A*, 551, A39
- Jelínek, P. & Karlický, M. 2012, *A&A*, 537, A46
- Jelínek, P., Karlický, M., & Murawski, K. 2012, *A&A*, 546, A49
- Karlický, M., Mészárosóvá, H., & Jelínek, P. 2013, *A&A*, 550, A1
- Kass, R. E. & Raftery, A. E. 1995, *Journal of the American Statistical Association*, 90, 773
- Katsiyannis, A. C., Williams, D. R., McAteer, R. T. J., et al. 2003, *A&A*, 406, 709
- Kennewell, J. & Steward, G. 2003, Solar Radio Spectrograph [SRS] Data Viewer [Srsdisplay] (Sydney: IPS Radio and Space Serv.)
- Klimchuk, J. A. 2015, *Philosophical Transactions of the Royal Society of London Series A*, 373, 20140256

- Kumar, P., Nakariakov, V. M., & Cho, K.-S. 2017, *ApJ*, 844, 149
- Lemen, J. R., Title, A. M., Akin, D. J., et al. 2012, *Sol. Phys.*, 275, 17
- Liu, W., Nitta, N. V., Schrijver, C. J., Title, A. M., & Tarbell, T. D. 2010, *ApJ*, 723, L53
- Liu, W. & Ofman, L. 2014, *Sol. Phys.*, 289, 3233
- Liu, W., Ofman, L., Nitta, N. V., et al. 2012, *ApJ*, 753, 52
- Liu, W., Title, A. M., Zhao, J., et al. 2011, *ApJ*, 736, L13
- Lodders, K. 2003, *ApJ*, 591, 1220
- Magdaleníć, J., Vršnak, B., Zlobec, P., Messerotti, M., & Temmer, M. 2005, in *Astrophysics and Space Science Library*, Vol. 320, *Solar Magnetic Phenomena*, ed. A. Hanslmeier, A. Veronig, & M. Messerotti, 259–262
- Magyar, N. & Van Doorselaere, T. 2016a, *A&A*, 595, A81
- Magyar, N. & Van Doorselaere, T. 2016b, *ApJ*, 823, 82
- Mann, G., Classen, T., & Aurass, H. 1995a, *A&A*, 295, 775
- Mann, I. R. & Wright, A. N. 1995, *J. Geophys. Res.*, 100, 23677
- Mann, I. R., Wright, A. N., & Cally, P. S. 1995b, *J. Geophys. Res.*, 100, 19441
- Markwardt, C. B. 2009, in *Astronomical Society of the Pacific Conference Series*, Vol. 411, *Astronomical Data Analysis Software and Systems XVIII*, ed. D. A. Bohlender, D. Durand, & P. Dowler, 251
- Martínez Oliveros, J. C., Raftery, C. L., Bain, H. M., et al. 2012, *ApJ*, 748, 66
- McEwan, M. P., Díaz, A. J., & Roberts, B. 2008, *A&A*, 481, 819
- McEwan, M. P., Donnelly, G. R., Díaz, A. J., & Roberts, B. 2006, *A&A*, 460, 893
- McLean, D. J. 1967, *Proceedings of the Astronomical Society of Australia*, 1, 47
- Mészárosová, H., Karlický, M., Jelínek, P., & Rybák, J. 2014, *ApJ*, 788, 44
- Mészárosová, H., Karlický, M., & Rybák, J. 2011, *Sol. Phys.*, 273, 393
- Mészárosová, H., Karlický, M., Rybák, J., & Jiříčka, K. 2009a, *A&A*, 502, L13
- Mészárosová, H., Karlický, M., Rybák, J., & Jiříčka, K. 2009b, *ApJ*, 697, L108
- Mészárosová, H., Rybák, J., Kashapova, L., et al. 2016, *A&A*, 593, A80

- Metropolis, N., Rosenbluth, A. W., Rosenbluth, M. N., Teller, A. H., & Teller, E. 1953, *J. Chem. Phys.*, 21, 1087
- Montes-Solís, M. & Arregui, I. 2017, *ApJ*, 846, 89
- Moreton, G. E. 1960, *AJ*, 65, 494
- Morton, R. J. & Erdélyi, R. 2009a, *A&A*, 502, 315
- Morton, R. J. & Erdélyi, R. 2009b, *ApJ*, 707, 750
- Morton, R. J. & Moorooogen, K. 2016, *A&A*, 593, A59
- Mrozek, T. 2011, *Sol. Phys.*, 270, 191
- Murawski, K. & Roberts, B. 1994, *Sol. Phys.*, 151, 305
- Nakariakov, V. M., Arber, T. D., Ault, C. E., et al. 2004, *MNRAS*, 349, 705
- Nakariakov, V. M. & Ofman, L. 2001, *A&A*, 372, L53
- Nakariakov, V. M., Ofman, L., Deluca, E. E., Roberts, B., & Davila, J. M. 1999, *Science*, 285, 862
- Nakariakov, V. M., Pascoe, D. J., & Arber, T. D. 2005, *Space Sci. Rev.*, 121, 115
- Nakariakov, V. M. & Verwichte, E. 2005, *Living Reviews in Solar Physics*, 2, 3
- Newkirk, Jr., G. 1961, *ApJ*, 133, 983
- Nisticò, G., Anfinogentov, S., & Nakariakov, V. M. 2014a, *A&A*, 570, A84
- Nisticò, G., Bothmer, V., Patsourakos, S., & Zimbardo, G. 2009, *Sol. Phys.*, 259, 87
- Nisticò, G., Nakariakov, V. M., & Verwichte, E. 2013, *A&A*, 552, A57
- Nisticò, G., Pascoe, D. J., & Nakariakov, V. M. 2014b, *A&A*, 569, A12
- Nisticò, G., Polito, V., Nakariakov, V. M., & Del Zanna, G. 2017, *A&A*, 600, A37
- Ofman, L. 2010, *Living Reviews in Solar Physics*, 7, 4
- Ofman, L. & Aschwanden, M. J. 2002, *ApJ*, 576, L153
- Ofman, L. & Davila, J. M. 1995, *J. Geophys. Res.*, 100, 23427
- Ofman, L., Davila, J. M., & Steinolfson, R. S. 1994a, *ApJ*, 421, 360
- Ofman, L., Davila, J. M., & Steinolfson, R. S. 1994b, *Geophys. Res. Lett.*, 21, 2259
- Oliver, R., Ruderman, M. S., & Terradas, J. 2014, *ApJ*, 789, 48

- Oliver, R., Ruderman, M. S., & Terradas, J. 2015, *ApJ*, 806, 56
- Owen, N. R., De Moortel, I., & Hood, A. W. 2009, *A&A*, 494, 339
- Pagano, P. & De Moortel, I. 2017, *A&A*, 601, A107
- Pascoe, D. J., Anfinogentov, S., Nisticò, G., Goddard, C. R., & Nakariakov, V. M. 2017a, *A&A*, 600, A78
- Pascoe, D. J., Goddard, C. R., Anfinogentov, S., & Nakariakov, V. M. 2017b, *A&A*, 600, L7
- Pascoe, D. J., Goddard, C. R., & Nakariakov, V. M. 2016, *A&A*, 593, A53
- Pascoe, D. J., Hood, A. W., de Moortel, I., & Wright, A. N. 2012, *A&A*, 539, A37
- Pascoe, D. J., Hood, A. W., De Moortel, I., & Wright, A. N. 2013a, *A&A*, 551, A40
- Pascoe, D. J., Nakariakov, V. M., & Kupriyanova, E. G. 2013b, *A&A*, 560, A97
- Pascoe, D. J., Nakariakov, V. M., & Kupriyanova, E. G. 2014, *A&A*, 568, A20
- Pascoe, D. J., Russell, A. J. B., Anfinogentov, S. A., et al. 2017c, *A&A*, 607, A8
- Pascoe, D. J., Wright, A. N., & De Moortel, I. 2010, *ApJ*, 711, 990
- Patsourakos, S., Vourlidas, A., Wang, Y. M., Stenborg, G., & Thernisien, A. 2009, *Sol. Phys.*, 259, 49
- Pesnell, W. D., Thompson, B. J., & Chamberlin, P. C. 2012, *Sol. Phys.*, 275, 3
- Peter, H., Bingert, S., Klimchuk, J. A., et al. 2013, *A&A*, 556, A104
- Pick, M. & Vilmer, N. 2008, *A&A Rev.*, 16, 1
- Qu, Z. N., Jiang, L. Q., & Chen, S. L. 2017, *ApJ*, 851, 41
- Reale, F. 2010, *Living Reviews in Solar Physics*, 7, 5
- Reale, F., Guarrasi, M., Testa, P., et al. 2011, *ApJ*, 736, L16
- Robbrecht, E., Berghmans, D., & Van der Linden, R. A. M. 2009, *ApJ*, 691, 1222
- Roberts, B. 1981a, *Sol. Phys.*, 69, 39
- Roberts, B. 1981b, *Sol. Phys.*, 69, 27
- Roberts, B. 2008, in *IAU Symposium*, Vol. 247, *Waves Oscillations in the Solar Atmosphere: Heating and Magneto-Seismology*, ed. R. Erdélyi & C. A. Mendoza-Briceno, 3–19

- Roberts, B., Edwin, P. M., & Benz, A. O. 1983, *Nature*, 305, 688
- Roberts, B., Edwin, P. M., & Benz, A. O. 1984, *ApJ*, 279, 857
- Ruderman, M. S. & Roberts, B. 2002, *ApJ*, 577, 475
- Russell, A. J. B., Simões, P. J. A., & Fletcher, L. 2015, *A&A*, 581, A8
- Sakurai, T., Goossens, M., & Hollweg, J. V. 1991, *Sol. Phys.*, 133, 227
- Sarkar, S., Pant, V., Srivastava, A. K., & Banerjee, D. 2016, *Sol. Phys.*, 291, 3269
- Scargle, J. D. 1982, *ApJ*, 263, 835
- Schmelz, J. T., Kimble, J. A., Jenkins, B. S., et al. 2010, *ApJ*, 725, L34
- Schmidt, J. M. & Cairns, I. H. 2012, *Journal of Geophysical Research (Space Physics)*, 117, A04106
- Schrijver, C. J., Aschwanden, M. J., & Title, A. M. 2002, *Sol. Phys.*, 206, 69
- Shen, Y. & Liu, Y. 2012, *ApJ*, 753, 53
- Shen, Y., Liu, Y., Song, T., & Tian, Z. 2018, *ApJ*, 853, 1
- Shestov, S., Nakariakov, V. M., & Kuzin, S. 2015, *ApJ*, 814, 135
- Shibata, K. & Magara, T. 2011, *Living Reviews in Solar Physics*, 8, 6
- Smerd, S. F., Sheridan, K. V., & Stewart, R. T. 1974, in *IAU Symposium*, Vol. 57, *Coronal Disturbances*, ed. G. A. Newkirk, 389
- Soler, R. & Terradas, J. 2015, *ApJ*, 803, 43
- Soler, R., Terradas, J., Oliver, R., Ballester, J. L., & Goossens, M. 2010, *ApJ*, 712, 875
- Srivastava, A. K., Dwivedi, B. N., & Kumar, M. 2013, *Ap&SS*, 345, 25
- Sych, R., Nakariakov, V. M., Karlicky, M., & Anfinogentov, S. 2009, *A&A*, 505, 791
- Taroyan, Y. & Bradshaw, S. J. 2014, *Sol. Phys.*, 289, 1959
- Terradas, J., Andries, J., & Goossens, M. 2007, *A&A*, 469, 1135
- Terradas, J., Andries, J., Goossens, M., et al. 2008, *ApJ*, 687, L115
- Terradas, J. & Ofman, L. 2004, *ApJ*, 610, 523
- Thurgood, J. O., Morton, R. J., & McLaughlin, J. A. 2014, *ApJ*, 790, L2

- Tomczyk, S., Card, G. L., Darnell, T., et al. 2008, *Sol. Phys.*, 247, 411
- Tomczyk, S., McIntosh, S. W., Keil, S. L., et al. 2007, *Science*, 317, 1192
- Torrence, C. & Compo, G. P. 1998, *Bulletin of the American Meteorological Society*, 79, 61
- Uchida, Y. 1970, *PASJ*, 22, 341
- Van Doorselaere, T., Andries, J., Poedts, S., & Goossens, M. 2004, *ApJ*, 606, 1223
- Van Doorselaere, T., Nakariakov, V. M., & Verwichte, E. 2007, *A&A*, 473, 959
- Vand, V. 1943, *Nature*, 151, 728
- Vasheghani Farahani, S., Nakariakov, V. M., Verwichte, E., & Van Doorselaere, T. 2012, *A&A*, 544, A127
- Vasheghani Farahani, S., Van Doorselaere, T., Verwichte, E., & Nakariakov, V. M. 2009, *A&A*, 498, L29
- Verth, G., Terradas, J., & Goossens, M. 2010, *ApJ*, 718, L102
- Verwichte, E., Aschwanden, M. J., Van Doorselaere, T., Foullon, C., & Nakariakov, V. M. 2009, *ApJ*, 698, 397
- Verwichte, E., Foullon, C., & Van Doorselaere, T. 2010, *ApJ*, 717, 458
- Verwichte, E., Nakariakov, V. M., & Cooper, F. C. 2005, *A&A*, 430, L65
- Verwichte, E., Nakariakov, V. M., Ofman, L., & Deluca, E. E. 2004, *Sol. Phys.*, 223, 77
- Verwichte, E., Van Doorselaere, T., Foullon, C., & White, R. S. 2013a, *ApJ*, 767, 16
- Verwichte, E., Van Doorselaere, T., White, R. S., & Antolin, P. 2013b, *A&A*, 552, A138
- von Toussaint, U. 2011, *Reviews of Modern Physics*, 83, 943
- Wang, T. 2011, *Space Sci. Rev.*, 158, 397
- Wang, T. J. & Solanki, S. K. 2004, *A&A*, 421, L33
- Warmuth, A. 2015, *Living Reviews in Solar Physics*, 12
- Warren, H. P., Ugarte-Urra, I., Doschek, G. A., Brooks, D. H., & Williams, D. R. 2008, *ApJ*, 686, L131

- Webb, D. F. & Howard, T. A. 2012, *Living Reviews in Solar Physics*, 9, 3
- White, R. S. & Verwichte, E. 2012, *A&A*, 537, A49
- White, R. S., Verwichte, E., & Foullon, C. 2013, *ApJ*, 774, 104
- Wiegmann, T., Petrie, G. J. D., & Riley, P. 2017, *Space Sci. Rev.*, 210, 249
- Wiegmann, T. & Sakurai, T. 2012, *Living Reviews in Solar Physics*, 9, 5
- Wu, C. S., Wang, C. B., Zhou, G. C., Wang, S., & Yoon, P. H. 2005, *ApJ*, 621, 1129
- Yang, L., Zhang, L., He, J., et al. 2015, *ApJ*, 800, 111
- Yu, H., Li, B., Chen, S.-X., & Guo, M.-Z. 2015, *ApJ*, 814, 60
- Yu, H., Li, B., Chen, S.-X., Xiong, M., & Guo, M.-Z. 2016, *ApJ*, 833, 51
- Yu, S., Nakariakov, V. M., Selzer, L. A., Tan, B., & Yan, Y. 2013, *ApJ*, 777, 159
- Yuan, D., Shen, Y., Liu, Y., et al. 2013, *A&A*, 554, A144
- Yuan, D. & Van Doorselaere, T. 2016, *ApJS*, 223, 24
- Zaitsev, V. V. 1966, *Soviet Ast.*, 9, 572
- Zaitsev, V. V. & Stepanov, A. V. 1982, *Soviet Astronomy Letters*, 8, 132
- Zajtsev, V. V. & Stepanov, A. V. 1975, *Issledovaniia Geomagnetizmu Aeronomii i Fizike Solntsa*, 37, 3
- Zimovets, I., Vilmer, N., Chian, A. C.-L., Sharykin, I., & Struminsky, A. 2012, *A&A*, 547, A6
- Zimovets, I. V. & Nakariakov, V. M. 2015, *A&A*, 577, A4
- Zimovets, I. V. & Sadykov, V. M. 2015, *Advances in Space Research*, 56, 2811